

Anisotropic Fracture Toughness Characterization of Shale Formation  
from Drill Cuttings

by  
Erica Esatyana

A dissertation submitted to the Department of Petroleum Engineering,  
Cullen College of Engineering  
in partial fulfillment of the requirements for the degree of

DOCTOR OF PHILOSOPHY

in Petroleum Engineering

Chair of Committee: Dr. Ahmad Sakhaee-Pour

Committee Member: Prof. S M Farouq Ali

Committee Member: Prof. Christine Ehlig-Economides

Committee Member: Prof. George K Wong

Committee Member: Prof. Kamy Sepehrnoori

University of Houston  
May 2022

Copyright 2022, Erica Esatyana

## **ACKNOWLEDGMENTS**

I would like to express my gratitude to Dr. Ahmad Sakhaee-Pour for his tremendous assistance, guidance, innovative ideas, and patience throughout my Ph.D. program to achieve high-quality research. Thank you to all the committee members – Prof. S M Farouq Ali, Prof. Christine Ehlig-Economides, Prof. George K Wong, and Prof. Kamy Sepehrnoori for their feedback on improving my dissertation. I am grateful to the Qatar National Research Fund (a member of the Qatar Foundation) through Grant #NPRP11S-0109-180241 and collaboration with the MetaRock Laboratories to validate my research work.

## **DEDICATION**

I dedicate this dissertation to my parents, family, and friends, who have been a great source of support and motivation.



## ABSTRACT

Shale is a sedimentary rock composed of clay minerals and silt-sized particles. Its pore throat sizes are as small as 10 nm in its matrix, which leads to ultralow permeability. It has become economically viable for hydrocarbon recovery because of hydraulic fracturing, in which the required energy is defined by fracture toughness. Shale is mechanically unstable and retrieving a suitable core size for common tests is costly and time-consuming. Thus, there is a need to develop new methods applicable to small pieces such as drill cuttings, which are often the only sources available in real-time conditions.

This study proposes two methods for the geomechanical characterization of shale at the core scale based on the interpretation of small-scale measurements. Both rely on nanoindentations. The proposed conceptual models have applications in characterizing formation heterogeneity in the petroleum industry. The first determines Young's moduli from cuttings, and the results are compared with those of the core plugs from the Wolfcamp Formation. The sensitivity of the results to sample preparation is also discussed.

The second method characterizes the fracture toughness of shale based on the conceptual model proposed in accordance with the effective medium theory. The proposed model sheds light on the complexities of the induced fracture patterns in shale that differ from those observed in homogeneous materials, such as fused silica and aluminum. The conceptual model is realistic for shale because it captures the sample heterogeneity. The second method is tested at a small scale using different tip

geometries. The interpreted fracture toughness values from the cube-corner and Berkovich tips are close, with less than 18% difference, which provides a partial validation for the conceptual model.

The proposed model is also tested against independent data obtained from the cracked Chevron notched Brazilian disc (CCNBD) test. The difference between predicted fracture toughness values from nanoindentation and the CCNBD test is less than 13%, and this good agreement validates the proposed model. The proposed model has applications in characterizing the mechanical properties of shale using small samples from unconventional resources.

## TABLE OF CONTENTS

<b>ACKNOWLEDGMENTS.....</b>	<b>III</b>
<b>DEDICATION .....</b>	<b>III</b>
<b>ABSTRACT .....</b>	<b>IV</b>
<b>TABLE OF CONTENTS .....</b>	<b>VI</b>
<b>LIST OF TABLES.....</b>	<b>X</b>
<b>LIST OF FIGURES.....</b>	<b>XI</b>
<b>NOMENCLATURE .....</b>	<b>XVI</b>
<b>CHAPTER 1 . INTRODUCTION .....</b>	<b>1</b>
1.1.    General problem .....	1
1.2.    Objectives .....	4
1.3.    Hypotheses.....	4
1.4.    Contribution to knowledge .....	5
1.5.    Summary of chapters .....	6
<b>CHAPTER 2 . LITERATURE REVIEW .....</b>	<b>8</b>
2.1.    Importance of shale.....	8
2.2.    Why is fracture toughness important? .....	9
2.2.1.    Fundamental concepts of fracture toughness .....	9
2.2.2.    Modes and types of fracture .....	10
2.2.3.    Cracked Chevron notched Brazilian discs (CCNBD) .....	13

2.2.4.	Heterogeneity and anisotropy in shale .....	14
2.2.5.	Fracture toughness in shale .....	16
2.3.	Fundamental concepts of nanoindentation .....	17
2.3.1.	Indenter tip geometries .....	20
2.3.2.	Load-displacement curve .....	23
2.3.3.	Indentation modulus and hardness .....	25
2.3.4.	Atomic force microscopy (AFM) versus nanoindentation .....	27
2.3.5.	Various sources of errors affecting nanoindentation data .....	28
2.4.	Fracture toughness measurements using nanoindentation .....	30
2.4.1.	Fracture-length method .....	31
2.4.2.	Energy method .....	34
2.4.3.	A comment on the application of the energy method for fracture toughness characterization based on nanoindentation .....	37

### **CHAPTER 3 . INDENTATION TECHNIQUE TO DETERMINE YOUNG’S MODULUS OF SHALE AT THE CORE SCALE USING DRILL CUTTINGS.....40**

3.1.	Sample descriptions .....	40
3.2.	Sample preparation .....	40
3.3.	Sensitivity of Young’s moduli to sample preparation .....	43
3.4.	Determining the cutting scale for nanoindentation .....	44
3.5.	Discussion .....	55
3.6.	Conclusions .....	57

### **CHAPTER 4 . CHARACTERIZING ANISOTROPIC FRACTURE TOUGHNESS OF SHALE USING NANOINDENTATION.....59**

4.1.	Sample descriptions .....	59
4.2.	Complexities of fracture toughness characterization in shale .....	59
4.3.	Approach.....	61
4.3.1.	Conceptual model.....	61
4.3.2.	Maximum applied load in nanoindentation.....	63
4.3.3.	Damaged versus fractured regions .....	64
4.4.	Results.....	69
4.5.	Discussion.....	77
4.6.	Conclusions.....	82

## **CHAPTER 5 . EVALUATION OF ANISOTROPIC SHALE FRACTURE TOUGHNESS USING NANOINDENTATION AND CRACKED CHEVRON NOTCHED BRAZILIAN DISC (CCNBD) TESTS.....84**

5.1.	Sample descriptions .....	84
5.2.	Experimental procedure.....	85
5.2.1.	CCNBD test.....	85
5.2.2.	Nanoindentation on core plugs.....	88
5.2.3.	Nanoindentation on cuttings.....	90
5.3.	Results.....	93
5.3.1.	Nanoindentation on core plugs.....	93
5.3.2.	Nanoindentation on cuttings.....	99
5.4.	Validation.....	100
5.5.	Discussion.....	104

5.6.	Conclusions.....	107
<b>CHAPTER 6 . ASSUMPTIONS AND LIMITATIONS .....</b>		<b>109</b>
6.1.	Indentation technique to determine Young’s modulus of shale at the core scale using drill cuttings.....	109
6.2.	Proposed conceptual model .....	111
<b>CHAPTER 7 . CONCLUDING REMARKS AND FUTURE WORKS RECOMMENDATIONS .....</b>		<b>114</b>
7.1.	Concluding remarks.....	114
7.1.1.	Indentation technique to determine Young’s modulus of shale at the core scale using drill cuttings.....	114
7.1.2.	Proposed conceptual model.....	115
7.2.	Future work recommendations .....	116
7.2.1.	Indentation technique to determine Young’s modulus of shale at the core scale using drill cuttings.....	116
7.2.2.	Proposed conceptual model.....	116
<b>REFERENCES .....</b>		<b>119</b>
<b>APPENDICES.....</b>		<b>135</b>
1.	Histogram of Samples B, C, and D (in lieu of Chapter 5).....	135
2.	Title pages of the journal publications relevant to the dissertation .....	138

## LIST OF TABLES

Table 2.1—The experimental methods to evaluate rock fracture toughness in different modes. ....	12
Table 2.2—Summary of the indenter tip properties and their impressions on the shale surface. The cube-corner tip has a smaller applied load than the other tips because it has a sharp contact angle. ....	22
Table 2.3—Typical interpreted Young’s moduli calculated from the shale samples and indenter tips. ....	27
Table 3.1—Shale surface with various discs for sample preparation at different stages. A nanoindenter tip is placed on the sample surface in the first stage for size comparison. The surface roughness decreases at higher stages and is more reflective of light. ....	42
Table 4.1— The relevant parameters to calculate fracture toughness (last row) of shale samples using a Berkovich tip in a parallel sample (Figure 4.7a) and a cube-corner tip in a perpendicular sample (Figure 4.7b). ....	70
Table 5.1—The pertinent properties of the studied shale. ....	84
Table 5.1 (continued) .....	85
Table 5.2—Typical CCNBD test results on four shale samples during pre-notch, post-notch, and post-test (fracture test).....	86
Table 5.3—The semicircular shale surface before and after sample preparation. The surface of a sample is more reflective of light upon completion. ....	89
Table 5.4—Prepared samples glued to an aluminum puck for indentation.....	92
Table 5.5—The relevant parameters for fracture toughness characterization of shale samples using nanoindentation. The high-resolution images are shown in Figure 5.4.....	95
Table 5.6—The average anisotropic fracture toughness of the shale samples.....	102

## LIST OF FIGURES

Figure 2.1—Modes of fracture are classified into (Irwin, 1968): (a) mode I or pure tensile, (b) mode II or in-plane shear, and (c) mode III or out-of-plane stress. ....	11
Figure 2.2—The loading fixture for pure mode I (Fowell, 1995). ....	14
Figure 2.3—Contact of a rigid indenter with a flat material. ....	18
Figure 2.4—Type of stress-strain behavior (Fischer-Cripps, 2011) in materials, such as ideal elastic-plastic (a) and rigid-plastic (b). ....	19
Figure 2.5—A schematic of an indentation movement with various parameters involved in the analysis (Oliver and Pharr, 1992). ....	23
Figure 2.6—The nanoindenter features that perform indentation testing. ....	24
Figure 2.7—A typical load-displacement curve obtained from nanoindentation (ISO 14577). The slope on the unloading part is used to characterize the mechanical properties. ....	25
Figure 2.8—Schematic of potential fracture patterns (Fischer-Cripps, 2011) where analytical relations were developed, such as Palmqvist or radial (a), lateral (b), median (c), and half-penny fractures (d). ....	31
Figure 2.9—Schematic of a sample indented with a three-sided pyramid geometry tip, where the gray region represents the impression. ....	33
Figure 3.1—The shale cross-section is divided into equal areas and indented at the center (a). The average Young's modulus variation is obtained from the nanoindentation of the shale sample at each preparation stage (b). ....	44
Figure 3.2—Schematic of the plastic zone. The minimum distance between indentations is larger than the plastic zone size (Chen and Bull, 2007) to avoid interference (spacing > $2cp$ ). ....	45
Figure 3.3—Conceptual illustration of the representative element volume (REV), in which repetition (a) generates the shale bulk volume (b). ....	46
Figure 3.4—Variation of the plastic zone size with Young's modulus at different yield strength values. The Poisson's ratio equals	



0.25, and Young's modulus and the yield strength values represent shale formations (Sayers, 2013; Sone and Zoback, 2013; Rybacki et al., 2015).....	47
Figure 3.5—Spatial locations of nanoindentations in four steps on a core plug ( $d = 25.4$ mm, $l = 17.6$ mm) with regular spacing. The area is equally divided in each step, and the process stops when the distance between the nearest indentations is close to the plastic zone size (a, b, c, d).....	49
Figure 3.6—The variation of Young's modulus with the indentation number for samples D (a), E (b), F (c), and G (d). The spatial locations of the indentations are shown in Figure 3.5. ....	50
Figure 3.7—Young's moduli of shale samples resulting from nanoindentations with regular spacings (a) and the difference between Young's modulus at each step and the four nearest at the subsequent steps (b). ....	51
Figure 3.8—Small pieces or cuttings of shale used to test the accuracy of the cutting scale (a), and prepared samples are glued to an aluminum puck for nanoindentation (b). ....	52
Figure 3.9—Young's moduli of shale samples obtained from independent triaxial tests using core plugs and nanoindentation using small pieces or cuttings (a) and the decrease in error when samples reached a higher level of smoothness after preparation (b). ....	53
Figure 3.10—The polished surface of the core plug, which corresponds to stage 7 in Table 3.1, reaches a higher level of smoothness (a) than cuttings in Figure 3.10b (b). Cuttings with the smoothest surface are less influenced by local flaws and close to the core scale measurements.....	54
Figure 4.1—High-resolution images of shale indented by 300, 500, and 700 mN. The induced fractures are distinct even at the same load, indicating a high heterogeneity level. The red arrows point out the relatively simple patterns used for fracture toughness characterization in this study.....	61
Figure 4.2—Schematic of the proposed conceptual model based on the Voronoi cells in shale. Various colors represent the stronger domain while the boundaries between them constitute the weaker domain (a). The loads applied to the indenter tip induce fractures when the tip hits the weaker domain (b).....	62

Figure 4.3—The hybrid grid system used in this study. The core plug diameter, $d$ , is 25.4 mm. The major grid size, $m$ , and minor, $s$ , are 17.1 and 2.44 mm, respectively. ....	64
Figure 4.4—High-resolution images of shale surface resulting from the Berkovich tip. The red circles represent two relatively simple fracture patterns, and the purple circle indicates a complex pattern. ....	65
Figure 4.5—Histogram of a shale sample for simple and complex fracture patterns parallel to the bedding planes with various loads (a). High-resolution images where the applied load is acceptable for fracture toughness characterization when smaller than or equal to 550 mN (b) and excessive when larger than 550 mN (c).....	67
Figure 4.6—Histogram of a shale sample for simple and complex fracture patterns perpendicular to the bedding planes with various loads (a). High-resolution images where all the applied loads are acceptable for fracture toughness characterization (b) because the induced fractures are relatively simple. ....	68
Figure 4.7— The indentation impression on a shale surface of a Berkovich tip parallel to the bedding plane (a) and a cube-corner tip perpendicular to the bedding plane (b).....	70
Figure 4.8—The variation of the ratios of the indentation tests with simple and complex fractures to the total number of tests, which is equal to 49, at each load. Complex induced fractures occur when the applied load is greater than 550 mN for Sample 1 and 700 mN for Sample 2. However, some loads do not create any fractures. ....	71
Figure 4.9—The fracture toughness values of four shale samples tested by the Berkovich tip. ....	73
Figure 4.10—The fracture toughness values of four shale samples tested by the cube-corner tip. ....	75
Figure 4.11—The average fracture toughness values of four shale samples using the Berkovich and cube-corner tips. ....	77
Figure 4.12—Three classifications of fracture propagation at the core scale (Zhang, 2013) are divider (a), short transverse (b), and arrester (c). ....	78
Figure 4.13—Conceptual illustrations of the anisotropic shale samples: parallel (a) and perpendicular (b) to the bedding planes.	

Fractures were induced at a small scale using nanoindentation. The triangles are the impression or indented area; the red and green marks represent simple fracture patterns produced through the grain boundaries and between the layers, respectively. ....	80
Figure 5.1—Cracked Chevron Notched Brazilian Disc (CCNBD) test of the shale samples. The three stages are pre-notch, post-notch, and post-test. ....	87
Figure 5.2—Notch and fracture propagation orientations when perpendicular (a) and parallel (b) to the bedding planes (blue lines). The perpendicular and parallel samples match Divider and Arrester orientations, respectively. ....	88
Figure 5.3—Hybrid grid system of a semicircular shale sample. The diameter ( $d$ ) of the core sample varies (Table 5.1). The major grid ( $m \times n$ ) pattern is $9 \times 9$ , which is equal in size to $0.566 \times 0.708$ in. The minor grid ( $s1 \times s2$ ) pattern is $5 \times 4$ , which is equal in size to $0.062 \times 0.078$ in. ....	90
Figure 5.4— Rock crusher (a) and shale cuttings (b) obtained from the semicircular samples shown in Table 5.3. ....	91
Figure 5.5—Impressions of the Berkovich tip on the surface of shale parallel (Samples A and B) and perpendicular (Samples C and D) to the bedding planes, where the applied load is 500 mN. ....	94
Figure 5.6— Histogram of Sample A (parallel to the bedding) in three regions with various loads (a). High-resolution images where the applied load is acceptable when (b) smaller than or equal to 750 mN and (c) excessive when larger than 750 mN. ....	97
Figure 5.7— Fracture toughness values of four shale samples are listed in Table 5.3. The data shows 144 out of 1,620 tests that led to simple fracture patterns for Sample A; 198 out of 1,620 tests for Sample B; 194 out of 1,620 tests for Sample C; and 184 out of 1,620 tests for Sample D. ....	98
Figure 5.8—Histogram of the number of indents where the maximum applied load is 500 mN (a). The fracture toughness of shale cuttings shows that 14 out of 47 tests led to simple fractures for Sample A; 20 out of 77 tests for Sample B; 12 out of 53 tests for Sample C; and 18 out of 54 tests for Sample D (b). ....	100

Figure 5.9—The average fracture toughness of the shale samples based on nanoindentation and the CCNBD test. ....	102
Figure 5.10—The error associated with the predicted shale anisotropic fracture toughness using nanoindentation (core plugs and cuttings) with the CCNBD results for validation purposes. ....	103
Figure 5.11—Conceptual illustrations of shale samples that are perpendicular (Fig. 3a) and parallel (Fig. 3b) to the bedding planes (blue lines) and the induced fractures on the surface of shale using nanoindentation (Esatyana et al., 2021). ....	105
Figure A.1—Histogram of sample B (parallel to the bedding) in three regions with various loads. High-resolution images where the applied load is <b>b</b> acceptable when it is smaller than or equal to 700 mN and <b>c</b> excessive when it is larger than 700 mN to characterize shale fracture toughness. ....	135
Figure A.2—Histogram of sample C (perpendicular to the bedding) in three regions with various loads. High-resolution images where the applied load is <b>b</b> acceptable when it is smaller than or equal to 650 mN and <b>c</b> excessive when it is larger than 650 mN to characterize shale fracture toughness. ....	136
Figure A.3—Histogram of sample D (perpendicular to the bedding) in three regions with various loads. High-resolution images where the applied load is <b>b</b> acceptable when it is smaller than or equal to 750 mN and <b>c</b> excessive when it is larger than 750 mN to characterize shale fracture toughness. ....	137

## NOMENCLATURE

$\alpha$	= empirical coefficient, dimensionless
$\beta$	= shape factor or geometric parameter, dimensionless
$\varepsilon$	= intercept factor, dimensionless
$\theta$	= face angle with the central axis of the indenter or semi-angle, deg
$\sigma$	= applied stress, N
$\sigma_{\max}$	= maximum applied stress, N
$\sigma_{\text{yield}}$	= yield strength, $\frac{\text{N}}{\text{m}^2}$
$A_c$	= projected area, $\text{microns}^2$
$a$	= distance from the center to the corner, microns
$a_1$	= fracture length of pure mode I, m
$a_r$	= contact radius, microns
$B$	= sample thickness, m
CCNBD	= cracked Chevron notched Brazilian disc
$c$	= fracture length, microns
$c_p$	= plastic zone radius, microns
$D$	= sample diameter, m
$d$	= total deformation, microns
$E_i$	= Young's modulus of the indenter tip, GPa
$E_r$	= reduced modulus, GPa
$E_s$	= Young's modulus of the sample, GPa

$F_{max}$	= applied compressive load, N
$H$	= hardness of the sample, GPa
$h_c$	= contact depth or penetration depth of the elastic contact, microns
$h_f$	= final depth where the elastic displacements are recovered upon unloading, microns
$h_{max}$	= maximum indentation depth, microns
$h_s$	= surface displacement at the contact perimeter, microns
$K_c$	= fracture toughness using nanoindentation, $\text{MPa}\cdot\text{m}^{1/2}$
$K_{IC}$	= fracture toughness of pure mode I, $\text{MPa}\cdot\text{m}^{1/2}$
$l$	= distance from the indented corner to the fracture tip, microns
$P_{max}$	= maximum applied load, mN
$R$	= sphere radius, microns
$S$	= slope which is equal to $\frac{dP}{dh}$ obtained from the unloading portion, dimensionless
$\nu_i$	= indenter tip Poisson's ratio, dimensionless
$\nu_s$	= sample Poisson's ratio, dimensionless
$Y$	= geometry factor, dimensionless
$Y_{min}^*$	= critical stress intensity factor, dimensionless

# CHAPTER 1 . INTRODUCTION

## 1.1. General problem

Shale formations have been extracted over the past decades as a major natural gas and oil source in the United States (EIA, 2021). Shale is a fine-grained clastic sedimentary rock consisting of clay, quartz, calcite, pyrite, and kerogen (Li and Sakhaee Pour, 2016; Hornby et al., 1994) with extremely low permeabilities (Soliman et al., 1991; Javadpour, 2009). It is mechanically unstable because of various mineralogical components that easily break into pieces. A scanning electron microscope (SEM) has been used to study numerous samples, and the findings are that the pore throat diameters of the shale matrix are in the range of 5 to 100 nm, with the most pore throat peaks between 10 and 15 nm (Nelson, 2009). Therefore, to improve the oil and gas recovery rate, hydraulic fracturing is conducted to enhance shale permeability (Soliman 1983; Poulsen and Soliman 1986; Hill et al., 2004).

As an important mechanical property for formation characterization and successful hydraulic fracturing design, fracture toughness is usually evaluated by diagnostic fracture injection testing (DFIT) on a field scale (Hagoort, 1981; Liu and Ehlig-Economides, 2018; Mayerhofer and Economides, 1993; Nolte, 1979, 1986; Soliman et al., 2005). DFIT, which is referred to as mini-frac, is used to estimate permeability and horizontal stresses by injecting a high-pressure fluid (Hagoort, 1981; Soliman et al., 2005). For this reason, injection is halted, and pressure decay is monitored.

Measuring core-scale properties provides more detailed information that is used for static and dynamic modeling (Lee et al., 2019). Core analysis accurately models the complex rock behaviors, such as mineralogical composition, pore-volume, fluid chemistry, capillary pressure, relative permeability, wettability, and geometry of the rock in the core plug, which may not be available from a field-scale measurement (Andersen et al., 2013; Gomes et al., 2007). In addition, large-scale measurements from static laboratory testing, such as triaxial compression (Aliha and Ayatollahi, 2013), or dynamic testing, such as seismic wave velocity (Crawford et al., 1995), often perform well in quantifying the failure of sample resistance. The only sources available in practice are usually drill cuttings that can be recovered abundantly during drilling operations (Tutuncu et al., 2005).

Cuttings provide valuable information about real-time drilling operations. Correct sampling and interpretation are keys to improving drilling performance and process efficiency (Karimi, 2013). Cuttings clarify some petrophysical parameters in shale affected by mud, where the presence of barite may obliterate the photoelectric index (Sherbeny et al., 2015).

Problem statement: The main problem with these common tests is that large samples are often unavailable. The standard experiments are also time-consuming and costly. The time required for conducting the standard measurement can be up to one and a half hours. Sample preparation requires 10 to 15 minutes, and setting up the sample takes 30 to 45 minutes. Cleaning up the device requires an additional 15 to 20 minutes. Running the experiment can take hours or days, depending on the size of the sample.



For nanoindentation, sample preparation and placement on the device take up to 17 and 10 minutes, respectively. The total time is about 30 minutes. There is an additional 10 to 15 minutes required for camera and tip calibration; however, these procedures are performed periodically as the camera is only calibrated to indent new material. Another advantage is that there is no need to clean up the device after completing the experiment. Running the experiment can take hours to days, depending on the number of indentations being applied on the surface of the shale.

Nanoindentation, which is non-destructive, is an appealing technique applicable to small samples (<1 in.). This technique allows cuttings to conveniently provide and map the mechanical properties of shale, such as Young's modulus and hardness. Its mapping capabilities allow the petroleum industry to characterize heterogeneity along the wellbore. Shale mechanical properties are of great importance in determining fracture toughness in accordance with Poisson's ratio for hydraulic fracturing design. They also contribute to drilling operations and wellbore stability (Asef, 2013).

Researchers have implemented nanoindentation to characterize composite materials (Brown et al., 2018), cement (Jennings et al., 2005), bone (Tai et al., 2006), and thin films (Nair et al., 2009). Nevertheless, the applications of nanoindentations for shale samples have remained limited (Abedi et al., 2016; Abousleiman et al., 2016; Sondergeld and Rai, 2019). This limitation is associated with the complex fracture patterns generated in shale (Gupta et al., 2020; Shukla et al., 2013).

## 1.2. Objectives

This dissertation has two main objectives for the geomechanical characterization of shale samples at the core scale using cuttings:

1. Determine Young's moduli of cuttings and compare the results with the core plugs.
2. Predict the anisotropic fracture toughness of the shale cuttings using nanoindentation.

## 1.3. Hypotheses

**Hypothesis 1:** I hypothesize that Young's modulus of shale on a core scale equals the average value obtained from nanoindentation at regular spacing, if the average value does not change significantly with the decrease in distance between indentations. A 20% difference is used as an engineering assumption in this study. The spacing must be larger than the plastic zone to avoid interference between the stimulated regions. The spacing between indents is included to use the smallest size possible.

**Test 1:** The first hypothesis is tested by comparing the average value of nanoindentation with an independent laboratory measurement of the core plug. This study shows that sample preparation plays an important role in nanoindentation. The sample surface is initially ground and polished to remove local defects. The load is then applied with regular spacing.

**Hypothesis 2:** I hypothesize that the shale matrix can be represented by two intertwined solid domains. One is weaker and fails when loaded, resulting in fractures,

whereas the other remains intact. The fracture toughness can be estimated by accounting only for the failure of the weaker domain. A fracture only occurs when the tip hits the weaker domain. This study proposes a conceptual model representing a shale matrix that comprises different minerals to form the grains. The boundary between the grains constitutes the weaker domain.

**Test 2 (same scale):** The second hypothesis is tested by comparing the predicted fracture toughness values using two tips, which are Berkovich and cube corner, with different topologies. The sample is indented following the hybrid grid system, in which various loads are applied at different locations to better characterize shale heterogeneity.

**Test 3 (independent validation):** The second hypothesis is also tested against an independent measurement to fully validate the proposed model. The cracked Chevron notched Brazilian disc (CCNBD) test is first used to obtain the fracture toughness at the core scale. Upon the completion of the CCNBD test, each core plug breaks and splits into two semicircular pieces. The semicirculars are then used for nanoindentation. Subsequently, the semicirculars are crushed, and the properties are characterized using the Berkovich tip.

## **1.4. Contribution to knowledge**

This dissertation has two major contributions, which are:

1. A new method to determine Young's modulus of the shale samples on a core scale using cuttings. This would investigate Young's moduli of the shale cuttings and provide the sensitivity of sample preparation.

2. A conceptual model based on the effective medium theory to characterize the anisotropic fracture toughness of shale. This would clarify the complexities of fracture patterns by applying various loads on the surface of shale.

## **1.5. Summary of chapters**

In Chapter 2, the fundamental concepts of fracture toughness, including the modes and types of fracture and standard measurement, are presented. Then, the application of nanoindentation is discussed, including the tip geometries, load-displacement curve, indentation modulus and hardness, benefits of nanoindentation over atomic force microscopy (AFM) and various sources of errors affecting nanoindentation results. This research focuses on shale samples and will cover their importance and behavior as well as two basic equations for calculating their fracture toughness.

In Chapter 3, a new method is proposed to determine Young's modulus of the Wolfcamp Formation on a core scale using cuttings. To define the scale of the cuttings, the method accounts for the spacing between the indentations and applied load. A review of nanoindentation and the sensitivity of the required sample preparation at different stages are presented. The predicted Young's moduli of the shale cuttings using nanoindentation are tested against the independent laboratory measurements.

In Chapter 4, a proposed conceptual model based on the effective medium theory to characterize shale fracture toughness using nanoindentation is introduced. The complexities of induced fracture patterns are discussed. Various loads at different locations are applied to define the acceptable load ranges to sufficiently induce simple

fractures where the linear elastic fracture mechanics are realistic. Finally, the predicted fracture toughness values obtained from the Berkovich tip are compared with the cube corner for partial validation.

In Chapter 5, the predicted anisotropic fracture toughness values of the shale core plug and cuttings using nanoindentation are validated with the CCNBD test. The CCNBD approach is used to measure the shale samples, which turn out to be halved (semicircular). The semicircular samples are then tested using nanoindentation. Afterward, the samples are crushed to represent smaller pieces of shale that are found more frequently. Finally, the cuttings are evaluated for fracture toughness characterization using nanoindentation. The difference between the fracture toughness values of each sample from the nanoindentation and the CCNBD test is obtained.

The assumptions and limitations of the indentation technique to determine Young's modulus at the core scale using drill cuttings and the proposed conceptual model are discussed in Chapter 6. This chapter investigates the limitations of applying small pieces in nanoindentation. For completeness, the anisotropic behavior, fluid-rock interactions, and application to other formations are included.

The conclusions are presented in Chapter 7. A promising new method is proposed for determining Young's modulus of shale cuttings using nanoindentation. Furthermore, the proposed model can determine the anisotropic fracture toughness of shale at the core scale using cuttings. Recommendations for future work are also provided.

## **CHAPTER 2. LITERATURE REVIEW**

### **2.1. Importance of shale**

Over the past decades, the petroleum industry has been extracting natural gas and oil from shale formations (Soliman, 1986; Morsy et al., 2013; Sheng et al., 2014; Hughes, 2013). Mineral identification by x-ray diffraction in shale poses major challenges, as the effects of diagenesis and metamorphism may occur (Roberts and Elmore, 2018). Shale comprises multiple phases of clay, carbonate, and quartz, including mica, aluminosilicate, and sulfide, with fewer mineral contents (Raven and Self, 2017). It also contains organic matter, such as kerogen, that generates oil when subjected to intense heat and overburden pressure. The structure of shale is laminated (Gu, 2018) or fissile, and it tends to split into thin layers in the direction parallel to the bedding planes or even break down into pieces, depending on the brittleness level.

The complexity of shale's mineralogical composition and structures may significantly impact oil or gas recovery (Grim, 1947). The decline of oil and gas production rates with the increasing price of conventional reservoirs makes alternative hydrocarbon sources of unconventional reservoirs, such as shale, tight sands, and coal beds, attractive (Höök et al., 2014). Shale gas and oil development are expected to significantly enhance the energy reserves of the United States (US) through horizontal drilling (Campbell, 1891) and multistage hydraulic fracturing (Soliman et al., 1990; Daneshy, 2003).

According to the US Energy Information Administration (EIA) (2013), 42% of total world resources are identified as shale formations. The US is ranked fourth for shale gas and second for shale oil among 41 countries worldwide. Although more prospective shale formations are assessed outside the US, none of them produce shale oil and gas in commercial quantities as the US does. In 2020, the EIA estimated that shale oil resources still dominated about 65% of total US oil production. The global shale gas market is predicted to grow by 10.7% after companies recover from the COVID-19 impact that resulted in operational challenges (Market Report, 2021).

## **2.2. Why is fracture toughness important?**

Hydraulic fracturing requires a deep knowledge of the stress field distribution to artificially create a fluid flow pathway into the wellbore (Thiercelin, 1989). The treatment works by applying sufficient pressure to fracture the formation. The horizontal wells are placed in the direction of minimum horizontal stress with the intention of hydraulic fracturing in the direction of maximum horizontal stress. The aims are better reservoir contact and production. For a successful hydraulic fracturing design, the fracture toughness value is crucial for the mechanical properties, usually evaluated on a core and field scale (Arora and Cai, 2014; Liu and Economides, 2018).

### **2.2.1. Fundamental concepts of fracture toughness**

Fracture mechanics is the field of mechanics that studies fracture propagation in samples. Researchers have investigated the possibilities of fracture growth rates and mechanisms in various conditions. The basic theory of linear elastic fracture mechanics

(LEFM) was first developed by Griffith (1920), then modified by Irwin (1957) because of plastic deformation at the fracture tip per unit surface area that was introduced as a critical stress intensity factor.

A stress intensity factor characterizes the stress state near the fracture tip in brittle materials where the fundamental assumptions of LEFM remain valid and specific conditions are met. LEFM is applicable if all materials are elastic except a small size of the inelastic region in the vicinity of the fracture tip. A stress intensity factor is a function of applied stress, induced fracture length, and fracture patterns as (Irwin, 1957)

$$\text{Stress intensity factor} = Y \sigma \sqrt{\pi a_I}, \quad (2.1)$$

where  $\sigma$  is the applied stress,  $a_I$  is the fracture length, and  $Y$  is the geometry factor, which is a dimensionless number with the values zero to 10 (Tada et al., 2000). The geometry factor depends on the fracture topology and its orientation to the applied load.

### **2.2.2. Modes and types of fracture**

There are three fundamental fracture modes, and their mixture is often described as mixed mode. At the fracture tip, the stress field is categorized into a mode I, mode II, and mode III (Figure 2.1). In mode I (Figure 2.1a), the fracture plane is perpendicular to the normal face and results in pure tensile. In mode II or sliding mode (Figure 2.1b), the fracture occurs under the action of shear stress and propagates in the same direction (in-plane). In mode III or tearing mode (Figure 2.1c), the fracture occurs in shear mode and propagates in the direction perpendicular to the shear (out-of-plane).



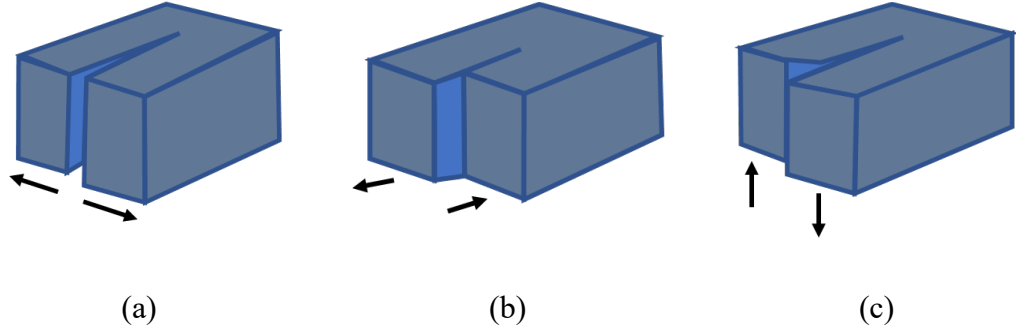


Figure 2.1—Modes of fracture are classified into (Irwin, 1968): (a) mode I or pure tensile, (b) mode II or in-plane shear, and (c) mode III or out-of-plane stress.

Mode I is the most common method for more reliable results. It often creates more damage and receives the most attention in research. Mode II does exist, but the result is not reliable as mode I. There are only a few applications of mode III because it does not occur as often as the other two modes (Griffith, 1920; Westergaard, 1939). The International Society for Rock Mechanics (ISRM, 1978) recommended different approaches to determine rock fracture toughness based on modes I, II, and III, as listed in Table 2.1. Irwin (1958) proposed that the stress at the fracture tip was a function of the applied stress and the fracture tip as

$$K_{IC} = Y \sigma_{\max} \sqrt{\pi a_I}, \quad (2.2)$$

where  $\sigma_{\max}$  is the maximum applied stress when the fracture occurs,  $a_I$  is the fracture length, and  $Y$  is the geometry factor, which is a dimensionless number with values of zero to 10 (Tada et al., 2000).

Table 2.1—The experimental methods to evaluate rock fracture toughness in different modes.

Mode	Test methods	Reference
I	Chevron Bend (CB), Short Rod (SR), Cracked Chevron Notched Brazilian Disc (CCNBD)	Gokaraju et al. (2017)
II	Compressive Shear (CS) or Shear Box (SB), Punch-Through Shear with Confining Pressure (PTS-CP), and Modified Punch-Through Shear with Confining Pressure (MPTS-CP) as a rectangular version of PTS-CP	Backers et al. (2002); Vizini and Futai (2021)
III	Edge Crack Torsion (ETC), Edge Notched Disc Bend (ENDB), Notched Cylinder subjected to torsion	Aliha et al. (2015); Pietras et al. (2020)

Ashby (1999) postulated that fracture toughness values vary up to four orders of magnitude over a broad number of materials, with the highest value of  $175 \text{ MPa.m}^{1/2}$  for steels and the lowest value of  $0.1 \text{ MPa.m}^{1/2}$  for polymers and foams. Several investigations have been performed to evaluate factors affecting the fracture toughness of coal measures of sandstones (Singh and Sun, 1990), polymer composites (Sharafi et al., 2021), aluminum alloys (Hahn and Rosenfield, 1975), natural composites (Al-Maharma and Sendur, 2018), and shale (Chandler et al., 2016; Gupta et al., 2020). The major factors controlling fracture toughness are temperature, strain rate, impact

strength, ductility, stress concentration, and specimen size (Anderson, 1991; Ayatollahi and Akbardoost, 2012). Understanding these factors help predict fracture height and width (Gokaraju et al., 2017).

There are two types of fractures in materials divided into brittle and ductile. These characteristics are defined depending on their ability to undergo plastic deformation prior to fracture. A brittle fracture involves an unstable fracture propagation with negligible or no plastic deformation, thus requiring a small energy absorption. Fractures may propagate through the grains (trans granular) or along the grain boundary (intergranular). They often occur unexpectedly.

In comparison, a ductile fracture requires more strain energy to induce a fracture because of the excessive amount of plastic deformation. As a result, the fracture propagation tends to be stable and slow. Ductility is a function of stress state, strain rate, and temperature. Two quantifications of ductility are the reduction and elongation of the area (Anderson, 1991).

### **2.2.3. Cracked Chevron notched Brazilian discs (CCNBD)**

This study uses the CCNBD test (see Figure 2.2 for schematic) as an independent laboratory measurement to test the second hypothesis. Out of the three methods suggested by the ISRM, the CCNBD test is the most advantageous because it consistently requires the least amount of sample preparation and its failure to create fractures (Aliha and Ayatollahi, 2013; Aliha et al., 2018). Furthermore, it entails simple geometry and demonstrates flexibility in setting up the sample between two flat platens.

In addition, it introduces pure mode I or pure mode II by adjusting the fracture orientation relative to the applied compressive load (Berto and Ayatollahi, 2011).

The initial notch is created in ceramic, graphite, and rock because of the difficulties in generating fractures (Ouchterlony, 1988). The fracture toughness based on CCNBD is expressed as (Fowell, 1995)

$$K_{IC} = \frac{F_{max}}{B\sqrt{D}} Y_{min}^*, \quad (2.3)$$

where  $K_{IC}$  is the fracture toughness of pure mode I,  $F_{max}$  is the applied compressive load,  $B$  is the sample thickness,  $D$  is the sample diameter, and  $Y_{min}^*$  is the dimensionless critical stress intensity factor.

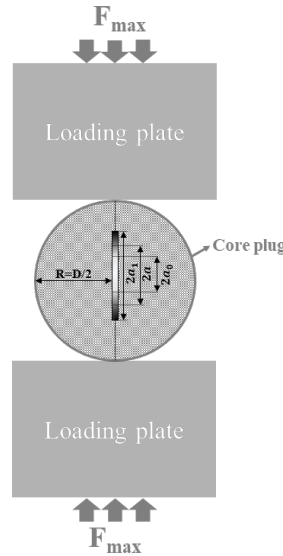


Figure 2.2—The loading fixture for pure mode I (Fowell, 1995).

#### 2.2.4. Heterogeneity and anisotropy in shale

Heterogeneity is defined as the variability or complexity of system properties as a function of spatial locations, which arises at all length scales attributed to mineralogy

and lithology, rock facies, and pore types (Fitch et al., 2013). The mineralogical heterogeneity in shale leads to difficulties during sample preparation. The soft minerals (Du et al., 2018) tend to detach during the grinding or polishing stage, whereas the hard minerals are easier to prepare. The finished surface aims to reach a higher level of smoothness to lower standard deviations of the resulting Young's modulus and hardness.

While anisotropy is a material property with a directionally dependent value, it has unique physical properties along different axes. In shale, anisotropy is a direction-dependent intrinsic property from the oriented clay platelets or fractures in shale and the distribution of organic matter (Fjær and Nes, 2014). The platelet orientations occur during or after deposition processes, such as burial and diagenesis. Anisotropy affects aspects of shale development, such as reservoir characterization (Sone and Zoback, 2013), in-situ stress estimation (Khan et al., 2011), wellbore stability analysis (Lee et al., 2012), hydraulic fracturing design (Serajian and Ghassemi, 2011), and seismic imaging (Zhang et al., 2018). Notch direction and fracture propagation describe three principal orientations that indicate shale anisotropy, as shown in Figure 4.12.

Shale heterogeneity and anisotropy are generally subject to an in-situ stress state. The in-situ stress is affected by overburden pressures and maximum and minimum horizontal stresses and results in different values in various directions. Those characteristics represent significant challenges in quantifying shale mechanical properties. The properties provide insight into hydraulic fracturing performance in shale formations (Tang et al., 2018).

### **2.2.5. Fracture toughness in shale**

Organic matter, rock properties, and clay minerals distinguish shale behaviors from other homogeneous materials, such as metal, ceramic, polymer, and composite. The properties of shale, such as Young's modulus and hardness, and its mineralogy substantially control fracture toughness. For instance, shale with higher porosity, clay content, and total organic carbon has lower Young's modulus, which leads to small fracture toughness values (Gupta et al., 2020). In addition, shale anisotropy significantly contributes to predicted fracture toughness in different directions (Chandler et al., 2016).

Mineralogical variability causes mechanical instability in the behavior of shale, which results in the samples easily breaking into pieces. Thus, recovering large samples for standard mechanical testing is challenging and expensive. The only sources often available in practice are drill cuttings that can easily be retrieved during drilling operations (Tutuncu et al., 2004). As a result, indentation has become a popular method for capturing the mechanical properties of shale from small pieces (Cheatham and Gnirk, 1967; Maurer, 1967; Simon, 1967; Mishnaevsky, 1995; Alehossein and Hood, 1996; Oliver and Pharr, 2004).

Nanoindentation provides valuable information on mechanical properties (Abedi et al., 2016; Xiang et al., 2017), such as Young's modulus (Sneddon, 1965), hardness (Doerner and Nix, 1986), fractures (Lawn et al., 1980), shear modulus (Sinha et al., 2019), creep (Acosta et al., 2021), and the fracture toughness (Laugier, 1987; Gupta et al., 2018) of samples. Fracture toughness is estimated by accounting for the

induced fracture length for a given maximum applied load based on LEFM (Griffith, 1920; Shukla et al., 2013). However, current studies have remained limited to ideal (symmetrical) fracture patterns (Ponton and Rawlings, 1989a, 1989b; Dukino et al., 1992) induced in homogeneous materials, such as fused silica (Shukla et al., 2013) and aluminum (Gouldstone et al., 2000). Indentations lead to complex fracture patterns in shale, which pose difficulties in characterizing fracture length and toughness (Gupta et al., 2020).

### **2.3. Fundamental concepts of nanoindentation**

Contact mechanics refers to the mechanical behavior of two bodies brought in contact. In the nineteenth century, Hertz first studied the nature of the contact between an indenter tip and a flat surface in an analytical solution as a foundation of nanoindentation measurement. The Hertzian theory assumes that the contact area is elastic and much smaller than the contacting bodies (Johnson, 1985). Each body is considered an elastic half-space, and the surface is frictionless (Popov, 2010), as shown in Figure 2.3.

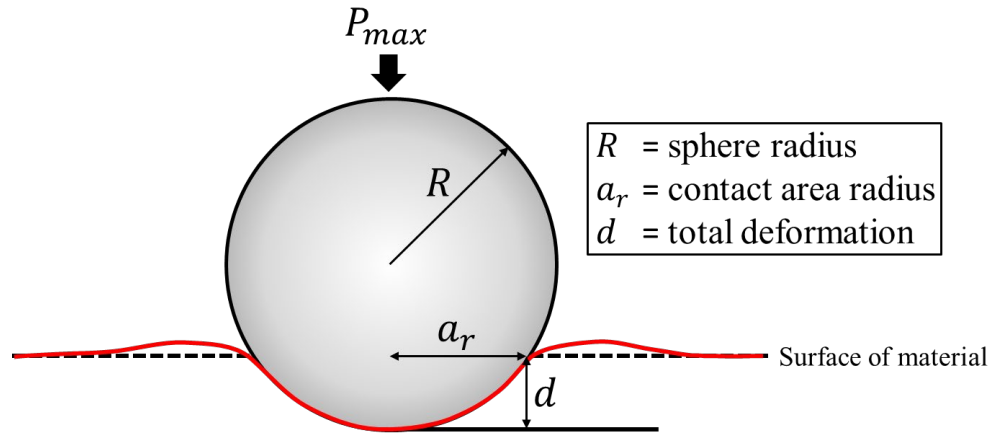


Figure 2.3—Contact of a rigid indenter with a flat material.

In the classical sense, the indentation stress field provides insight into aspects of the indentation process, such as yielding and fracturing (Oliver and Pharr, 1992). The stress fields are assumed to be purely elastic and described in closed form for various indenter geometries (Fischer-Cripps, 2011). The indentation process is commonly an ideal elastic-plastic one, and the presence of plastic deformation complicates the behavior. Indentation techniques are typically used to measure the hardness that represents the least value of pressure beneath a spherical indenter at the center of the contact area (Hertz, 1881). Indentation testing may also investigate fracture toughness, strength, and internal residual stresses.

In 1925, Brinell introduced a test to determine the hardness of a given material; this was later referred to as the Brinell hardness test. In this test, a carbide ball is pressed into a surface with an accurately controlled test load (Brinell, 1925). It is commonly used to characterize materials that are coarse or rough, such as castings and forgings, and usually applies a high load of 500 kgf and 3000 kgf for non-ferrous materials and



steels, respectively. There are other Brinell scales with loads as low as 1 kgf and 1 mm diameter indenters, but those are not frequently used. The Brinell test is applied to a wide range of metallic material.

For brittle materials such as ceramic or glass, the indentation hardness is also called the apparent hardness,  $H$ , which is less than the true hardness because it measures an ideal elastic-plastic deformation (Marshall and Lawn, 1985). There is little elastic deformation, as shown in Figure 2.4a. The apparent hardness corresponds to the true hardness when the material behavior is an ideal rigid plastic, such as steel and copper, as illustrated in Figure 2.4b (Atkins and Tabor, 1965).

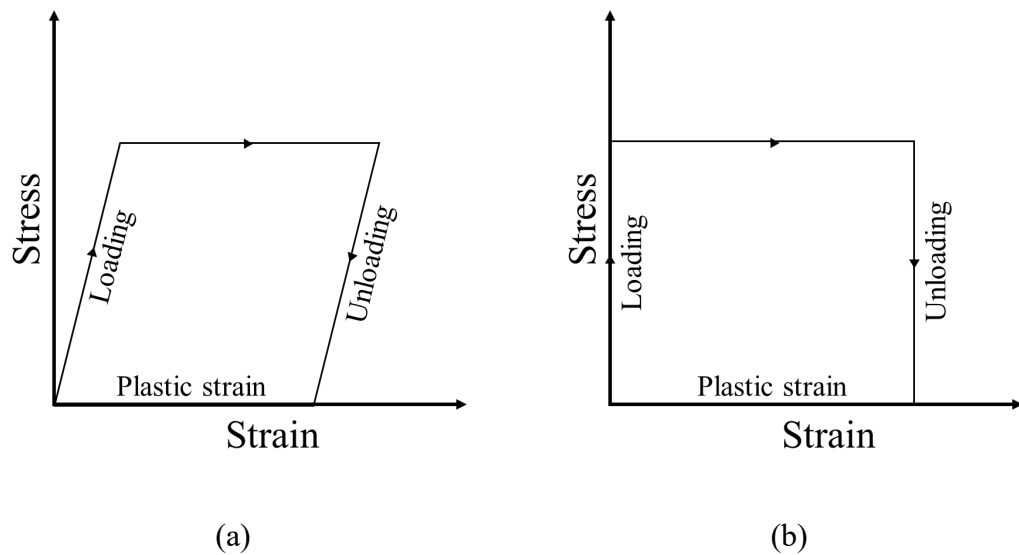


Figure 2.4—Type of stress-strain behavior (Fischer-Cripps, 2011) in materials, such as ideal elastic-plastic (a) and rigid-plastic (b).

In nanoindentation, an indenter tip with known mechanical properties probes the shale samples, and their properties are unknown by applying well-controlled contact forces. The procedure characterizes the mechanical properties of samples, such as

Young's modulus and hardness, from the load-displacement curve (Pharr et al., 1992). The indenter tip geometries vary, as discussed in the following section.

### **2.3.1. Indenter tip geometries**

The known geometry of the indenter tip—generally spherical, conical, or pyramidal—defines the size of the contact area. Conical and pyramidal tips are sharp, easily constructed to meet a single point, and self-similar while indenting a half-space. They perform permanent deformations (irreversible) after contact or load removal (Pharr et al., 1992). A spherical indenter, categorized as having a blunt tip, offers a smooth transition from elastic to elastic-plastic contact and is suitable to indent soft materials (Fischer-Cripps, 2011).

Sharp tips are classified as three-sided or four-sided indenters. For example, Berkovich and cube-corner tips are considered three-sided indenters, whereas Vickers and Knoop are four-sided indenters. This study used Berkovich and cube-corner tips to test the proposed conceptual model (Esatyana et al., 2021). The Vickers tip was also applied, but it did not create easily identifiable fractures. Other geometries, such as cone and sphere, are not used in this work. It is challenging to manufacture conical diamonds with sharp tips, whereas the contact stresses are initially small and only produce elastic deformation for the spherical indenter (Fischer-Cripps, 2011).

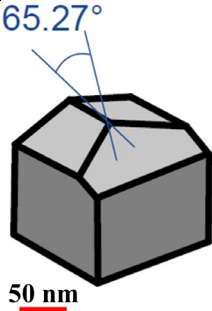
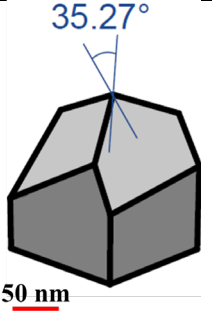
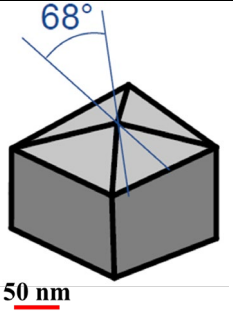
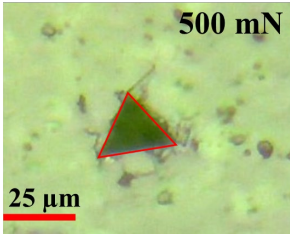
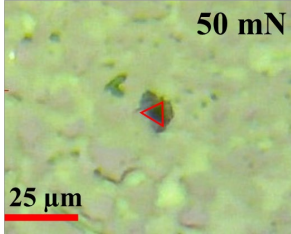
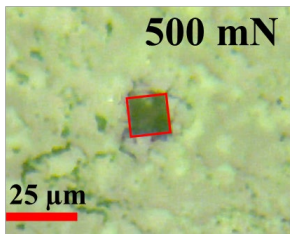
Berkovich—a scientist from Russia—invented the Berkovich tip (1951). It is so it is fairly easy to create the three-sided geometry with a sharp tip. The tip maintains a self-similar geometry at small scales and induces plasticity even at small loads; the large

angle of  $65.27^\circ$  minimizes the influence of friction (Berkovich, 1951; Rother et al., 1998). The Berkovich tip is used to characterize materials and films thicker than 100 nm (Khrushchov and Berkovich, 1951).

The cube-corner tip is a three-sided pyramid with mutually perpendicular faces arranged in geometry like the corner of a cube (Marshall et al., 1980; Rother et al., 1998). The centerline angle is  $35.27^\circ$ . This sharp tip produces much higher stresses and strains in the projected area (Marshall et al., 1980), and is beneficial for generating small and well-defined fractures in brittle materials.

A typical range of the tip radius for the new Berkovich and the cube-corner tip is in the order of 50 to 100 nm. The indenter tips are based on contact geometry, projected area, semi-angle, effective cone angle, and geometry factor (Fischer-Cripps, 2011). The impression sizes vary depending on the applied load. The properties of the Berkovich, cube-corner and Vickers tips are provided in Table 2.2.

Table 2.2—Summary of the indenter tip properties and their impressions on the shale surface. The cube-corner tip has a smaller applied load than the other tips because it has a sharp contact angle.

Indenter type	Berkovich	Cube-corner	Vickers
Geometric shapes	Three-sided	Three-sided	Four-sided
Projected area, $A_c$	$3\sqrt{3}h_c^2 \tan^2\theta$	$3\sqrt{3}h_c^2 \tan^2\theta$	$4h_c^2 \tan^2\theta$
Contact angle, $\alpha$	$65.27^\circ$	$35.27^\circ$	$68^\circ$
Effective cone angle, $\Psi$	$70.3^\circ$	$42.28^\circ$	$70.3^\circ$
Geometry correction factor, $\beta$	1.034	1.034	1.012
Indenter tip geometry			
Impression on the surface of shale			

### 2.3.2. Load-displacement curve

Nanoindentation provides real-time load-displacement data while indenting the sample surface. This study employed sharp indenters with three-sided geometry, such as the Berkovich and cube-corner tips. Figure 2.5 delineates an indentation movement and pinpoints several parameters used in the analysis.

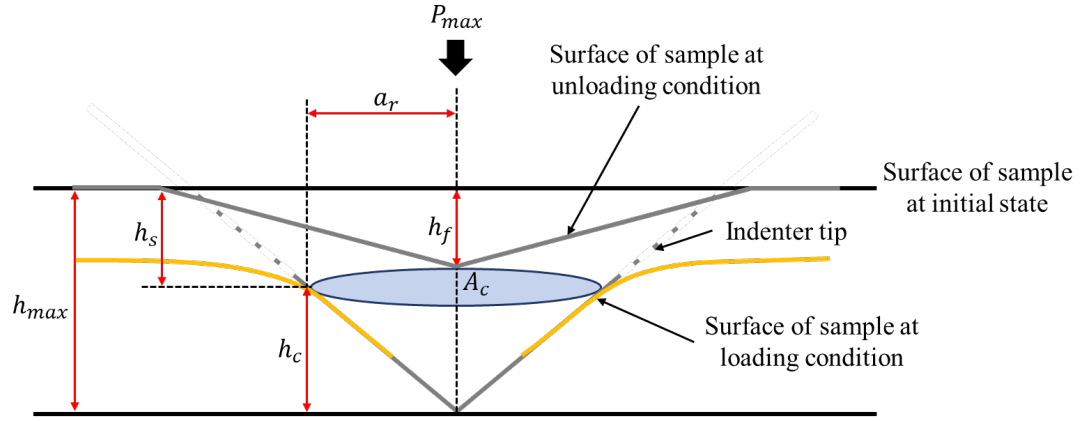


Figure 2.5—A schematic of an indentation movement with various parameters involved in the analysis (Oliver and Pharr, 1992).

where  $h_{max}$  is the maximum indentation depth,  $h_s$  is the surface displacement at the contact perimeter,  $h_c$  is the contact depth or penetration depth of the elastic contact,  $a_r$  is the contact area radius,  $h_f$  is the final depth where the elastic displacements are recovered, and when the indenter tip is fully withdrawn (upon unloading),  $A_c$  is the projected area, and  $P_{max}$  is the maximum applied load. The maximum indentation depth is determined as

$$h_{max} = h_s + h_c. \quad (2.4)$$

The projected area depends on the geometry of the indenter tips, and for the Berkovich and cube-corner is expressed as (Oliver and Pharr, 1992)

$$A_c = 3\sqrt{3}h_c^2 \tan^2 \theta, \quad (2.5)$$

where  $\theta$  is the face angle with the central axis of the indenter or semi-angle. The semi-angle equals  $65.27^\circ$  for the Berkovich tip and  $35.26^\circ$  for the Cube corner.

The penetration depth depends on the applied load (Figure 2.6) and can be expressed as

$$h_c = h_{max} - \varepsilon \frac{P_{max}}{S}, \quad (2.6)$$

where  $\varepsilon$  is the intercept factor (Pharr and Bolshakov, 2002), and  $S$  is the slope, which is equal to  $\frac{dP}{dh}$  obtained from the unloading portion. The Berkovich, cube-corner, and Vickers tips' intercept factor is 0.75, while for the conical indenter, the value is 0.72 (Oliver and Pharr, 1992).

The experimental work begins when the load is applied to the indenter tip, increased from zero to a maximum value, and reduced to zero. The actuator mainly performs nanoindentation. For instance, it attaches the tip, applies the load, and controls the movement, as depicted in Figure 2.6.

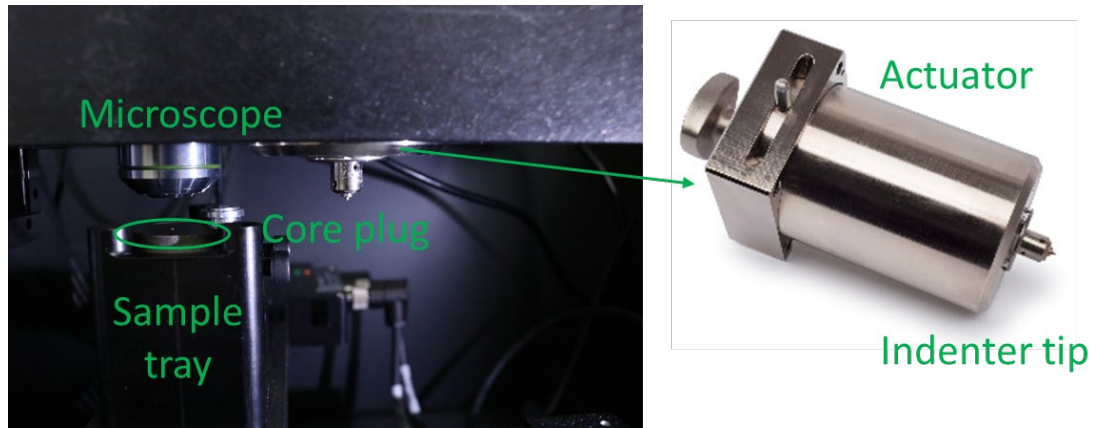


Figure 2.6—The nanoindenter features that perform indentation testing.

The load-displacement curve varies, depending on the maximum applied load, types of samples, and indenter tip. Typically, higher loads and sharper tips result in an extensive penetration depth. The mechanical properties of the sample, such as Young's modulus and hardness, are characterized by analyzing the load-displacement curve, as shown in Figure 2.7.

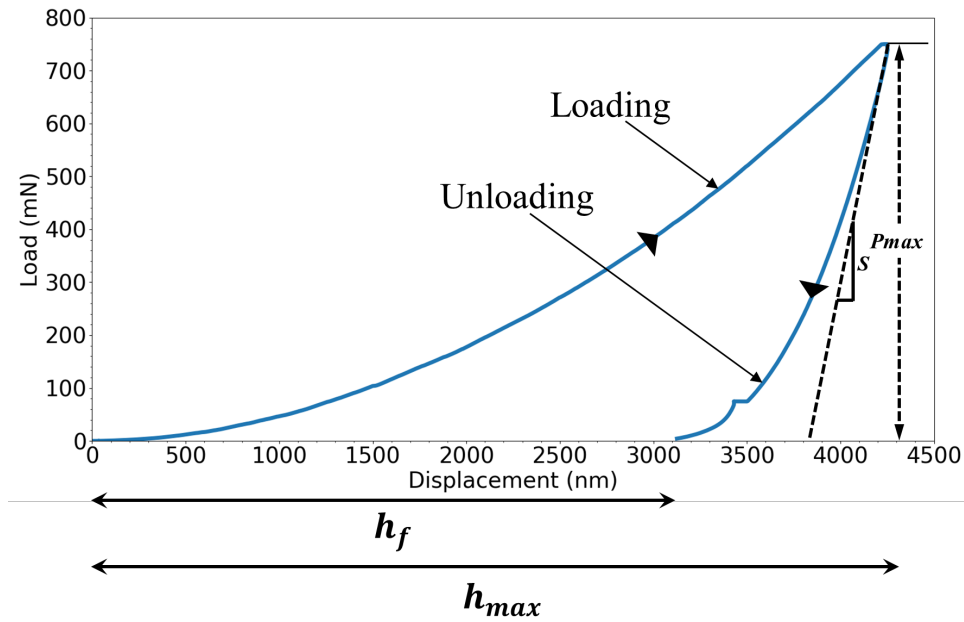


Figure 2.7—A typical load-displacement curve obtained from nanoindentation (ISO 14577). The slope on the unloading part is used to characterize the mechanical properties.

### 2.3.3. Indentation modulus and hardness

The variation of the load-displacement curve offers a valuable tool for calculating the indentation modulus (Oliver and Pharr, 1992)

$$E_r = \frac{S}{2\beta} \sqrt{\frac{\pi}{A_c}}, \quad (2.7)$$

where  $E_r$  is the reduced modulus,  $S$  is the slope of load versus displacement at the beginning of unloading, and  $\beta$  is the shape factor or geometric parameter. The shape factor is equal to 1.03 for the Berkovich tip, and other geometries are reported in the literature (Cheng and Cheng, 1998).

The reduced modulus is a function of the modulus and Poisson's ratio of both the sample and indenter tip. Oliver and Pharr (2004) estimated the sample modulus by accounting for the reduced indenter modulus as

$$\frac{1-\nu_s^2}{E_s} = \frac{1}{E_r} - \frac{1-\nu_i^2}{E_i}, \quad (2.8)$$

where  $\nu_s$  is the sample Poisson's ratio,  $E_s$  is the sample Young's modulus,  $\nu_i$  is the indenter tip Poisson's ratio, and  $E_i$  is Young's modulus of the indenter tip. The right side of the second term is usually negligible because the  $E_i$  value is much higher than  $E_s$ .

The indenter tip is made of a diamond with a typical Young's modulus of 1140 GPa and Poisson's ratio of 0.07 (Klein and Cardinale, 1993). For most rock types, the Poisson's ratio is usually between 0.25 and 0.3, which is more representative of shale (Sone and Zoback, 2013). Therefore, changing the Poisson's ratio by 0.1 would alter the results by less than 0.01 as

$$\Delta E_s \approx E_r(1 - \Delta \nu_s^2). \quad (2.9)$$

The reduced modulus obtained from indentation testing varies depending on the sample. In this example, the values captured from the shale samples range from 60 to 95 GPa (Esatyana et al., 2020). The hardness is determined from the unloading portion as



$$H = \frac{P_{max}}{A_c}. \quad (2.10)$$

Table 2.3 represents the difference between the predicted Young's modulus of shale,  $E_s$ , and the reduced modulus,  $E_r$ , is between 1.31% and 1.81%. With that being said, the reduced modulus can be directly implemented to determine fracture toughness.

Table 2.3—Typical interpreted Young's moduli calculated from the shale samples and indenter tips.

$E_s$ (GPa)	$\nu_s$	$E_r$ (GPa)	$\nu_i$	$E_i$ (GPa)
59.21	0.25	60	0.07	1140
96.72	0.25	95	0.07	1140

#### 2.3.4. Atomic force microscopy (AFM) versus nanoindentation

The objectives of AFM and nanoindentation are to measure mechanical properties by indenting the sample's surface. AFM topographic imaging provides a three-dimensional surface profile of sample structures in high spatial resolution (Engel and Muller, 2000) to map chemical and physical properties and molecular interactions (Alsteens et al., 2017). The required samples are often soft and thin in the order of a few nanometers (Park et al., 2004). In AFM, the indenter tip is mounted on a cantilever, which governs the movement in an up or down direction. The cantilever has multiple degrees of freedom while moving down to the surface by a piezo transducer.

AFM has some drawbacks for several reasons (Griepentrog et al., 2013). First, the AFM tip radius, ranging from a few through 10 nanometers, causes difficulties in measuring exact dimensions and shapes (Cappella and Dietler, 1999). Second, the

cantilever can twist if the tip deforms and cause undesirable motions while analyzing the tip-sample contact. Thus, AFM measurement is challenging and time-consuming (Grienpentrog et al., 2013).

Conversely, nanoindentation covers larger areas than AFM to perform hundreds of tests with micron spatial resolution on a small sample size. Furthermore, the indentation technique represents the variability across the sample for heterogeneous materials. Each indent accurately captures the load-displacement curve to determine Young's modulus and hardness and indirectly measure fracture toughness. To measure the impression of the indentation does not require a powerful microscope because the contact area is measured with the indentation depth and tip geometry.

### **2.3.5. Various sources of errors affecting nanoindentation data**

Errors can lead to misleading conclusions, which are inevitable in any scientific experiment, including nanoindentation. Therefore, several issues affecting nanoindentation and the potential remedies will be discussed here. The potential remedies are important to gain more confidence in the resulting data.

First, the nanoindenter device is sensitive to vibration and shocks, including air current or noise. Noise could come from the surrounding area, such as people walking or talking in front of the laboratory. Thus, the device is usually placed on an anti-vibration table made of steel. The table is designed with a sturdy framework for a remarkably reliable vibration prevention system (Nohava et al., 2009).

Second, experimental research findings reveal that surface roughness lowers the sample resistance and reduces Young's moduli obtained from nanoindentation (Esatyana et al., 2020). Surface roughness represents the relation between indentation depth and the measured properties (Miller et al., 2008), including the contact area between the indenter tip and sample surface (Jiang et al., 2008). The Oliver and Pharr (1992) method assumed a perfectly flat and smooth surface for indentation analysis. Therefore, it is recommended to properly prepare the sample before indentation testing and quantify the surface roughness value to provide more information. Sample preparation consists of grinding and polishing the stages to achieve a smooth and shiny sample surface (Esatyana et al., 2020).

Third, the pile-up and sink-in phenomena depend on the material, indenter tip, and applied load. The sample surface is typically drawn inwards underneath the indenter in an elastic material known as a sink-in. Meanwhile, the material may either pile up or sink in around the impression in the plastic material. Tabor (1950) concluded that piling up and sinking in have detrimental impacts on contact area determination. Large and little dislocations are found in the crystal structure concerning the indenter tip; the resulting errors in the contact area are up to 60% (Bolshakov and Pharr, 1998). A procedure for accounting for piling-up and sinking-in effects based on contact stiffness and high-resolution images is required (McElhaney et al., 1998).

In addition to the sources of errors mentioned above, the indentation size effect (ISE) is often overlooked with the association to the area function (Li et al., 1993). The ISE indicates that hardness tends to increase with decreasing indentation depth. For

conical and pyramidal indenters, the phenomenon becomes important at indentation depths of less than 1 micron (Pharr et al., 2010). For spherical indenters, higher hardness is produced when the diameters of the spheres are less than 100 microns. The presence of thin oxide films, residual stresses, strain hardening, and friction between the indenter and material lead to the ISE (Li et al., 1993). The indentation of hard materials and proper sample preparation diminish the significance of the ISE (Fischer-Cripps, 2011).

## **2.4. Fracture toughness measurements using nanoindentation**

Nanoindentation is an ideal tool to indirectly determine fracture toughness over localized areas at small loads. The maximum load is equal to 1,100 mN. The fracture length emanating from a local indentation impression on the surface determines fracture toughness (Sebastiani et al., 2015). However, a significant portion of the induced fracture under the sample surface is difficult to map, which creates another challenge in characterizing fracture patterns after indentation (Gupta et al., 2020). The inability to generate fractures with easy-to-map patterns has limited the number of relations available for indentation techniques.

The governing relation is easier to derive when the fracture pattern is defined by analytical and numerical methods (Tada et al., 2000). The Palmqvist or radial fractures (Figure 2.8a) occur on the surface (visible) and extend shallowly downward into the material (invisible) by hoop stress. Lateral or horizontal fractures (Figure 2.8b) are generated by tensile stress beneath the material surface. Median fractures (Figure 2.8c) are created underneath the surface where the direction is located at the corner of the

residual impression. Half-penny fractures (Figure 2.8d) may extend upward and join radial fractures that intersect at the surface. The creation of fracture patterns is sensitive to experimental conditions. The variability of fracture patterns based on the Vickers indenter in homogeneous materials is shown in Figure 2.8 (Cook and Pharr, 1990).

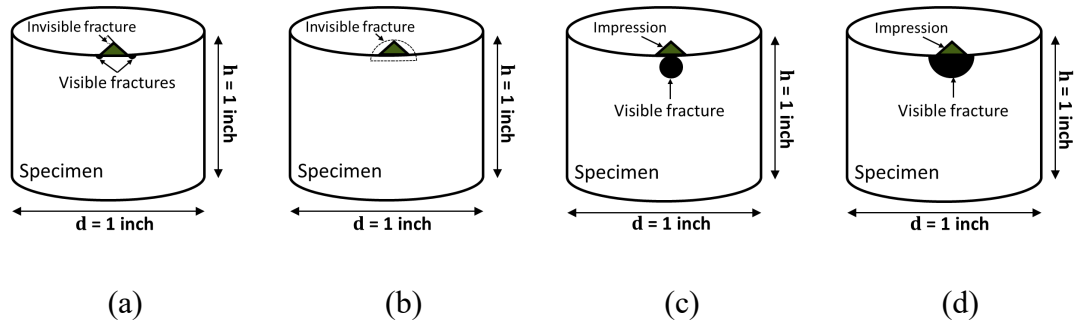


Figure 2.8—Schematic of potential fracture patterns (Fischer-Cripps, 2011) where analytical relations were developed, such as Palmqvist or radial (a), lateral (b), median (c), and half-penny fractures (d).

There are two methods for fracture-toughness characterization in homogenous media based on nanoindentations (Liu, 2015). They are known as the fracture length (Laugier, 1987) and the energy release rate methods (Griffith, 1920). The two methods are discussed subsequently.

#### 2.4.1. Fracture-length method

Fracture toughness refers to a material's property that evaluates its resistance to fractures when the load is applied. The indentation technique measures the fracture length generated by a sharp tip. The fracture length is an essential parameter to directly quantify fracture toughness. The approach is known as the fracture length method.

In 1980, the Lawn-Evans-Marshall (LEM) model introduced elastic-plastic indentation damage in ceramic and glass for the median or radial fracture system. Following that, the evaluation of the indentation technique was developed to directly measure fracture toughness. A simplified fracture toughness analysis was modeled subject to long fractures ( $c/a \gg 1$ ) and treated as a half-penny fracture. The equation is as (Anstis et al., 1981)

$$K_c = \alpha \left( \frac{E_s}{H} \right)^{\frac{1}{2}} \frac{P_{max}^{\frac{3}{2}}}{c^2}, \quad (2.11)$$

where  $K_c$  is the fracture toughness,  $\alpha$  is an empirical coefficient,  $E_s$  is Young's modulus of the sample,  $H$  is the hardness,  $P_{max}$  is the maximum applied load, and  $c$  is the fracture length. The empirical coefficient value varies depending on the tips. For the Berkovich tip, the value is 0.016 (Dukino and Swain, 1992), and it is 0.032 (Ast et al., 2019) for the cube-corner tip. In nanoindentation, only one value of Young's modulus is captured on each test, resulting in an isotropic Young's modulus. Nevertheless, fracture toughness is anisotropic due to the presence of defects in different directions.

Calibration was performed using the data from Anstis et al. (1981), which showed a small coefficient of variation. Unlike glass, induced fractures in ceramic are more realistic to form the Palmqvist type (Laugier, 1986). Nevertheless, fracture toughness analysis based on half-penny fractures is reliable for developing a novel analytical approach to Palmqvist fractures proposed by Laugier (1987) as

$$K_c = \alpha \left( \frac{a}{l} \right)^{\frac{1}{2}} \left( \frac{E_s}{H} \right)^{\frac{2}{3}} \frac{P_{max}^{\frac{3}{2}}}{c^2}, \quad (2.12)$$

where  $a$  is the distance from the indented center to the corner, and  $l$  is the distance from the indented corner to the fracture tip. The term of  $\left(\frac{a}{l}\right)^{\frac{1}{2}}$  represents the slight variation between glass (median or Palmqvist) and ceramic (Palmqvist).

The fundamental assumptions of Equation 2.12 are based on linear elastic fracture mechanics, in which the material behavior is brittle and limits interactions between induced fractures. Moreover, there is no ensuing lateral fracture, delamination, or shattering (Laugier, 1987). Fractures are initiated at the loading portion of the load-displacement curve (Cook and Pharr, 1990). The relation is valid for the ideal geometry wherein the induced fractures form a three-sided pattern emanating from the indented corner, as shown in Figure 2.9.

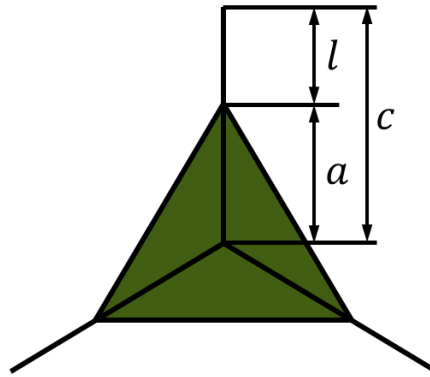


Figure 2.9—Schematic of a sample indented with a three-sided pyramid geometry tip, where the gray region represents the impression.

Fracture toughness is measured by the indentation method with a Vickers, Berkovich, or cube-corner tip. Berkovich and cube-corner tips are sharper and preferred over the Vickers tip because the size of radial fractures is best described on a sample surface (Dukino and Swain, 1992). A sharp indenter has been widely applied to define penetration depth and induce relatively simple fracture patterns rather than a blunt shape that most likely behaves in an elastic manner (Bell et al., 1991; Schiffmann, 2011). The fracture patterns generated on a sample surface are strongly related to the small contact loads with sharp indenters and the geomechanical behavior of materials. They govern elastic-plastic stress fields behavior for fracture development (Lawn and Howes, 1981).

#### 2.4.2. Energy method

The energy approach is an alternative method to calculate fracture toughness (Cheng et al., 2002). This method is applied to thin films and shale (Li et al., 1997; Liu, 2015). The following equations were developed as a quadratic function (Kick's law) to represent the loading and unloading curves without a holding step (Lawn and Howes, 1981) as

$$P = P_{max} \frac{h^2}{h_{max}^2}, loading \quad (2.13)$$

$$\text{and } P = P_{max} \frac{(h-h_f)^2}{(h-h_{max})^2}, unloading, \quad (2.14)$$

where  $P_{max}$  is the maximum applied load,  $h_f$  is the final displacement, and  $h_{max}$  is the maximum displacement at the end of a loading step. The total energy is expressed as

$$U_t = U_e + U_p = U_e + U_{pp} + U_{frac}, \quad (2.15)$$



where  $U_t$  is the total energy,  $U_e$  is the elastic energy,  $U_p$  is the plastic energy,  $U_{pp}$  is the pure plastic energy, and  $U_{fac}$  is the fracture energy.

Liu et al. (2016) proposed the method to employ elastic and pure plastic behavior. However, it does not represent real materials with complex microstructures. Pure plastic energy can be expressed as (Liu et al., 2016)

$$\frac{U_{pp}}{U_t} = 1 - \frac{1 - 3\left(\frac{h_f}{h_{max}}\right)^2 + 2\left(\frac{h_f}{h_{max}}\right)^3}{1 - \left(\frac{h_f}{h_{max}}\right)^2} \quad (2.16)$$

$$\text{and } h_f = h_r - h_{th} - h_{creep}, \quad (2.17)$$

where  $h_{th}$  is the thermal drift measured by the system, and  $h_{creep}$  is the creep displacement that occurred during a holding step at the maximum applied load. Jha et al. (2012) observed the load displacement in the power-law as

$$P = P_{max} \frac{h^n}{h_{max}^n} = Kh^n, \text{ loading} \quad (2.18)$$

$$\text{and } P = P_{max} \frac{(h-h_f)^m}{(h-h_{max})^m} = \alpha(h-h_f)^m, \text{ unloading.} \quad (2.19)$$

The total and elastic energies can also be determined by calculating the area under the loading curve with a holding step and the unloading curve expressed as

$$U_t = \int_0^{h_l} P dh + \int_{h_l}^{h_{max}} P dh = \frac{P_{max} h_l}{1+n} + P_{max} (h_{max} - h_l) = \frac{P_{max} h_{max} \left(1+n-\frac{h_l}{h_{max}}\right)}{1+n} \quad (2.20)$$

$$\text{and } U_e = \int_{h_r}^{h_{max}} P dh = \frac{P_{max} h_{max} \left(1-\frac{h_r}{h_{max}}\right)}{(1+m)}, \quad (2.21)$$

where  $n$  and  $m$  are the power indexes for the loading and unloading curves,  $h_l$  is the loading displacement at  $P_{max}$ , and  $h_r$  is the residual displacement. By acknowledging the previous parameters, the fracture energy,  $U_{frac}$  and can be calculated as

$$U_{frac} = U_p - U_{pp} \quad (2.22)$$

$$\text{and } h_c = h_{max} - \varepsilon \frac{P_{max}}{S}, \quad (2.23)$$

where  $h_c$  is the contact depth,  $\varepsilon$  is a constant related to the geometry of the indenter tip (0.75 for the Berkovich indenter tip). The critical energy dissipated during fracture per unit area of the created fracture-surface area or strain energy release rate is  $G_c$ , where the projected area,  $A_c$ , is determined as

$$A_c = 24.5h_c^2 \quad (2.24)$$

$$\text{and } G_c = \frac{\partial U_{frac}}{\partial A_{frac}} = \frac{U_{frac}}{A_c}. \quad (2.25)$$

The fracture toughness,  $K_c$  (Cheng et al., 2002), can be computed from the energy release rate multiplied by the reduced modulus,  $E_r$  as

$$K_c = \sqrt{G_c E_r}. \quad (2.26)$$

### 2.4.3. A comment on the application of the energy method for fracture toughness characterization based on nanoindentation

This investigation is related to the mechanical properties, mineral compositions, and microstructures of shale samples from the Bakken Formation. The fracture toughness of the shale was calculated using the energy-based method. The theoretical concept of this approach was proposed by Cheng et al. (2002), in which total energy ( $U_t$ ) is a sum of irreversible or plastic energy ( $U_p$ ) and elastic energy ( $U_e$ ). It corresponds to the load-displacement curve: the area under the loading and unloading curves determine  $U_t$  and  $U_e$ , respectively. As a result of nanoindentation, shale samples generate more complex than simple fracture patterns, making it difficult to measure their lengths. Therefore, many researchers prefer to use the energy approach rather than the crack length method to calculate fracture toughness on a small scale using nanoindentation. Three drawbacks of the energy-based method are as follows:

- i. The mathematical expression of pure plastic energy,  $U_{pp}$

By using the mathematical relationship,  $U_{pp}$  can be easily obtained by Equation 2.12 or Equation 11 in Liu et al., 2016. However, this expression assumes that the energy changes during loading-unloading are only costed by elastic and plastic deformations thoroughly (Lawn and Howes, 1981). Hence,  $U_p = U_{pp}$ . Some materials, such as cement paste and mortar, generated complex microfractures (Jha et al., 2012) and induced fracture energy,  $U_{frac}$ , where  $U_{frac} = U_p - U_{pp}$ .

$U_{pp}$  is a key parameter to calculate  $U_{frac}$ , which is used as an input parameter to calculate the energy release rate,  $G_c$  (Equation 2.24 or Equation 12 in Liu et al., 2016). Subsequently, it is possible to compute fracture toughness,  $K_c$  (Equation 2.26 or Equation 14 in Liu et al., 2016). It was observed that  $U_t$  and  $U_e$  obey the Meyer's power law function. By considering this, there were inconsistencies in the mathematical relationship while calculating  $\frac{U_{pp}}{U_t}$  because the denominator  $U_t$ , following Kick's law, was investigated, and the function does not consider microfractures

$$P = P_{max} \frac{h^2}{h_{max}^2}, \text{ loading} \quad (2.27)$$

$$\text{and } U_t = \int_0^{h_{max}} P dh = \int_0^{h_{max}} P_{max} \frac{h^2}{h_{max}^2} dh = P_{max} \frac{h^3}{h_{max}^2} \Big|_0^{h_{max}} = \frac{P_{max}}{3} \frac{h_{max}^3}{h_{max}^2} = \frac{P_{max} h_{max}}{3}. \quad (2.28)$$

## ii. Application of projected area, $A_c$

The projected area is one of the parameters used to estimate  $E_r$  and  $H$  (Fischer-Cripps, 2011), and it is related to penetration depth and the known geometry of the indenter. Here are some of the reasons why the proposed method and equation require correction or clarification for fracture toughness characterization:

- a. Assuming that the energy release rate may be written as stated above, apart from fracture energy definition, we also need to know the crack surface area created at this energy level. The proposed method assumes that crack surface area is related to maximum displacement and is a constant of 24.5. However, it is unclear how the equation has been derived and the physical evidence relating it to the crack surface area.

b. The equation for  $A_C$  is used to calculate reduced Young's modulus ( $E_r$ ) and hardness ( $H$ ) in Equation 2.24 and Equation 9 in Liu et al. (2016). The only difference is the magnitude of penetration depth ( $h_{max}$  versus  $h_c$ ), which indicates a huge difference that is not expected between the two.

iii. The correct order of magnitude

Some researchers have calculated fracture toughness based on the energy-based method using nanoindentation; the workflow can be seen in Liu (2015) and Liu et al. (2016). After comparison with the crack length method, both results have at least ten orders of magnitude difference. On the other hand, comparing the crack length method with standard mechanical testing, such as short-rod (Chandler et al., 2016), Brazilian tensile (Tran et al., 2014), three-point-bending (Jin et al., 2018), and straight notch Brazilian disc (Yuan et al., 2017), has proven that shale fracture toughness is in the same order of magnitude. Therefore, further investigation is required to develop a new expression of calculating fracture toughness based on the energy-based method.

## **CHAPTER 3. INDENTATION TECHNIQUE TO DETERMINE YOUNG'S MODULUS OF SHALE AT THE CORE SCALE USING DRILL CUTTINGS**

The content of this chapter has been published in *Petrophysics – The SPWLA Journal of Formation Evaluation and Reservoir Description* (Esatyana et al., 2020). This chapter proposes a new method to determine Young's modulus of shale at the core scale using drill cuttings. The average values of cuttings obtained from nanoindentation are compared with independent laboratory testing using core plugs.

### **3.1. Sample descriptions**

Seven core plugs were collected from the Wolfcamp Formation. The first three plugs are samples A, B, and C. The objective is to test the sensitivity of shale preparation at different stages based on Young's moduli results. The other four samples are labeled D, E, F, and G to define the spacing between indents on shale cuttings. The four plugs are then crushed to obtain cuttings and tested by nanoindentation to capture Young's moduli values. The results are compared with independent laboratory measurements on the core plugs.

### **3.2. Sample preparation**

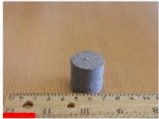
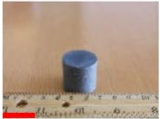
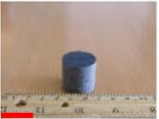
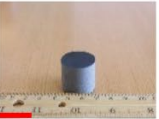
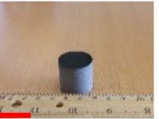
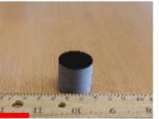
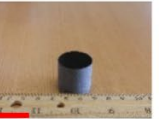







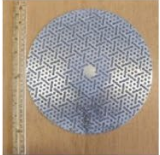
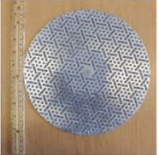

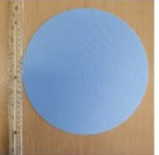


Standard rock mechanical testing has a large actuator that makes it less sensitive to local defects. Thus, core samples are easier to prepare before nanoindentation. Sample preparation is also easier for other fields, such as materials science and

mechanical engineering, because they focus on homogeneous materials, such as fused silica and aluminum, which usually have fewer defects than shale.

For the indentation testing, the tip that applies the load to the sample surface is smaller than the core size, which is in nanometers. The small tip size and penetration depth suggest that the sample surface must be properly prepared to obtain reliable results. Otherwise, the interpreted results may capture the surface roughness or any small fractures on the sample surface, which lower the resistance of the intact medium. The surface roughness is usually quantified in materials science and engineering, and the standards follow ISO 4287 (1997). However, the quantitative characterization of surface roughness is beyond the scope of this study.

Table 3.1 represents different stages of sample preparation on core plugs. The first three stages (stages 2 to 4) are grinding, and the last three (stages 5 to 7) are polishing (Bhushan and Gupta, 1991). Sample preparation begins with the grinding stage, which uses rough abrasive surface materials to remove imperfections like pits, nicks, lines, and scratches. Next, the polishing stage uses a finer abrasive to leave progressively thinner lines invisible to the naked eye. The sensitivity of sample preparation at each stage is discussed in the subsequent section.

Table 3.1—Shale surface with various discs for sample preparation at different stages. A nanoindenter tip is placed on the sample surface in the first stage for size comparison. The surface roughness decreases at higher stages and is more reflective of light.

Stage	1 (original)	2	3	4	5	6	7
Core plug	 25.4 mm	 25.4 mm	 25.4 mm	 25.4 mm	 25.4 mm	 25.4 mm	 25.4 mm
Enlarged surface	 25.4 mm	 25.4 mm	 25.4 mm	 25.4 mm	 25.4 mm	 25.4 mm	 25.4 mm
Discs used	—						
Disc description	—	Bonded diamond (Grit 500)	Bonded diamond (Grit 1200)	Composite for fine grinding	Woven acetate	Woven natural silk	Porous neoprene



### **3.3. Sensitivity of Young's moduli to sample preparation**

In the first step, the cross-section of the shale surface is divided equally (squares 1 to 16), and each square is indented at its center. The shale sample is initially indented at stage 1 (original). Then, it is prepared for the subsequent stages and tested until the sample surface at all stages is examined. The removed length of the shale sample perpendicular to the circular cross-section must be larger than the plastic zone size to avoid interference between indents.

The investigation of the average Young's moduli helps to better understand the effects of sample preparation at different stages, shown in Figure 3.1. The outcome is susceptible to the grinding stages because they remove local flaws, such as microfractures or defects, while the polishing stages slightly alter the results. Local flaws reduce the sample resistance against deformation. Hence, they can lower Young's modulus results captured from nanoindentation. For instance, after removal, the average Young's moduli in the first preparation stages increased to 83%, 52%, and 64% for samples A, B, and C, respectively. The average modulus changed to less than 10% during the last three stages for all the samples.

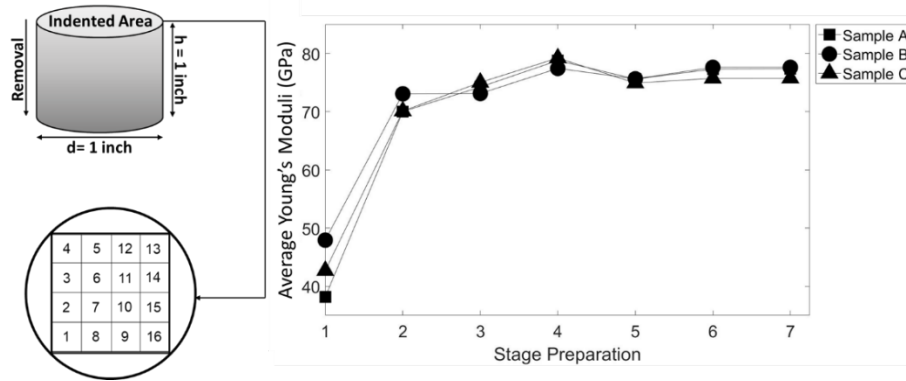


Figure 3.1—The shale cross-section is divided into equal areas and indented at the center (a). The average Young's modulus variation is obtained from the nanoindentation of the shale sample at each preparation stage (b).

### 3.4. Determining the cutting scale for nanoindentation

To interpret the elastic properties of the rock samples, it is assumed that Young's modulus of shale on a core scale is equal to the average value obtained from nanoindentation at a regular spacing if the value changes less than 20% while decreasing the distance between indents. This is based on the notion that the indent spacing must be larger than the plastic zone to avoid interference between the stimulated regions. The spacing distance is later implemented for cuttings.

In nanoindentation, Sneddon's solution is based on the stress field in an infinite half-space (Sneddon, 1965). This basis is usually applied to finite-size samples where the sample size is larger than the stimulated region. Sneddon's assumptions are often overlooked because researchers have focused on quantifying the local properties of porous media (Ulm et al., 2007; Shukla et al., 2013).

In this study, the assumption is compatible with the Sneddon solution, wherein nanoindentation captures a bulk property (as opposed to a local property) pertinent to a

volume smaller than the core volume. The justification is that a solid medium undergoes deformation in various locations, even at a small load. Johnson (1970) proposed a relation to calculate the corresponding plastic zone size (Figure 3.2), and it can be approximated as

$$\frac{c_p}{a_r} = \left[ \frac{1}{6(1-\nu_s)} \left( \frac{E_s}{\sigma_{yield}} \tan \left( \frac{\pi}{2} - \theta \right) + 4(1 - 2\nu_s) \right) \right]^{\frac{1}{3}}, \quad (3.1)$$

where  $c_p$  is the plastic zone radius,  $a_r$  is the contact radius,  $\nu_s$  is the Poisson's ratio of the sample,  $E_s$  is Young's modulus,  $\sigma_{yield}$  is the yield strength, and  $\theta$  is a geometrical parameter.

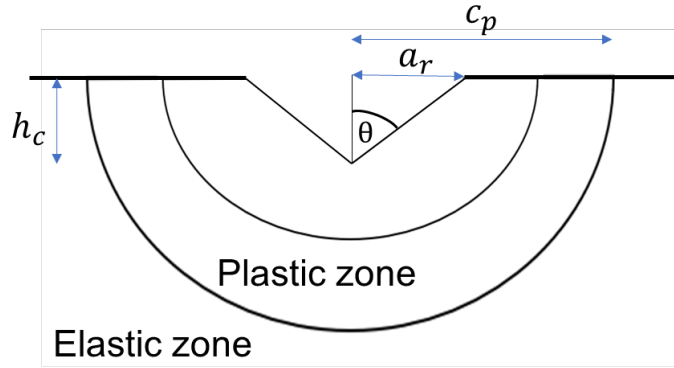


Figure 3.2—Schematic of the plastic zone. The minimum distance between indentations is larger than the plastic zone size (Chen and Bull, 2007) to avoid interference (spacing  $> 2c_p$ ).

The corresponding distance ( $c_p$ ) is equal to the representative elementary volume (REV) size (Hill, 1963), represented by the red square in Figure 3.3a, in which repetition creates the bulk volume at the large scale shown in Figure 3.3b. Thus, the assumption implies that there is a scale smaller than the core scale that controls the

core-scale properties. A smaller scale refers to a cutting scale, which is not essentially equal in different formations. In practice, it may be impossible to accurately determine the cutting scale for each formation because only small pieces are available. Nevertheless, estimating Young's moduli of a sample with a size close to the cutting size predicts their values at the core scale.

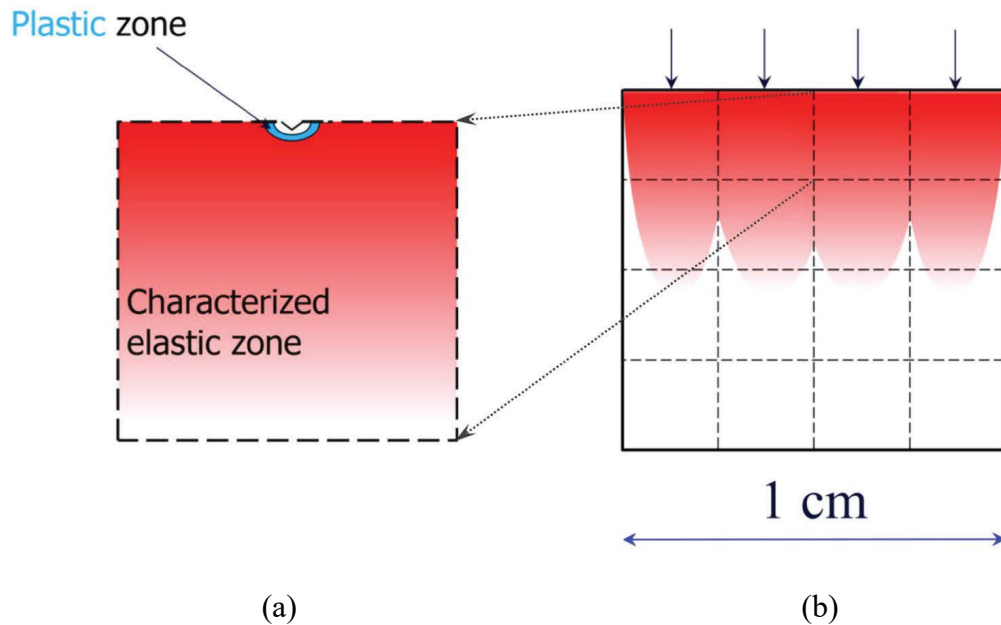


Figure 3.3—Conceptual illustration of the representative element volume (REV), in which repetition (a) generates the shale bulk volume (b).

The objective is to propose a method that can be applied to shale cuttings. The plastic zone size constrains the spacing between indents as the lower limit and the core size as the upper limit. The spacing must be larger than the plastic size to avoid interference between the stimulated regions. In the plastic zone, the sample is damaged significantly. Thus, the properties are unrealistic.

Next is the determination of the plastic zone size. In this study, the indentation load is 500 mN because the results are obtained with a smaller load ( $<100$  mN) and are influenced by surface roughness (Miller et al., 2008). Various shale samples show that the penetration depth is close to 3.5 microns for this load range. The semi-angle for the Berkovich tip is  $70.3^\circ$ , the Poisson's ratio is 0.25, Young's modulus is 20 GPa, and the yield strength is 20 MPa (Wang et al., 2001; Mavko et al., 2009; Zhu et al., 2009; Gao et al., 2015). The pertaining parameters lead to the plastic zone size ( $=2c_p$ ) equal to 85 microns (Equation 3.1). The variation of the plastic zone size corresponds with Young's moduli and yield strength when the Poisson's ratio is equal to 0.25, thus providing an estimate for the lower limit in different shale samples, as represented in Figure 3.4.

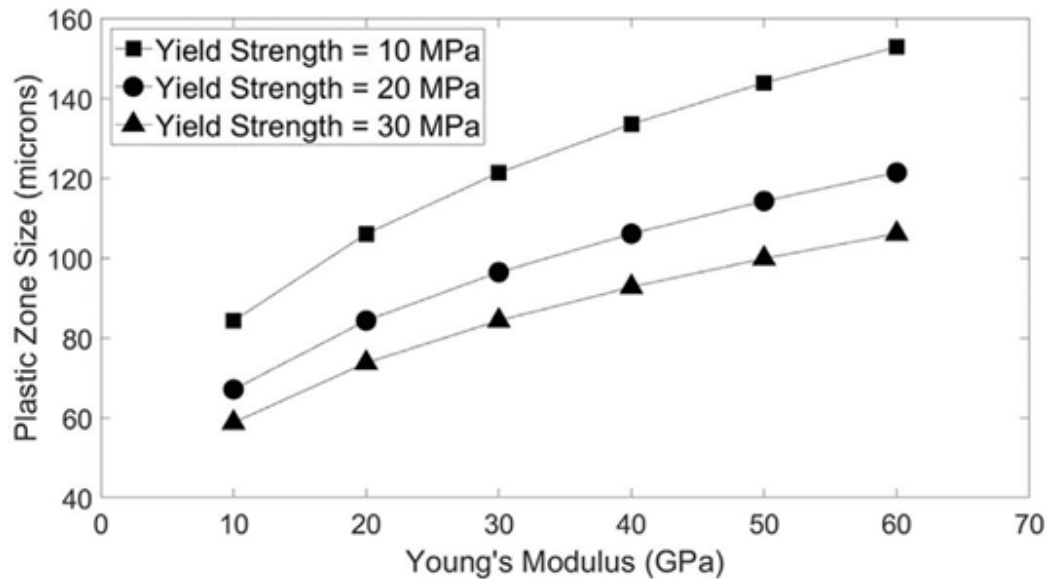


Figure 3.4—Variation of the plastic zone size with Young's modulus at different yield strength values. The Poisson's ratio equals 0.25, and Young's modulus and the yield strength values represent shale formations (Sayers, 2013; Sone and Zoback, 2013; Rybacki et al., 2015).

The plastic size estimation is based on the assumptions that Young's modulus and yield strength can change independently. In practice, the two are correlated, so the determined values present a limiting scenario. Nevertheless, the presented values are used only as a lower limit in this study, and they do not change the research findings.

At the initial stage, indentations with regular spacings are applied on the polished surface of a core plug to determine the cutting scale. Figure 3.5 represents the divisions and spatial locations of the indentations at each step. The spacing between indents is halved at each step. Other possible patterns can be attempted, which are likely to yield different outcomes. The objective is to determine the cutting scale and find the smallest size possible to be applied at the core size (~1 in.). The smallest size allows for small cuttings, which are more accessible.

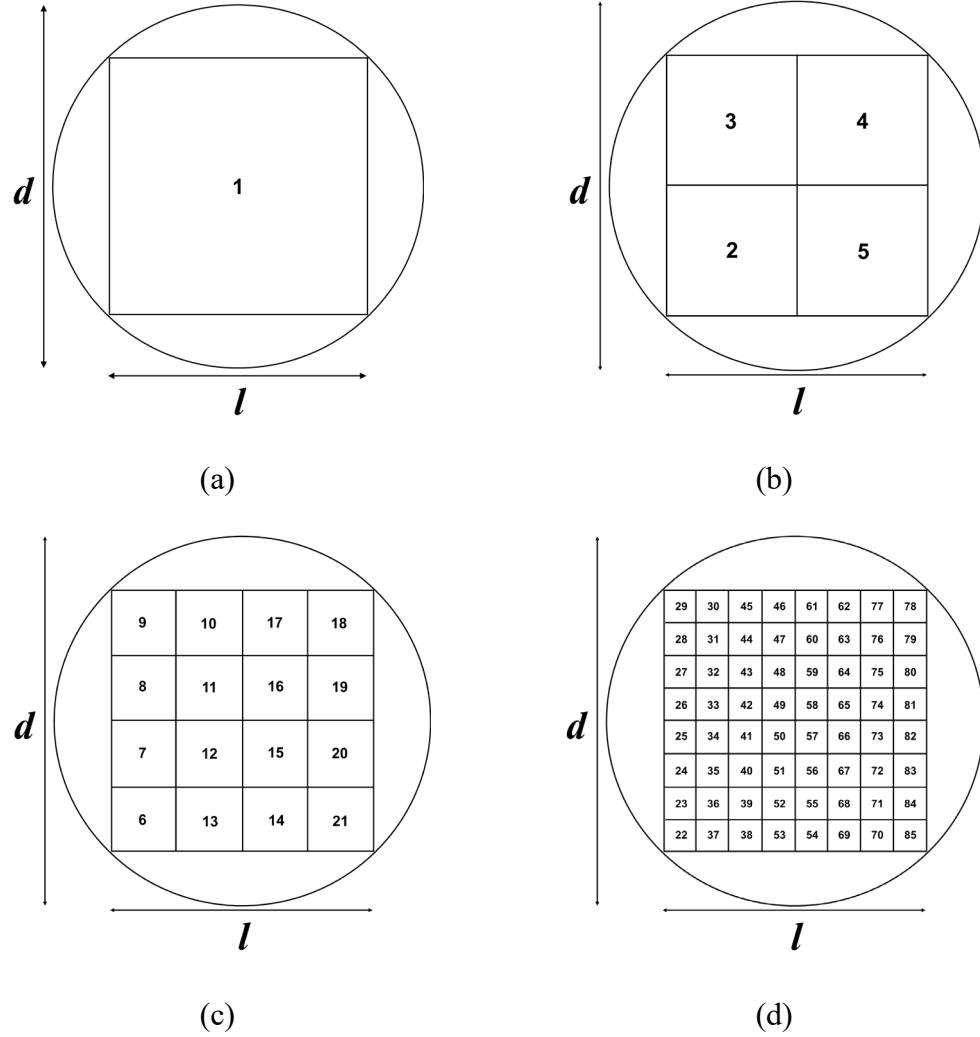


Figure 3.5—Spatial locations of nanoindentations in four steps on a core plug ( $d = 25.4$  mm,  $l = 17.6$  mm) with regular spacing. The area is equally divided in each step, and the process stops when the distance between the nearest indentations is close to the plastic zone size (a, b, c, d).

Nanoindentation investigates the shale surface regularly at various locations based on the pattern shown in Figure 3.5. The penetration depth is close to 3.5 microns when the applied load is 500 mN. Hence, the regular spacings of the loads are crucial for characterizing the shale surface. The result is related to the bulk properties and

depends on the penetration depth of each sample. Figure 3.6 represents the variation of Young's modulus of each sample.

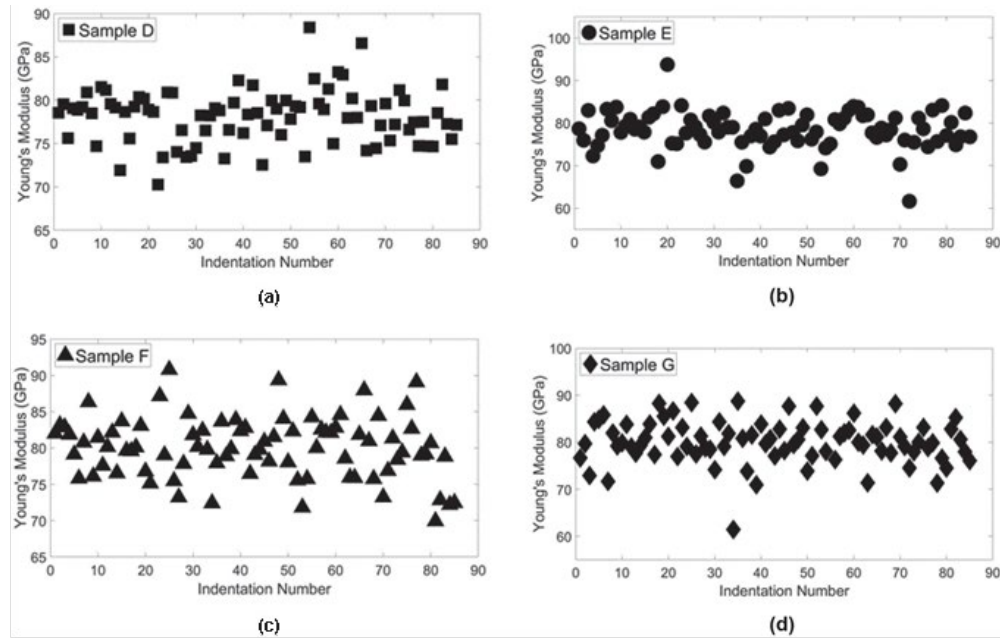


Figure 3.6—The variation of Young's modulus with the indentation number for samples D (a), E (b), F (c), and G (d). The spatial locations of the indentations are shown in Figure 3.5.

The primary parameters available from nanoindentations are Young's modulus and hardness (Equation 2.6). The main interest is to determine Young's modulus of the cutting scale. The average difference between Young's moduli at each step and those of the four nearest indentations evaluate the cutting scale. Figure 3.7 shows the average difference between Young's moduli is smaller than 6% when the regular spacing equals 2.2 mm and close to 4% when associated with 8.8 mm. The variations of Young's modulus obtained with 17.6-mm spacings are close to those of 8.8-mm spacings; thus, an 8.8-mm sample can replace a 17.6-mm sample. Following that, a 4.4-mm sample can be used for an 8.8-mm sample, and subsequently, a 2.2-mm can replace a 4.4-mm



sample. In conclusion, the cutting scale can be set close to 2.2 mm, and samples with this size or indentation spacing can be used for core scale measurements (**Hypothesis 1**).

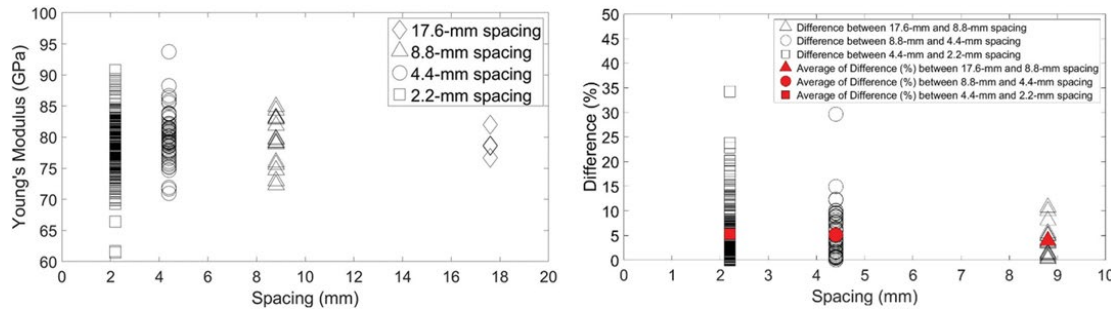


Figure 3.7—Young's moduli of shale samples resulting from nanoindentations with regular spacings (a) and the difference between Young's modulus at each step and the four nearest at the subsequent steps (b).

The cutting scale varies in different formations and even for different samples from the same formation. Shukla et al. (2013) proposed the typical size of cuttings as 3 to 5 mm. Cutting chips larger than 2 mm are ideal. In practice, some drill cuttings with around 1 mm also provide reliable results (Ortega and Aguilera, 2012). Another key consideration is that the cutting scale must be larger than the plastic zone size, close to 0.1 mm, where the applied load equals 500 mN. Therefore, the acceptable range for the cutting scale is a few millimeters. It is preferable to define a scale as small as possible to apply on cuttings.

Figure 3.8 represents the cuttings before (a) and after (b) sample preparation. A scale ruler shows the sample size. The data reported in the literature (Ortega and Aguilera, 2014) is consistent with various sample sizes in this study. The small polished pieces were well-positioned and attached to the aluminum puck with minimal glue

instead of resin, as other researchers (Deirieh et al., 2012; Shukla et al., 2013) did to avoid any form of substrate softer than the materials. Loads were applied perpendicular to the sample to maintain alignment between the indenter tip and aluminum puck.

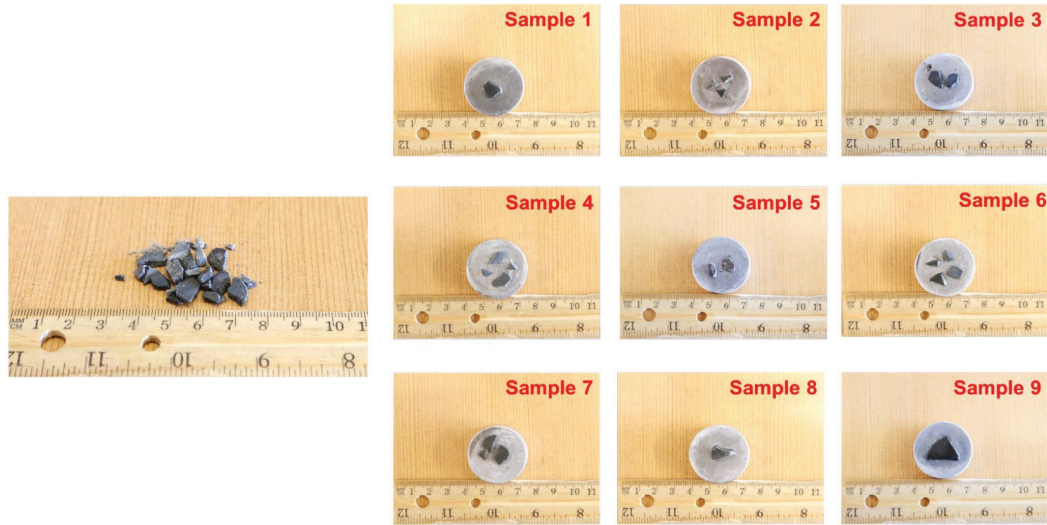


Figure 3.8—Small pieces or cuttings of shale are used to test the accuracy of the cutting scale (a), and prepared samples are glued to an aluminum puck for nanoindentation (b).

In this study, the accuracy of the cutting scale was tested to determine Young's moduli at the core scale. The independent laboratory measurements were first conducted on core plugs under different confining stresses (40.6, 50.6, and 30.5 MPa). Then, the small pieces obtained from compression during triaxial testing were used for nanoindentation. Indentation spacings of 2.2 mm were applied to small pieces. Figure 3.9 shows the results. The difference between the average Young's modulus based on nanoindentation and the independent laboratory measurement was calculated to test the proposed method. The results remained smaller than 30% for all shale samples.

Therefore, the agreement between the predicted values of nanoindentation and independent testing verifies the first hypothesis (**Test 1**).

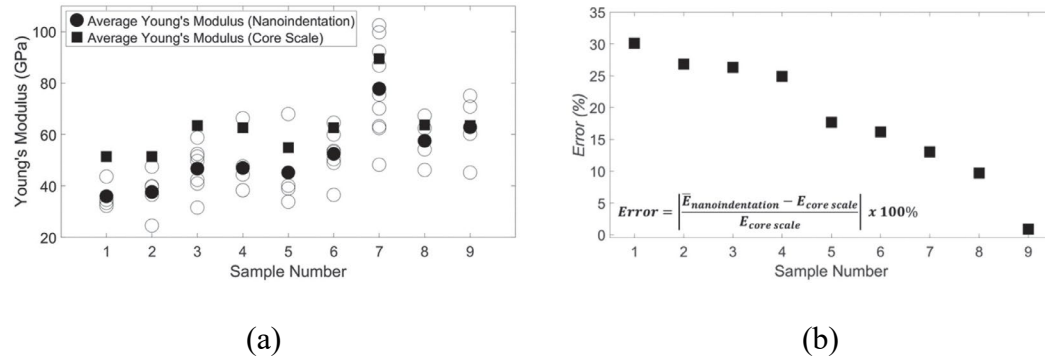


Figure 3.9—Young's moduli of shale samples obtained from independent triaxial tests using core plugs and nanoindentation using small pieces or cuttings (a) and the decrease in error when samples reached a higher level of smoothness after preparation (b).

Using a microscope, the difference between unpolished and polished surfaces becomes apparent in Figure 3.10. The finished surface of a core plug reaches a higher level of smoothness than cuttings. Achieving a high-quality surface that reflects light (Table 3.1) is challenging when dealing with cuttings. This is because of a high level of irregularity in the initial state of cuttings. Moreover, polishing small pieces of brittle materials is more difficult.

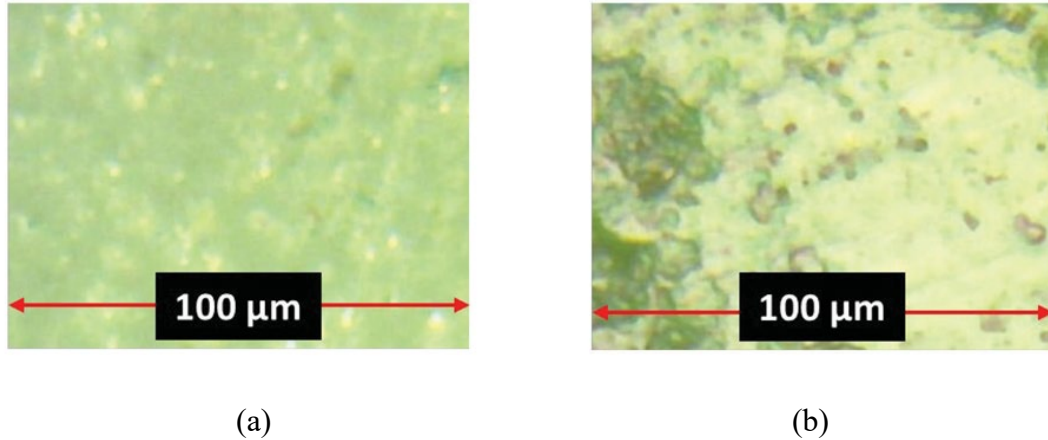


Figure 3.10—The polished surface of the core plug, which corresponds to stage 7 in Table 3.1, reaches a higher level of smoothness (a) than cuttings in Figure 3.10b (b). Cuttings with the smoothest surface are less influenced by local flaws and are close to the core scale measurements.

The methodology and correlation of using drill cuttings have proven useful for providing direct sources to quantitatively evaluate rock properties, such as porosity, permeability, and Young's moduli (Lopez et al., 2015). This is important because the availability of well logs and core data remains limited compared with cuttings. However, it is desirable to collect both drill cuttings and core plug data for comparison to determine the correction factor associated with these two direct sources of information (Ortega and Aguilera, 2014). Once the data obtained from drill cuttings are corrected to cores, the proposed correlations can be applied as reasonable approximations to estimate Young's moduli for use in other shale formations.

### **3.5. Discussion**

The main objective of this study was to propose a method that would be applicable for shale cuttings to predict Young's moduli at the core scale. However, there are limitations to the application of nanoindentation on cuttings and sample preparation. The standard method for preparing the shale surface is usually best for large samples. Small pieces like cuttings typically have irregular shapes and break during polishing, especially when the sample is brittle.

The results presented in Figure 3.8 are based on the application of regular spacings rather than finding the smoothest area to make the process more systematic. There was an improvement in the results when the smoothest area was selected for indentation; thus, the error was smaller. Based on the analysis, improving the quality of sample preparation reduces errors. The ion-milling technique is better suited to smaller samples and expected to improve the accuracy of the results.

For various reasons, analyzing cuttings for formation characterization is appealing. Cuttings help better in characterizing the formation heterogeneity along the wellbore when only small pieces are available. In contrast to large samples, cuttings are abundant and can easily be recovered at a minimal cost. They can be used in close real-time conditions. Thus, the actual interpretation of the properties is significant, especially if the cuttings collected on the surface can be associated with the formation depth. In this study, the sample depth was not discussed.

Predicting Young's moduli on a core scale from nanoindentation provides additional information that can be beneficial for developing more realistic reservoir models. The model involves anisotropic behavior that exhibits different properties as a function of spatial orientation. However, it is impossible to determine the bedding direction on cuttings, which becomes more complex when the sample is smaller. Therefore, the reported Young's modulus for each sample at the core scale may be interpreted as an effective isotropic response. The determination of anisotropic properties based on nanoindentation entails loading in different directions. More advanced preparation techniques are required to reach a high level of smoothness (stage 4 in Table 3.1) on the shale surface.

The shape of the cutting is irregular, leading to an uneven thickness. The thickness of the cuttings in this study is a few millimeters, although it is measured in this study. The cutting is larger than the plastic size.

The proposed method predicts Young's moduli of shale on a core scale from drill cuttings using nanoindentation in a systematic pattern. The assumption was that the average Young's modulus obtained from nanoindentation characterizes the sample behavior on a core scale when the average property does not change with decreasing distance. As a validation, the nanoindentation results were compared with independent laboratory testing. Thus, no upscaling is required to determine the core scale properties.

### **3.6. Conclusions**

The main objective of this study was to propose a new method that can be used to characterize shale formations using drill cuttings. The proposed method is required because large samples (~1 in.) are often unavailable. Thus, cuttings are the only sources available and used to determine Young's modulus on a core scale. The Young's moduli of shale cuttings were obtained from nanoindentation. Then, the values were averaged to predict Young's modulus on a core scale. The error of predicted results yielded a good agreement where the value was smaller than 30% for all the samples on a core scale.

This study also showed that surface smoothness has a major impact on the results obtained from nanoindentation. Smoothness was achieved by sample preparation prior to indentation testing. Surface grinding and then polishing stages were performed. The two processes are desirable to remove local defects on the shale surface and attain properties more representative of bulk behavior. Surface grinding is more crucial than the polishing stage, which can be omitted. The average Young's moduli resulting from nanoindentation increased more than 50% after grinding but less than 10% after polishing.

Nanoindentation and its governing equations, including sample preparation, were discussed. The technique is an appealing approach for small pieces. However, it is prone to sample preparation because the size of the indenter tip is in the range of nanometers. This study revealed that the predicted results from cuttings are close to core scale measurements when the sample is prepared properly. In the petroleum industry,

cuttings analysis characterizes the formation heterogeneity along the wellbore, specifically in horizontal drilling, where large samples are not easily recovered.



## **CHAPTER 4. CHARACTERIZING ANISOTROPIC FRACTURE TOUGHNESS OF SHALE USING NANOINDENTATION**

The content of this chapter has been published in the *SPE Reservoir Evaluation & Engineering* (Esatyana et al., 2021). This chapter proposes a conceptual model to characterize the fracture toughness of shale using nanoindentation. The predicted fracture toughness values obtained from the Berkovich tip are compared with the cube-corner tip to partially validate the proposed model.

### **4.1. Sample descriptions**

The Wolfcamp Formation has been an active unconventional resource located in the Permian Basin in Texas. Four shale samples in two different directions were retrieved; two samples (Samples 1 and 2) are parallel to the bedding planes, and two (Samples 3 and 4) are perpendicular to the bedding planes. In this study, the Berkovich tip indents each sample. The estimated fracture toughness results are validated using the cube-corner tip at the same scale based on the conceptual model proposed in this study.

### **4.2. Complexities of fracture toughness characterization in shale**

One of the main parameters in calculating fracture toughness is the fracture length. Determining the fracture length from nanoindentation on shale is challenging because the induced patterns differ from those identified in the literature (Figure 2.3). Fracture length is inversely proportional to fracture toughness. Laugier (1987) proposed

an analytical approach to show the dependency of fracture toughness on the fracture length as

$$K_c = \alpha \left(\frac{a}{l}\right)^{\frac{1}{2}} \left(\frac{E_s}{H}\right)^{\frac{2}{3}} \frac{P_{max}}{c^{\frac{3}{2}}}, \quad (4.1)$$

where  $a$  is the distance from the indented center to the corner,  $l$  is the distance from the indented corner to the fracture tip,  $E_s$  is Young's modulus of the sample,  $P_{max}$  is the maximum applied load, and  $c$  is the measured fracture length. The term of  $\left(\frac{a}{l}\right)^{\frac{1}{2}}$  demonstrates slight variation between glasses (median or Palmqvist) and ceramics (Palmqvist).

Figure 4.1 shows indented shale samples at 300 mN, 500 mN, and 700 mN. The dark triangle near the center denotes the indented area or impression; the light green, which covers most of the area, is the polished surface. The light grey irregular shapes surrounding the indented area are relevant to defects caused by the lack of sample preparation. The shale heterogeneity is clear from the high-resolution images (photographs) captured from the shale surface after the indentation process.

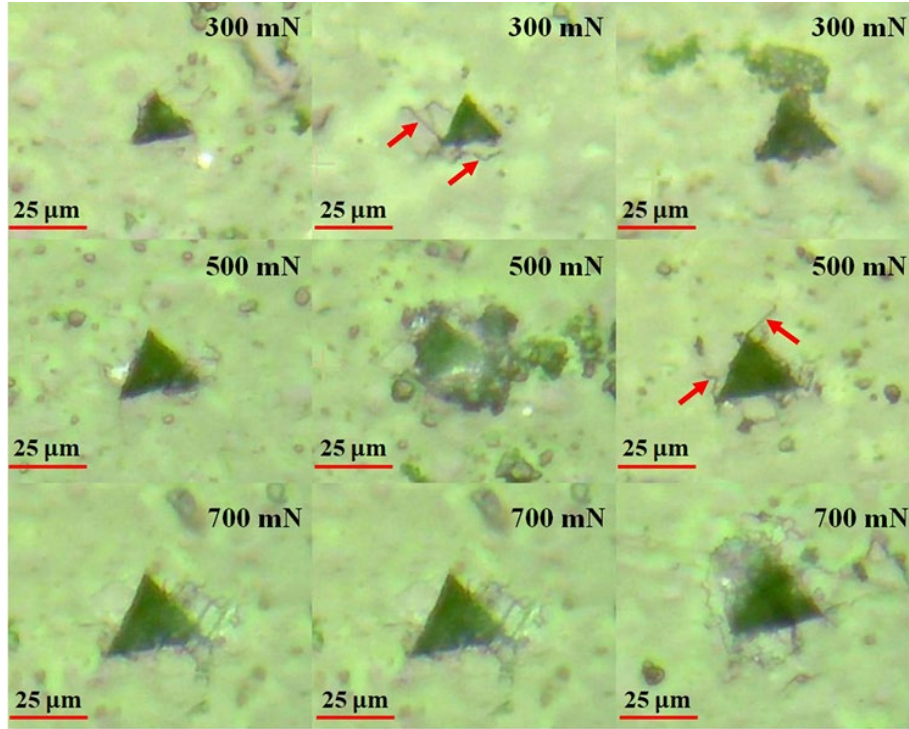


Figure 4.1—High-resolution images of shale indented by 300, 500, and 700 mN. The induced fractures are distinct even at the same load, indicating a high heterogeneity level. The red arrows point out the relatively simple patterns used for fracture toughness characterization in this study.

### 4.3. Approach

#### 4.3.1. Conceptual model

The shale matrix is assumed to consist of two intertwined, solid domains. When the maximum load is applied, one domain remains intact, whereas the other domain is weaker and fails when loaded, resulting in fractures. The boundary between the grains generates the weaker domain. Fracture toughness measurement only accounts for the failure of the weaker domain. Fractures only generate when the tip hits the weaker domain to characterize the pertinent shale properties using nanoindentation. The high-

resolution images show that simple fracture patterns are acceptable to determine fracture toughness with the condition that their lengths are smaller than 20 microns. On the other hand, fracture toughness is difficult to measure in a complex pattern when its length is greater than 25 microns. Thus, indentations within complex patterns and without fractures are excluded from fracture toughness characterization (**Hypothesis 2**).

The proposed conceptual model is realistic for shale to better capture its heterogeneity. It is challenging to depict the shape and size of the mineral properties that correspond to the stronger domain because of their distinctive components. Figure 4.2 represents the schematic of the conceptual model. The Voronoi cells (Voronoi, 1908) with different colors illustrate the stronger domain, and the boundaries represent the weaker domain. The Voronoi cells can have different properties and remain intact during nanoindentation. However, the properties of the weaker domain are of interest in this study.

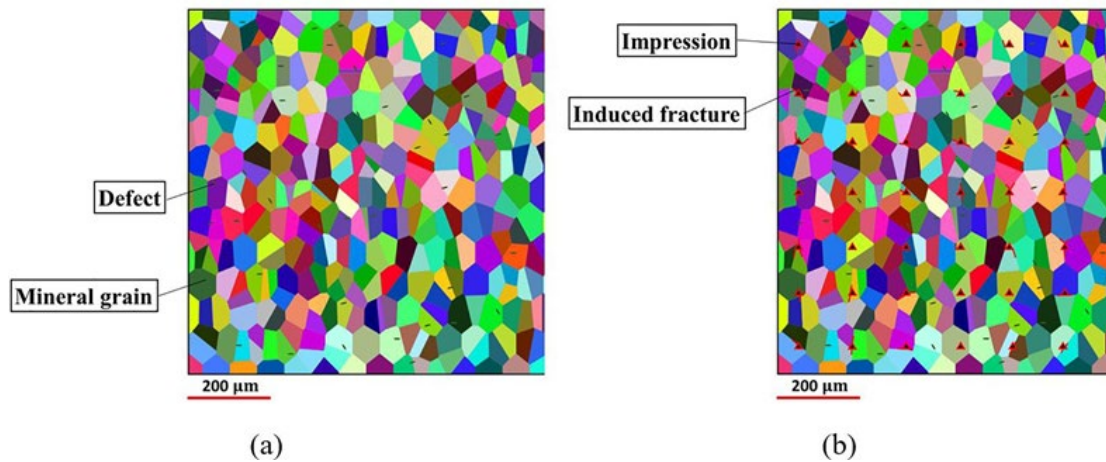


Figure 4.2—Schematic of the proposed conceptual model based on the Voronoi cells in shale. Various colors represent the stronger domain while the boundaries between them constitute the weaker domain (a). The loads

applied to the indenter tip induce fractures when the tip hits the weaker domain (b).

Nanoindentation creates different scenarios when it hits the surface. For instance, a fracture occurs when the tip contacts the weaker domain, which will be the only domain analyzed to calculate the fracture toughness. On the other hand, when the indenter tip lands on the grain, which is part of the stronger domain, it generates no fracture. Hence, nanoindentation without fractures is omitted. Maxwell (1873) proposed a similar model for the first time, known as the effective-medium theory for characterizing properties of porous media, which can be adopted for analyzing fracture toughness.

#### **4.3.2. Maximum applied load in nanoindentation**

Nanoindentation creates a local impression but does not necessarily break the sample. There is no direct way to assign the acceptable load *a priori* to determine fracture toughness because the dimensions of locally induced fractures vary. As a result, various loads at different locations are applied to determine the acceptable range where linear elastic fracture mechanics assumptions are realistic.

The spacing between adjacent indents is larger than the plastic zone size to avoid interference and attain realistic mechanical properties (Esatyana et al., 2020). The sample is damaged significantly in the plastic zone. If only two indents are conducted with an identical load, the spacing can be as large as the sample diameter.

Figure 4.3 shows that the indentation location patterns follow the hybrid grid system with relatively random grain boundaries. This procedure ensures that the effects

of the sample heterogeneity are included. The hybrid grid system explores an extensive area with various loads to account for heterogeneity, thus better characterizing the sample. The load increases from 50 to 1,100 mN with increments of 50 mN. This study uses square grids, although other patterns are possible. The acceptable range for generating a relatively simple fracture pattern is identified by trial and error.

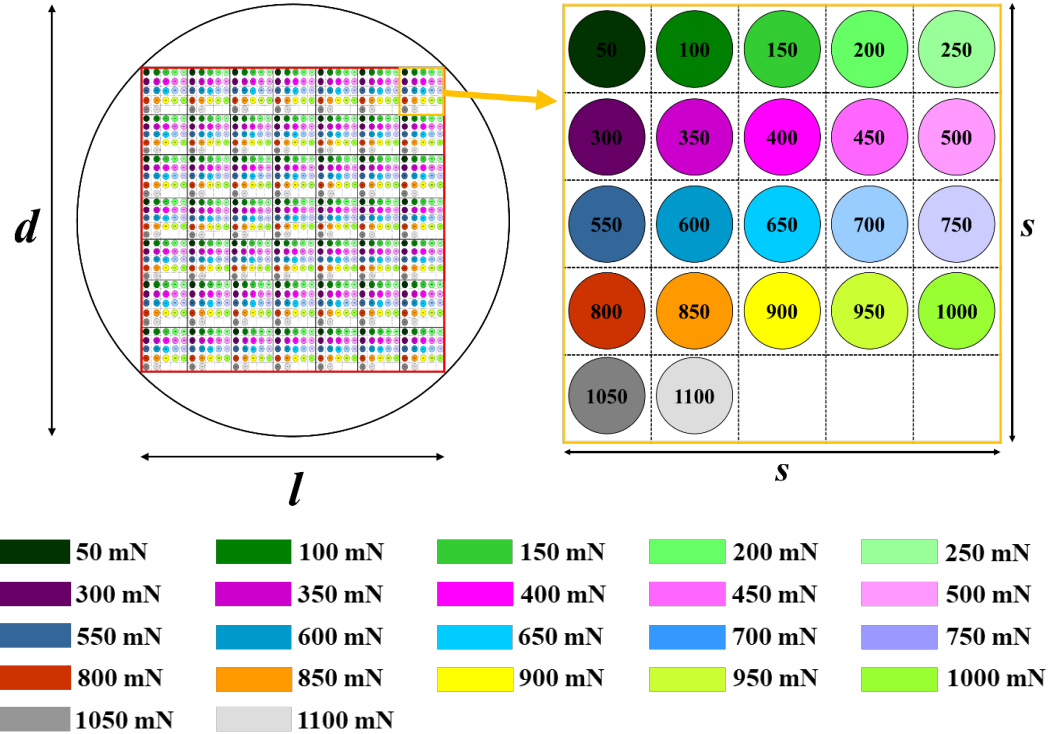


Figure 4.3—The hybrid grid system used in this study. The core plug diameter,  $d$ , is 25.4 mm. The major grid size,  $m$ , and minor,  $s$ , are 17.1 and 2.44 mm, respectively.

#### 4.3.3. Damaged versus fractured regions

The ideal fracture pattern propagates from a three-sided Berkovich tip, which is present in homogeneous media, such as fused silica. Figure 2.9 illustrates an example of such a pattern. However, the ideal pattern does not form in shale because of the high

level of heterogeneity. Other researchers have also reported the absence of the ideal pattern in shale (Gupta et al., 2020; Shukla et al., 2013). Figure 4.4 represents high-resolution images that clearly demonstrate the complexity of fracture patterns on the shale surface, where the maximum applied load is 500 mN. Three types of fracture patterns are classified: no fracture, simple fracture, and complex fracture.

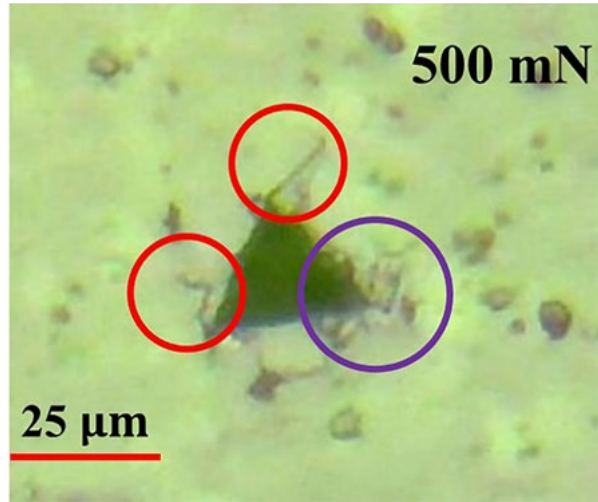


Figure 4.4—High-resolution images of shale surface resulting from the Berkovich tip. The red circles represent two relatively simple fracture patterns, and the purple circle indicates a complex pattern.

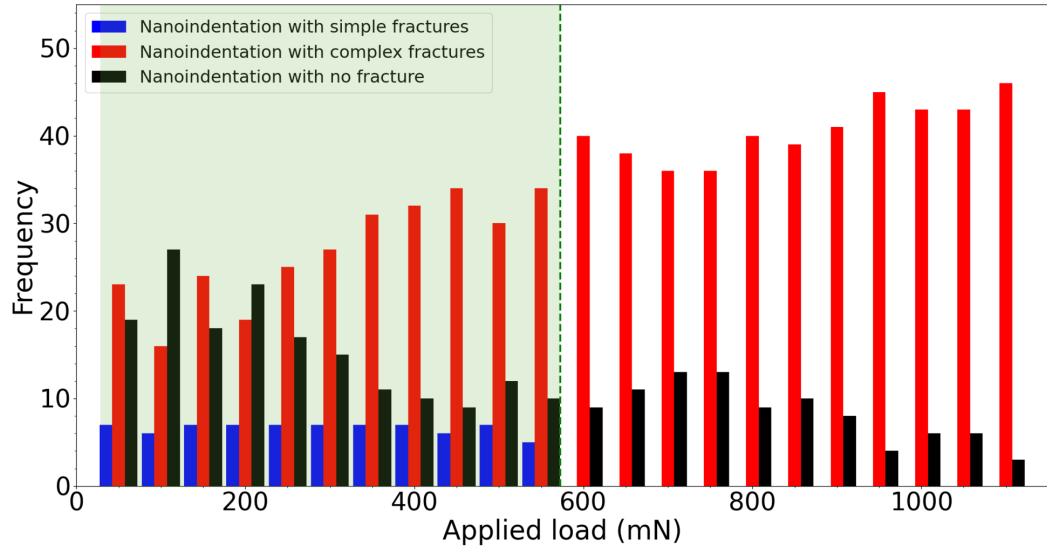
A simple fracture pattern is created when the fracture length is smaller than 20 microns. If it is a complex pattern or damaged area, which is difficult to measure, the length is greater than or equal to 25 microns. The applied loads are classified as *acceptable* when a relatively simple fracture pattern (red circle) is generated or *excessive* when the fracture pattern is complex (purple circle). The fracture length in the simple fracture pattern is preferable in determining fracture toughness. This classification is because the analytical relation for fracture toughness characterization is valid when the

fundamental assumptions of linear elastic fracture mechanics (LEFM) are realistic. LEFM corresponds to the conditions that do not intersect between the induced fractures, and the plastic zone size is small.

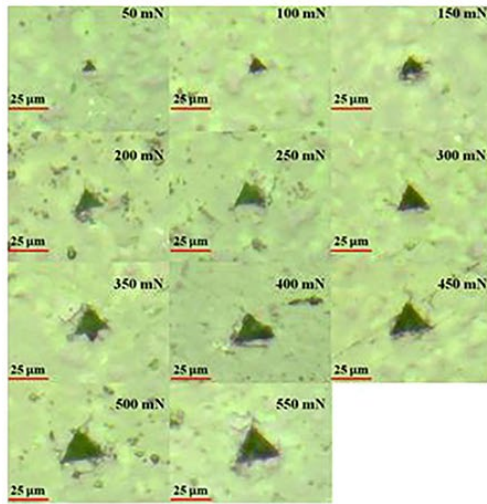
I used a cube-corner tip to partially validate the proposed approach at the same scale. The two tips have different topologies. The difference is that the contact angle is smaller in the cube-corner tip, which forms fractures more easily compared to the Berkovich tip for a given load. A similar procedure was followed to apply the load using the hybrid grid system and identify the fracture length. The fracture toughness values calculated by the cube-corner tip were subsequently compared to those of the Berkovich tip.

The high-resolution images in Figure 4.5 are parallel to the bedding planes and analyzed to classify the load range. Based on the histogram, it is suggested that the applied load is acceptable for fracture toughness characterization when the load is smaller than or equal to 550 mN, with a damaged zone size close to 9 microns. In contrast, the applied load is deemed excessive when greater than 550 mN (green dashed line in Figure 4.5a). The acceptable load range may not be identical in different directions because of anisotropic behavior. Figure 4.6 indicates that relatively simple fracture patterns form more easily in samples perpendicular to the bedding planes because they propagate away from the indenter tip without creating any significant damage when the size is greater than or equal to 25 microns.

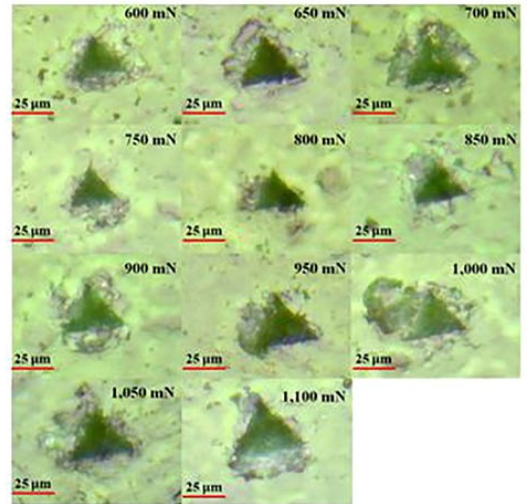




(a)

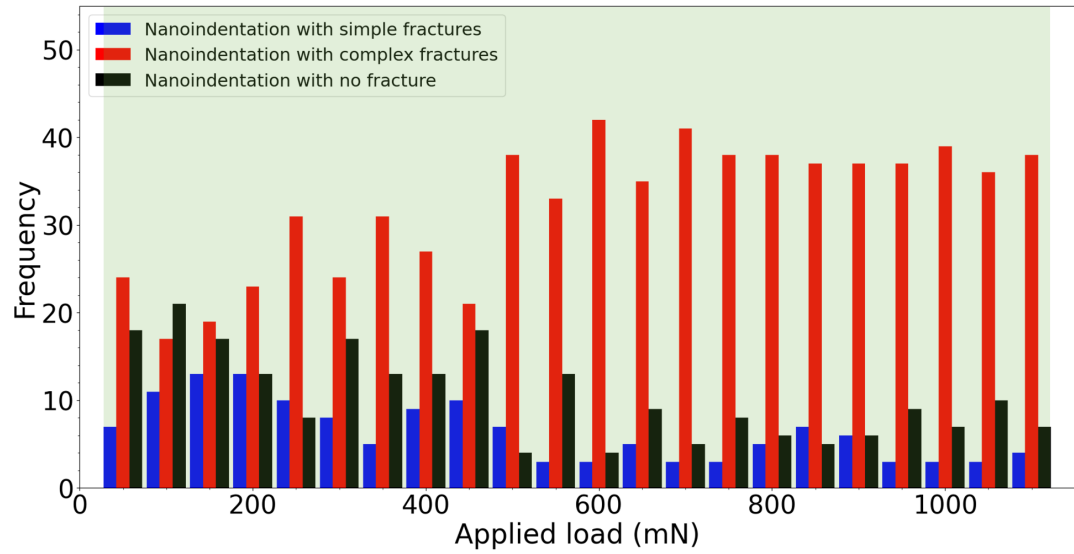


(b)

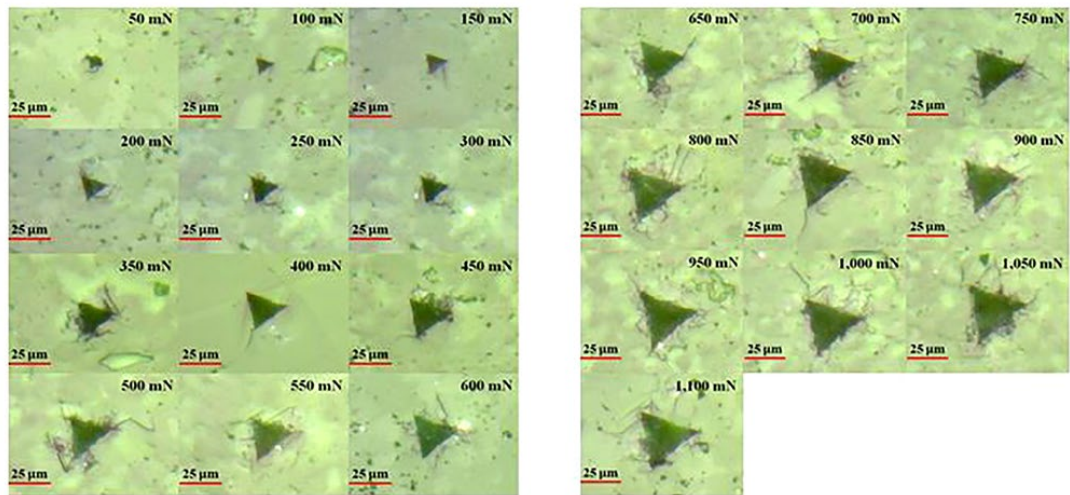


(c)

Figure 4.5—Histogram of a shale sample for simple and complex fracture patterns parallel to the bedding planes with various loads (a). High-resolution images where the applied load is *acceptable* for fracture toughness characterization when smaller than or equal to 550 mN (b) and *excessive* when larger than 550 mN (c).



(a)



(b)

Figure 4.6—Histogram of a shale sample for simple and complex fracture patterns perpendicular to the bedding planes with various loads (a). High-resolution images where all the applied loads are acceptable for fracture toughness characterization (b) because the induced fractures are relatively simple.

The induced fractures in Figures 4.5 and 4.6 are distinct. The applied loads cause more damage in the sample parallel to the bedding planes and lead to acceptable fractures in the sample perpendicular to the bedding planes. The difference represents a change in the acceptable load range, which may be relevant to the bedding planes' direction (Gu, 2018)—specifically, it affects the sample response at a small scale. Determining the threshold value may appear subjective; high-resolution images provide a guideline to define an acceptable load range. The damaged area is typically close to the impression without a discernible fracture when the load is excessive.

#### **4.4. Results**

The fracture toughness is determined by calculating the fracture length from high-resolution images. These results are averaged to make them more representative. The following examples are provided for clarification to distinguish the fracture patterns. Figure 4.7 represents high-resolution images with fractures whose patterns are considered relatively simple in this study. The assigned lengths ( $a_1$ ,  $a_2$ ,  $l_1$ ,  $l_2$ ) make it possible to determine the corresponding fracture length to dictate the fracture toughness, listed in Table 4.1.

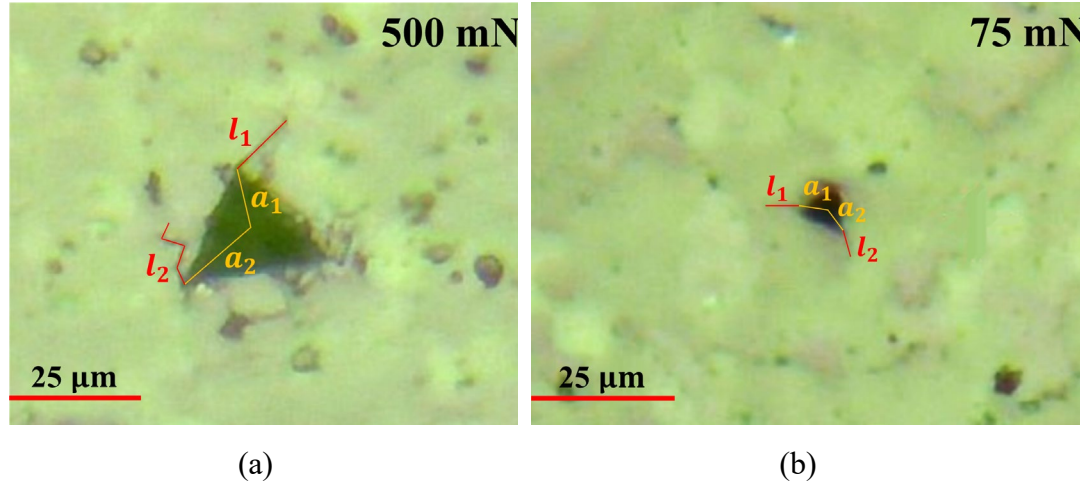


Figure 4.7— The indentation impression on a shale surface of a Berkovich tip parallel to the bedding plane (a) and a cube-corner tip perpendicular to the bedding plane (b).

Table 4.1— The relevant parameters to calculate fracture toughness (last row) of shale samples using a Berkovich tip in a parallel sample (Figure 4.7a) and a cube-corner tip in a perpendicular sample (Figure 4.7b).

Description, unit	Parameters	Sample direction	
		Parallel	Perpendicular
1 <sup>st</sup> distance from the center to the corner, microns	$a_1$	18.09	5.00
2 <sup>nd</sup> distance from the center to the corner, microns	$a_2$	18.09	5.00
1 <sup>st</sup> distance from the corner to the tip, microns	$l_1$	14.14	7.50
2 <sup>nd</sup> distance from the corner to the tip, microns	$l_2$	15.81	10.31
Average distance from the center to the corner, microns	$a_{average}$	18.09	5.00
Average distance from the corner to the tip, microns	$l_{average}$	14.98	8.905
Fracture length, microns	$c$	33.07	13.91
Empirical coefficient, dimensionless	$\alpha$	0.016	0.032
Young's modulus, GPa	$E_s$	77.39	85.3
Hardness, GPa	$H$	2.11	2.35
Maximum applied load, mN	$P_{max}$	500	75
Fracture toughness, MPa.m <sup>1/2</sup>	$K_c$	0.498	0.383

The conversion of the acquired data of load (mN) and displacement (nm) to Young's modulus ( $E_s$ ) and hardness ( $H$ ) of the sample is a function of the maximum applied load and the projected area. The nanoindenter instrument usually follows a standard procedure (Oliver and Pharr, 1992). Only a few indentations lead to a simple fracture pattern, approximately 3 to 13 out of 49 tests. Figure 4.8 shows the corresponding ratio of simple and complex fracture patterns using the Berkovich tip.

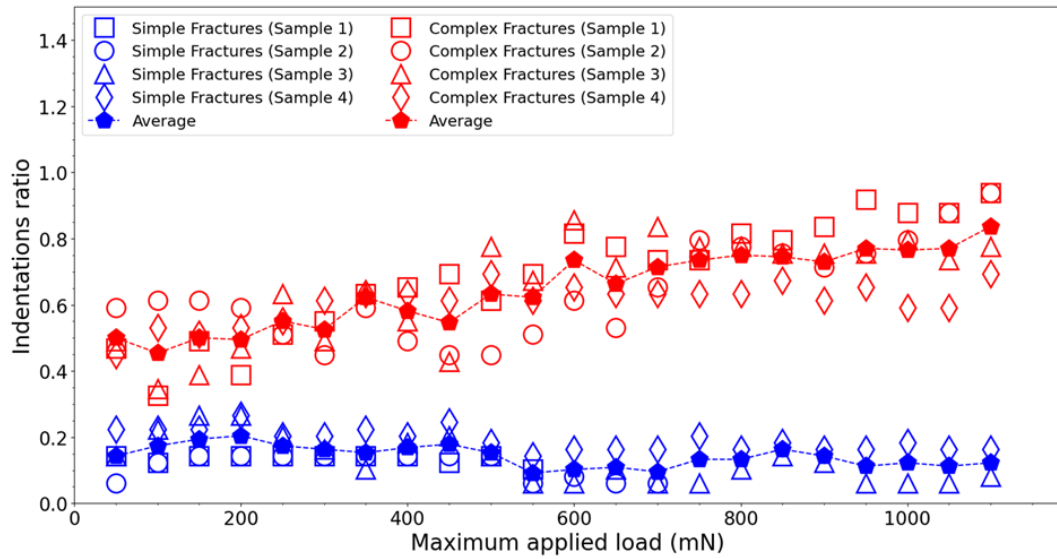


Figure 4.8—The variation of the ratios of the indentation tests with simple and complex fractures to the total number of tests, which is equal to 49, at each load. Complex induced fractures occur when the applied load is greater than 550 mN for Sample 1 and 700 mN for Sample 2. However, some loads do not create any fractures.

The indentation tests followed the hybrid grid system in Figure 4.3 using the Berkovich tip. Fracture creation usually depends on the sample's heterogeneity and anisotropy. Simple fractures propagate more easily within a layer (perpendicular) than across several bedding planes (parallel). Based on the proposed conceptual model, the interpreted fracture toughness of shale samples at various loads using Berkovich and cube-corner tips are represented in Figure 4.9 and Figure 4.10, respectively.

Figure 4.9 depicts that the average fracture toughness is  $0.65 \text{ MPa.m}^{1/2}$  and  $0.72 \text{ MPa.m}^{1/2}$  for Samples 1 and 2, respectively; and  $0.48 \text{ MPa.m}^{1/2}$  and  $0.51 \text{ MPa.m}^{1/2}$  for Samples 3 and 4, respectively. Samples 1 and 2 are parallel to the bedding planes, whereas Samples 3 and 4 are perpendicular. The Berkovich tip indented samples at various loads. The lower fracture toughness in perpendicular samples (Figure 4.6b) is consistent with the high-resolution images where fracture propagates more easily than in parallel samples (Figure 4.5b).

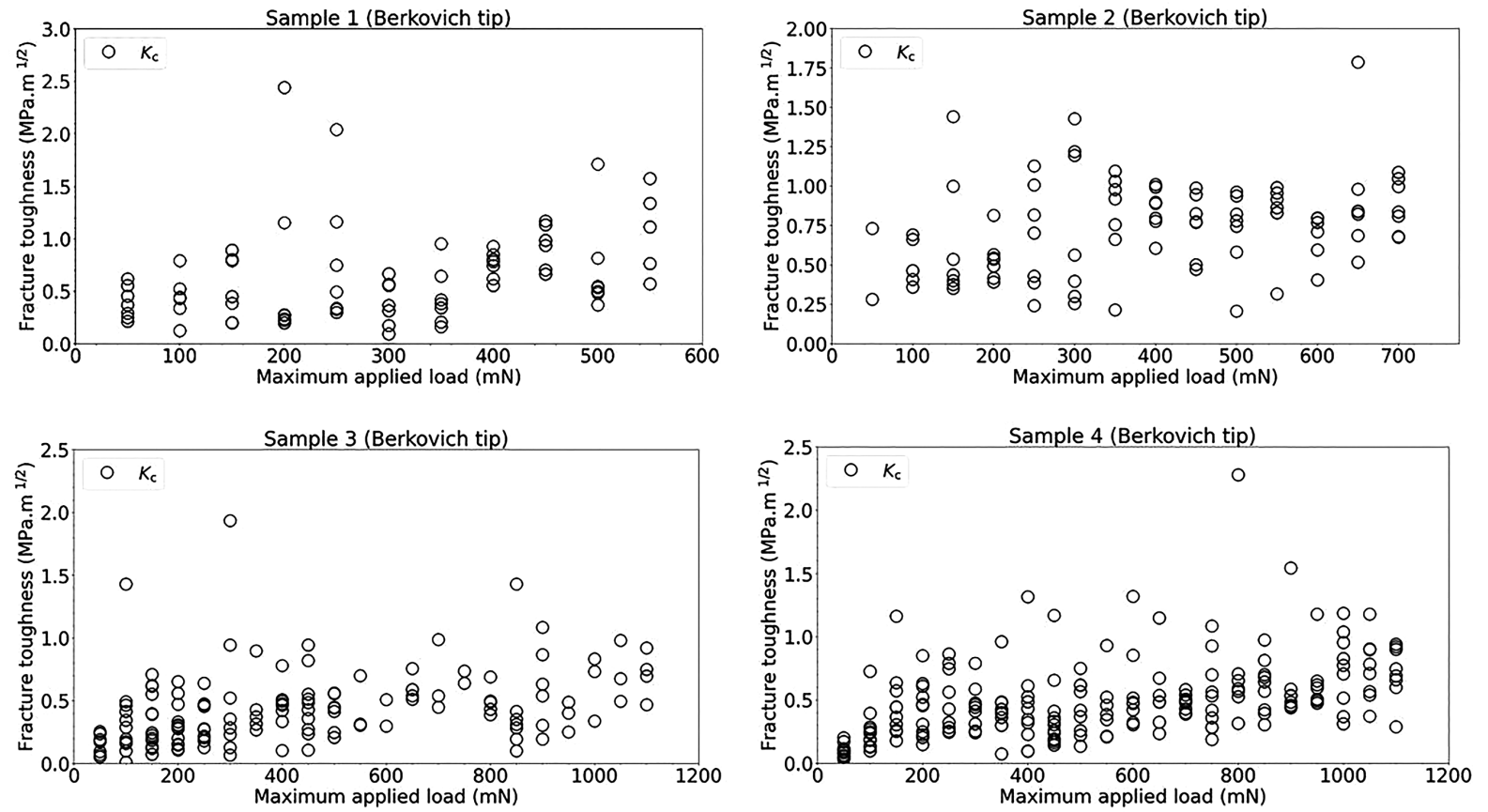


Figure 4.9—The fracture toughness values of four shale samples tested by the Berkovich tip.

Next, the cube-corner tip determines the fracture toughness values of shale samples. The comparison partially validates the fracture toughness obtained by the Berkovich tip. The average fracture toughness calculated by the cube-corner tip is 0.53 MPa.m<sup>1/2</sup> for Sample 1, 0.57 MPa.m<sup>1/2</sup> for Sample 2, 0.38 MPa.m<sup>1/2</sup> for Sample 3, and 0.41 MPa.m<sup>1/2</sup> for Sample 4. Similar to the Berkovich tip, the acceptable and excessive loads are identified by examining the images. Nonetheless, acquiring consistent fracture toughness values for a solid medium is challenging as the two tips have different empirical coefficients (Gupta et al., 2020) **(Test 2)**.



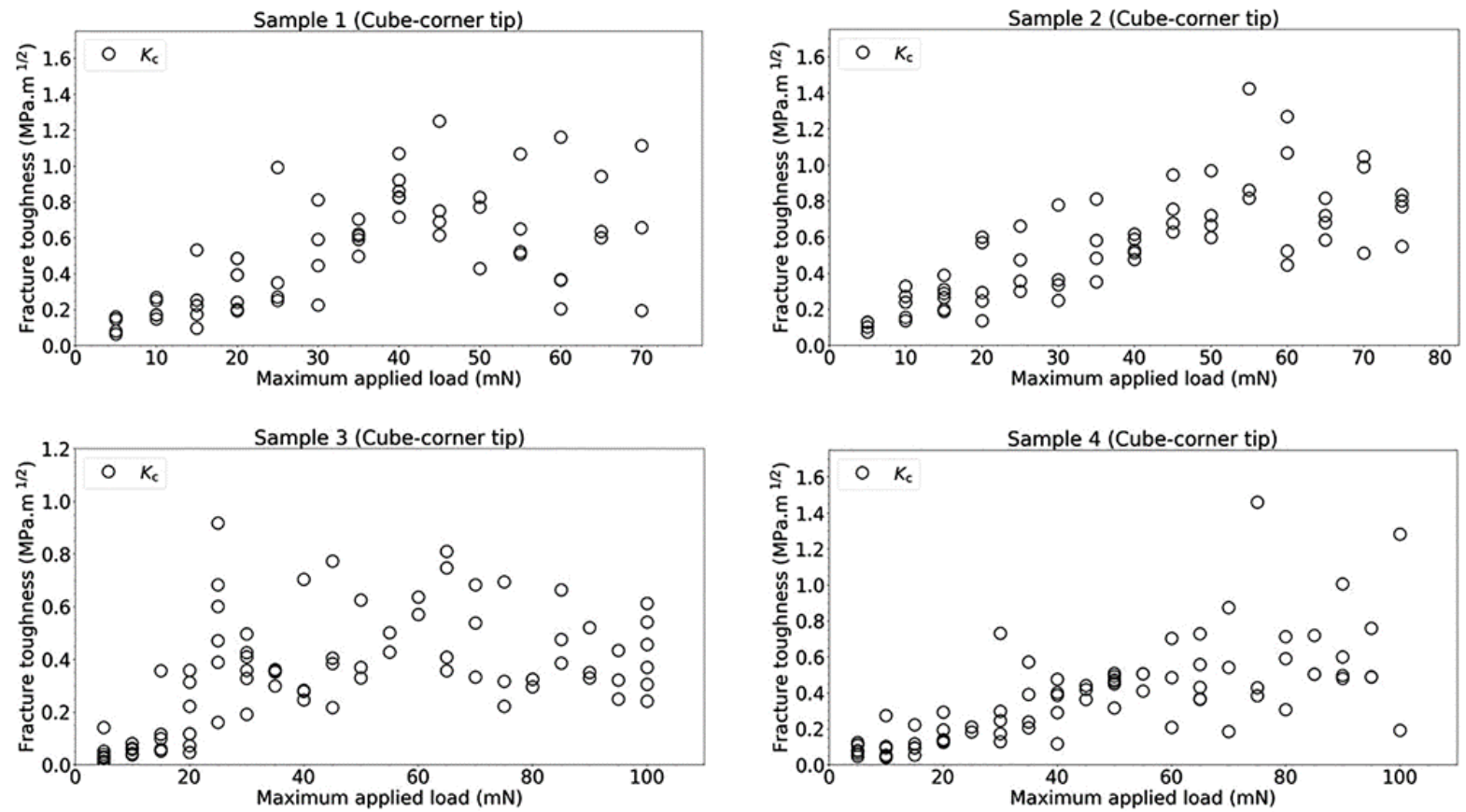


Figure 4.10—The fracture toughness values of four shale samples tested by the cube-corner tip.

Figure 4.10 depicts the average fracture toughness indented by the cube-corner tip. The cube-corner tip is similar to the Berkovich tip, with three-sided pyramids that induce a relatively similar impression. The only difference is that the contact angle is smaller in the cube-corner tip, which allows it to create fractures more easily than in the Berkovich tip (Table 2.1). The interpreted fracture toughness values based on the cube-corner tip are close to those shown in Figure 4.9. The average fracture toughness values using the two tip geometries are determined to compare the results. The average values for the parallel samples (1 and 2) are larger than those for the perpendicular samples (3 and 4).

Nanoindentation at different locations yields different results because it captures heterogeneous properties. Therefore, the average results obtained in Figure 4.9 and Figure 4.10 help to explain the overall behavior. Large scatter in fracture toughness values are also reported in the literature (Chandler et al., 2016; Ghidelli et al., 2017; Tran et al., 2014). In general, researchers consider a method acceptable when it yields a correct order of magnitude (Chandler et al., 2016; Ghidelli et al., 2017; Tran et al., 2014). Figure 4.11 illustrates that the average fracture toughness values yield agreeable results. The difference in the average fracture toughness values is less than 18%; thus, the comparison provides a partial validation for the proposed conceptual model at the same scale (**Test 2**).

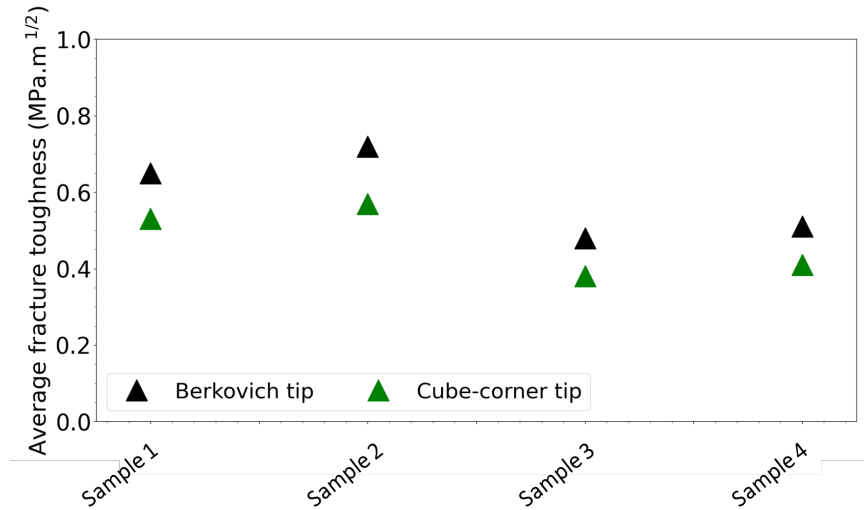


Figure 4.11—The average fracture toughness values of four shale samples using the Berkovich and cube-corner tips.

#### 4.5. Discussion

The primary objective of this study was to propose a conceptual model to characterize the fracture toughness of shale using nanoindentation. The model was based on how the fracture's length is interpreted and more apparent when the indenter tip lands between grains. This study revealed the absence of the ideal fracture pattern discussed in some literature (Figure 2.9). However, more probable scenarios existed with one or two fractures.

The proposed conceptual model clarified why the ideal fracture pattern was not observed in shale. The solid domain in the model is a combination of stronger and weaker domains that are intertwined. The impressions do not generate any fractures when the tip lands on the stronger domain. Instead, the conceptual model interprets the equivalent fracture length when the tip hits a weaker domain. The clarification was achieved by showing any possible distribution for the grains with different minerals on

the shale samples. The conceptual model justified the significant change between the ideal fracture patterns of homogeneous media in the literature and those observed in this study.

Creating a relatively simple fracture pattern was easier using the Berkovich tip than the cube-corner tip. The latter typically leads to a complex fracture pattern or larger damaged area without easy-to-detect fractures. In general, the Berkovich tip was more suitable for fracture toughness characterization in shale, whereas the cube-corner tip enabled partial validation of the proposed conceptual model at the same scale.

Another consideration was the anisotropic behavior of shale, where the bedding planes play an important role in controlling it. As a result, three scenarios of fracture propagation on a core scale (Figure 4.12) were defined in the literature that accounts for the relative orientation of the fracture plane with respect to the bedding planes (Zhang, 2013). Nevertheless, applying the defined scenarios for characterizing anisotropic fracture toughness was difficult while implementing nanoindentation.

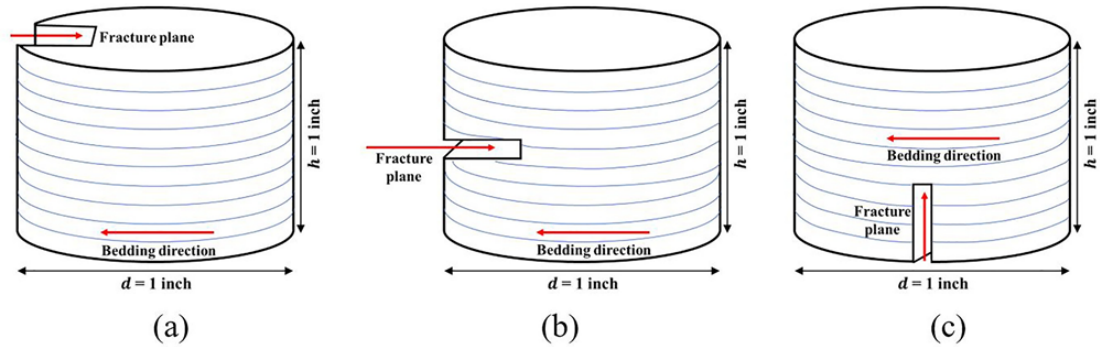


Figure 4.12—Three classifications of fracture propagation at the core scale (Zhang, 2013) are divider (a), short transverse (b), and arrester (c).

The bedding planes determined at a core scale do not necessarily constrain fracture propagation at a small scale. Hence, the fracture toughness values observed at a core scale may differ from the predicted values at a small scale. There is a need to develop a method applicable to small samples in practice because large samples are often unavailable. Moreover, a better sense of the fracture toughness at a small scale would improve understanding of how induced fractures contribute to the flow at different scales. It may also be possible to upscale the interpreted fracture toughness to a large scale (Graham-Brady and Huq, 2013; Paliwal and Ramesh, 2008).

Figure 4.13 clarifies shale's anisotropic behavior and its impact on the bedding planes at a core scale where fractures propagate as a result of nanoindentation. It represents two scenarios of the bedding planes, indicated by the blue lines, based on the proposed conceptual model. The tip may hit the bedding planes in a parallel sample, and the applied load is insufficient to form a fracture with a size that is closer to the core size. The induced fractures are more likely to propagate only in a single layer for the perpendicular sample and not interfere with other layers or planes (Figure 4.13b). This study shows that the interpreted fracture toughness is more representative of the local properties of a single layer.

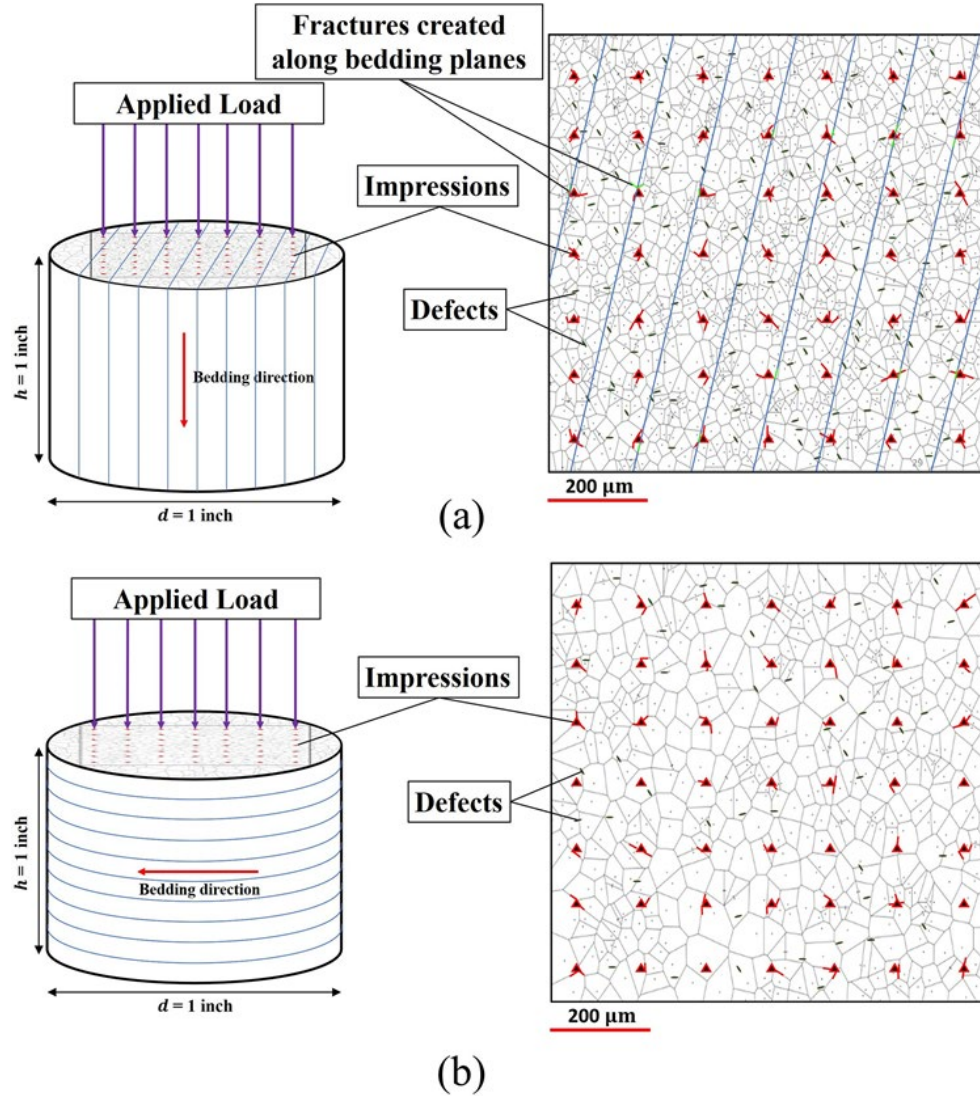


Figure 4.13—Conceptual illustrations of the anisotropic shale samples: parallel (a) and perpendicular (b) to the bedding planes. Fractures were induced at a small scale using nanoindentation. The triangles are the impression or indented area; the red and green marks represent simple fracture patterns produced through the grain boundaries and between the layers, respectively.

A Voronoi diagram generator created the Voronoi splitting in Figure 4.13 to represent the random distribution of the grains with various mineral components. The Voronoi diagrams in Figures 4.2 and 4.13 conceptualize a random distribution of the

grains. The boundaries may be related to distinct mineral types, geometry structures, or improper sample preparation. Identifying grains with specific mineralogy is beyond the scope of this study.

The predicted values of the cube-corner tip were used to validate the interpreted fracture toughness resulting from the Berkovich tip based on the proposed conceptual model. This is possible because the values predicted from the two tip geometries were compared on the same scale, smaller than the core scale. In addition, the two tip geometries required various external loads that lead to different fracture lengths; thus, the induced fracture patterns also differ. As a result, the comparison between the interpreted values of the two tips is significant.

Large-scale measurements on the core plugs provide additional evidence to check the proposed conceptual model. The one-to-one comparison between the Berkovich and cube-corner tips is explained in the subsequent chapter. However, based on the information available in the literature, the predicted values appear to be in the correct order for US shale formations. For instance, researchers who work in independent laboratory measurements have reported that the Chevron-notch short bar is in the range of 0.69 to 1.16 MPa.m<sup>1/2</sup> (Tran et al., 2014), the short rod approach is in the range of 0.12 to 1.39 MPa.m<sup>1/2</sup> (Chandler et al., 2016), and the three-point bending test is 0.85 MPa.m<sup>1/2</sup> (Jin et al., 2018).

## 4.6. Conclusions

This study proposed a conceptual model to characterize the fracture toughness of shale using nanoindentation. The proposed model assumed that the shale matrix comprises two intertwined, solid domains. One domain is weaker and fails when loaded, resulting in fractures or damage, whereas the other remains intact. The model was based on the effective-medium theory and adopted for the first time for fracture toughness characterization. The classic model is applicable to symmetrical (ideal) fracture patterns, which are abundant in homogeneous media, such as fused silica.

This study tested four shale samples from the Wolfcamp Formation. Two samples were parallel to the bedding planes, and the other two were perpendicular to the bedding planes. Shale with different loads was systematically tested. The applied loads that were acceptable for fracture toughness characterization were considered to be those in which the induced fractures formed a relatively simple pattern. Conversely, applied loads were deemed excessive if they led to complex fracture patterns or intersected each other.

The interpreted fracture toughness obtained from the Berkovich tip was partially validated with the cube-corner tip at the same scale. Samples 1 and 2 were parallel to the bedding planes, and Samples 3 and 4 were perpendicular. For the Berkovich tip, the fracture toughness values were  $0.65 \text{ MPa}\cdot\text{m}^{1/2}$  and  $0.72 \text{ MPa}\cdot\text{m}^{1/2}$  for Samples 1 and 2, respectively; Samples 3 and 4 were  $0.48 \text{ MPa}\cdot\text{m}^{1/2}$  and  $0.51 \text{ MPa}\cdot\text{m}^{1/2}$ , respectively. In comparison, the average fracture toughness values calculated by the cube-corner tip



were  $0.53 \text{ MPa.m}^{1/2}$  and  $0.57 \text{ MPa.m}^{1/2}$  for Samples 1 and 2, respectively, and  $0.38 \text{ MPa.m}^{1/2}$  and  $0.41 \text{ MPa.m}^{1/2}$  for Samples 3 and 4, respectively.

The interpreted results from the cube-corner tip were consistent with those from the Berkovich tip. Comparing the average fracture toughness values yielded agreeable results with less than 18% difference. The model revealed the complexities in characterizing shale using nanoindentation. Moreover, it explained why induced fracture patterns differ from the ideal pattern defined in most literature by partially validating the predicted fracture toughness of the samples indented by the cube-corner tip with those of the Berkovich tip. The proposed conceptual model promises to be implemented in shale at the same scale. The next chapter will explain how the model will be fully tested by comparing shale fracture toughness at different scales using nanoindentation against independent laboratory testing.

## CHAPTER 5. EVALUATION OF ANISOTROPIC SHALE FRACTURE TOUGHNESS USING NANOINDENTATION AND CRACKED CHEVRON NOTCHED BRAZILIAN DISC (CCNBD) TESTS

The content of this chapter is still under review in the *Rock Mechanics and Rock Engineering* (Esatyana et al., 2021). This chapter validates the results obtained from nanoindentation based on the proposed conceptual model against standard laboratory testing using the CCNBD test.

### 5.1. Sample descriptions

This study uses four shale samples from the Wolfcamp Formation extracted from an outcrop. Samples are divided into two groups. Samples A and B are parallel to the bedding planes, and Samples C and D are perpendicular to the bedding planes. Prior to indentation, samples are first used for the CCNBD test. Table 5.1 lists the pertinent sample properties.

Table 5.1 – The pertinent properties of the studied shale.

Group	1		2	
Sample	A	B	C	D
Direction to the bedding	Parallel	Parallel	Perpendicular	Perpendicular
Length (in)	0.8	0.8	0.8	0.8
Diameter (in)	1.98	1.98	1.98	1.98
Weight (g)	107.32	107.84	107.81	107.79

Table 5.2 (continued)

Description				
-------------	---	--	---	---

**5.2. Experimental procedure**

The predicted anisotropic fracture toughness of shale using the conceptual model (hybrid grid system) proposed by Esatyana et al. (2021) on core plugs and cuttings remains unverified against the International Society for Rock Mechanics (ISRM) methods. This study validates the results with the reported fracture toughness of the CCNBD test. Detailed experimental procedures of the CCNBD test and nanoindentation testing are explained subsequently.

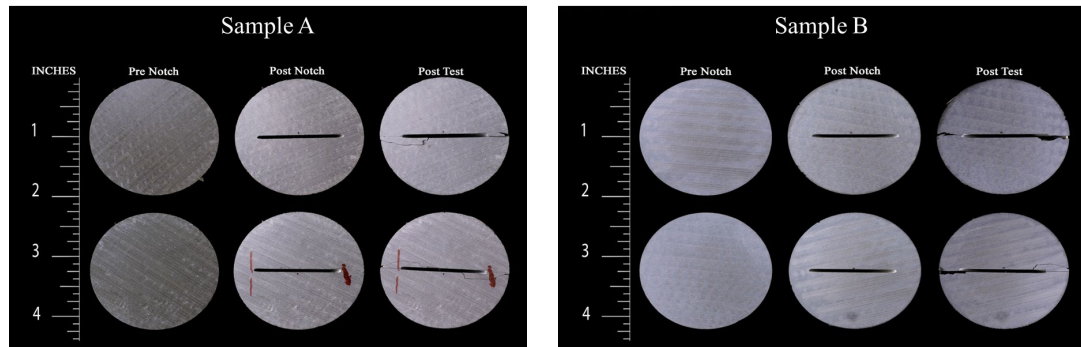
**5.2.1. CCNBD test**

It is challenging to determine the bedding planes with the naked eye. At this stage, microscope, and compressive wave (acoustic) analysis define the direction of the bedding planes. Next, Meta Rock Laboratories tests the samples using the CCNBD test. The results are documented in Table 5.2 (**Test 3**).

Table 5.3—Typical CCNBD test results on four shale samples during pre-notch, post-notch, and post-test (fracture test).

Sample	A	B	C	D
Fracture Plane (Figure 5.2)	Arrester	Arrester	Divider	Divider
Initial Notch Length (in)	0.27	0.19	0.24	0.27
Final Notch Length (in)	0.66	0.64	0.65	0.64
$F_{max}$ (N)	4,118	4,430	4,127	3,749
$K_{IC}$ (MPa.m <sup>1/2</sup> )	0.772	0.797	0.759	0.687

The notch is essential for the fracturing stage. Before breaking the sample, an initial notch is cut in the center with a rotary diamond saw. Next, each sample is placed between two flat plates and compressed by a diametral load (Fowell and Xu, 1993). The subtle lines on the sample's surface (Figure 5.1) are drill marks formed during sample preparation.



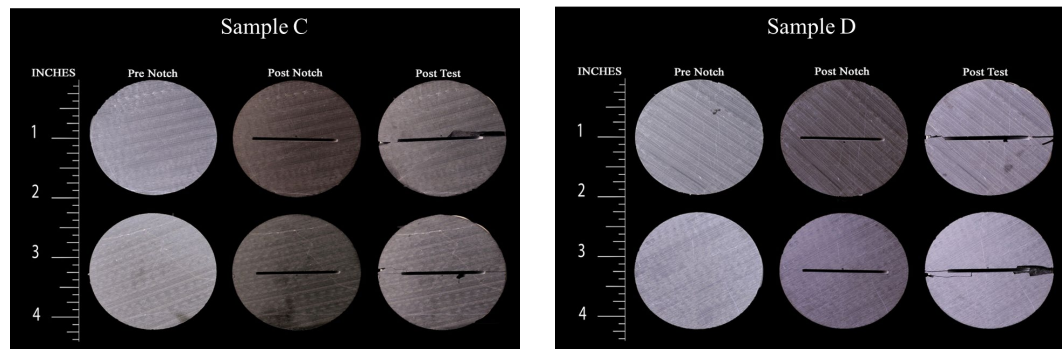


Figure 5.1—Cracked Chevron Notched Brazilian Disc (CCNBD) test of the shale samples. The three stages are pre-notch, post-notch, and post-test.

The direction of the bedding planes controls the anisotropic behavior of the rock sample. However, the direction is hardly visible if the sample is dense. The fracture orientation relative to the bedding planes determines the fracture principles. Chandler et al. (2016) classified three fracture propagation principles on a core scale as Divider, Arrester, and Transverse, which are discussed subsequently.

A notch is cut as a pre-fracture stage of the CCNBD test. In the perpendicular sample, the notch direction is perpendicular to the bedding planes, but the fracture propagates parallel to the bedding planes and is referred to as the Divider orientation. In the parallel sample, there are two possibilities of fracture propagation principles. The notch direction and fracture propagate parallel to the bedding planes in the transverse orientation. In the Arrester orientation, the notch direction and fractures are perpendicular to the bedding planes, which is relevant to this study.

Each sample direction matches one of the three principal fracture plane orientations relative to the bedding planes, based on the notch direction and fracture propagations, as illustrated in Figure 5.10. For instance, parallel and perpendicular

samples correspond to Divider and Arrester orientation. Besides, the predicted fracture toughness of the perpendicular sample is lower than the parallel sample, which shows consistency with the reported fracture plane orientation values in some literature studies (Inskip et al., 2018; Ren et al., 2020).

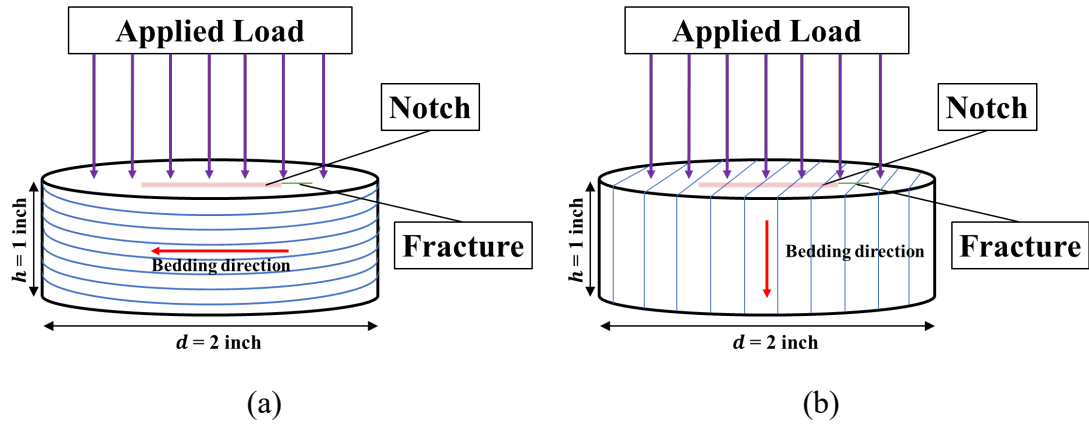


Figure 5.2—Notch and fracture propagation orientations when perpendicular (a) and parallel (b) to the bedding planes (blue lines). The perpendicular and parallel samples match Divider and Arrester orientations, respectively.

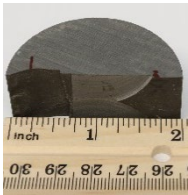
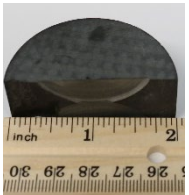
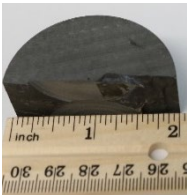
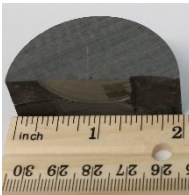
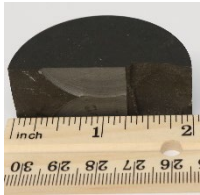
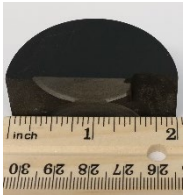
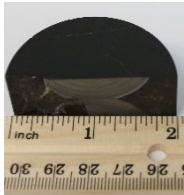
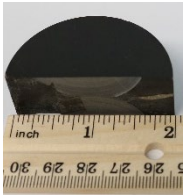
The CCNBD test is a standard laboratory test to determine anisotropic fracture toughness on the core scale. However, in practice, the CCNBD test may be impossible because of the lack of large samples. This study validates the predicted fracture toughness based on the conceptual model proposed by Esatyana et al. (2021) by comparing the indentation testing against the CCNBD test.

### 5.2.2. Nanoindentation on core plugs

The indenter tip is sensitive to local defects or microstructures, lowering mechanical properties such as Young's modulus and hardness values. Esatyana et al. (2020) have comprehensively studied the sensitivity of sample preparation in grinding

and polishing stages to Young’s moduli of shale samples. Table 5.3 depicts the surface of a semicircular shale sample before and after preparation.

Table 5.4—The semicircular shale surface before and after sample preparation. The surface of a sample is more reflective of light upon completion.

Condition	A	B	C	D
Unpolished				
Polished				

High-resolution images classify applied loads as acceptable or excessive by analyzing the generated fracture patterns. The distance between indents must be larger than the plastic zone to avoid interference between the stimulated regions. Esatyana et al. (2020) reported that the minimum spacing distance between indents for shale samples was 100 microns when the load was equal to 500 mN. The hybrid grid system in Figure 5.3 applies various loads on the surface of a sample to better capture shale heterogeneity. The applied loads increase from 50 to 1,000 mN with 50 mN incremental because there is no direct way to assign the maximum load before nanoindentation. The trial and error of various loads at different locations evaluate the creation of relatively simple fracture patterns on the surface of shale (**Test 3**).

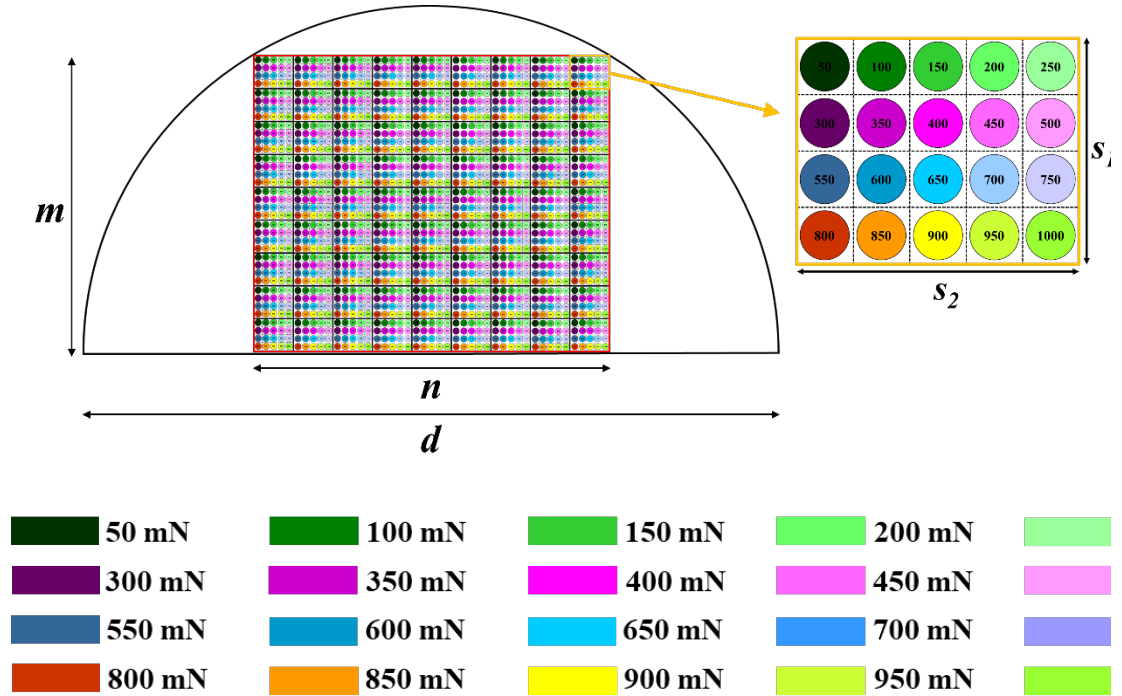


Figure 5.3—Hybrid grid system of a semicircular shale sample. The diameter ( $d$ ) of the core sample varies (Table 5.1). The major grid ( $m \times n$ ) pattern is  $9 \times 9$ , which is equal in size to  $0.566 \times 0.708$  in. The minor grid ( $s_1 \times s_2$ ) pattern is  $5 \times 4$ , which is equal in size to  $0.062 \times 0.078$  in.

### 5.2.3. Nanoindentation on cuttings

After indenting the semicircular samples, the next step is to characterize the fracture toughness of the cuttings. A heavy-duty steel rock crusher (Figure 5.4a) breaks the semicircular into pieces (Figure 5.4b) and pulverizes them. To operate the equipment, the operator puts a semicircular sample into a cylinder, steps on the base, inserts the plunger, and moves the plunger back and forth.





(a)

Sample A



Sample B



Sample C



Sample D

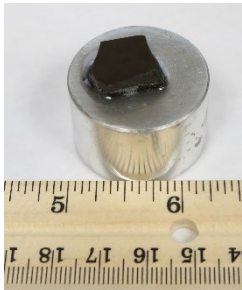
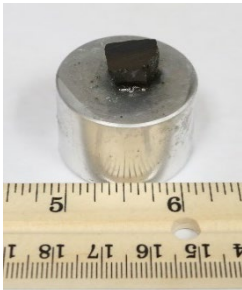
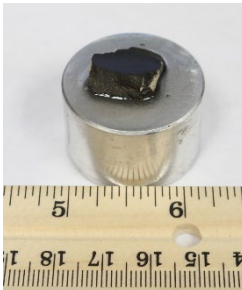

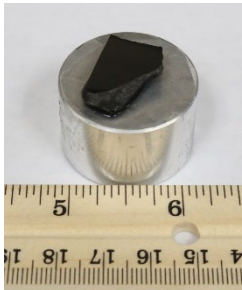
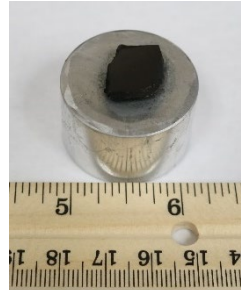
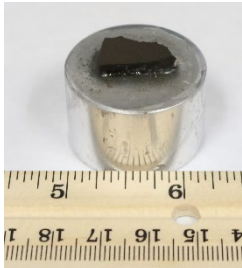

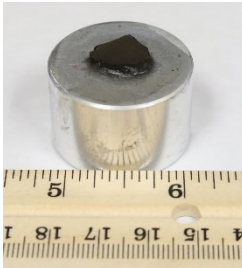
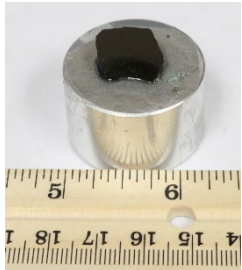
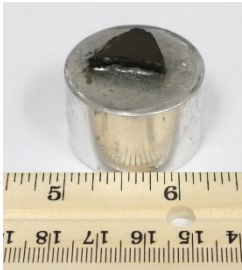
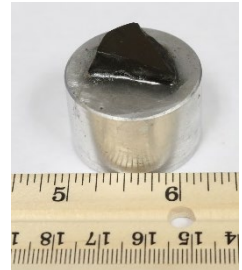


(b)

Figure 5.4— Rock crusher (a) and shale cuttings (b) obtained from the semicircular samples shown in Table 5.3.

The cuttings are glued to an aluminum puck to ensure sufficient resistance to the indentation load. Similar to the nanoindentation of the semicircular samples, sample preparation is necessary to reduce errors caused by local defects. Cuttings of irregular shapes can complicate the preparation by tearing the discs apart. Suitable cuttings must be well-positioned with minimal glue attached to the puck, as depicted in Table 5.4.

Table 5.5—Prepared samples glued to an aluminum puck for indentation.

Sample	Cutting no. 1	Cutting no. 2	Cutting no. 3
A			
B			
C			
D			

The size of cuttings ranges from 0.009 to 0.0295 in. to achieve a smooth surface and ensure the sample reliably captures the shale's properties. The smallest size is obtained by dividing the number of acceptable fracture patterns by the total number of indents. The cuttings of Sample C have the smallest size, with only two out of twelve indents equal to 0.17 in. Esatyana et al. (2020) showed that smaller samples lead to significant errors (**Test 3**).

Nanoindentation on cuttings does not account for the hybrid grid system because of the limited surface area. Therefore, the acceptable spacing between indents equals 0.086 in. when the maximum applied load is 500 mN (Esatyana et al., 2020). Moreover, it is more difficult to identify the direction of bedding planes in cuttings than in larger samples (**Test 3**).

## **5.3. Results**

### **5.3.1. Nanoindentation on core plugs**

After performing the tests, the predicted fracture toughness values of the semicircular samples are compared with the CCNBD test results, as shown in Table 5.3. The four shale samples generated 6,480 high-resolution images; each sample was given 1,620 indents. Figure 5.5 clarifies the relevant parameters, such as  $a$ ,  $l$ , and  $c$ , based on high-resolution images of indented samples.

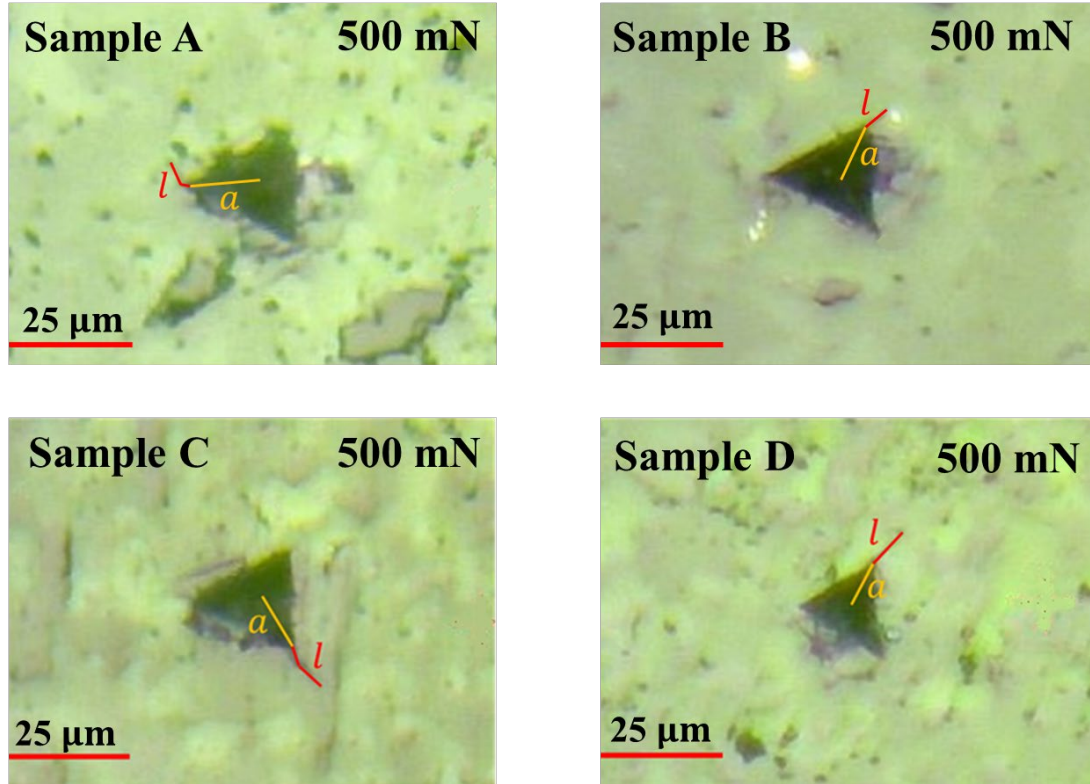


Figure 5.5—Impressions of the Berkovich tip on the surface of shale parallel (Samples A and B) and perpendicular (Samples C and D) to the bedding planes, where the applied load is 500 mN.

The characterized fracture toughness is anisotropic because the nanoindentation accounts for the fracture length created in various directions. Only the images with relatively simple fracture patterns are used to identify fracture length for anisotropic fracture toughness characterization. Table 5.5 provides detailed parameters obtained from the high-resolution images in Figure 5.5 to calculate the fracture toughness in different directions.

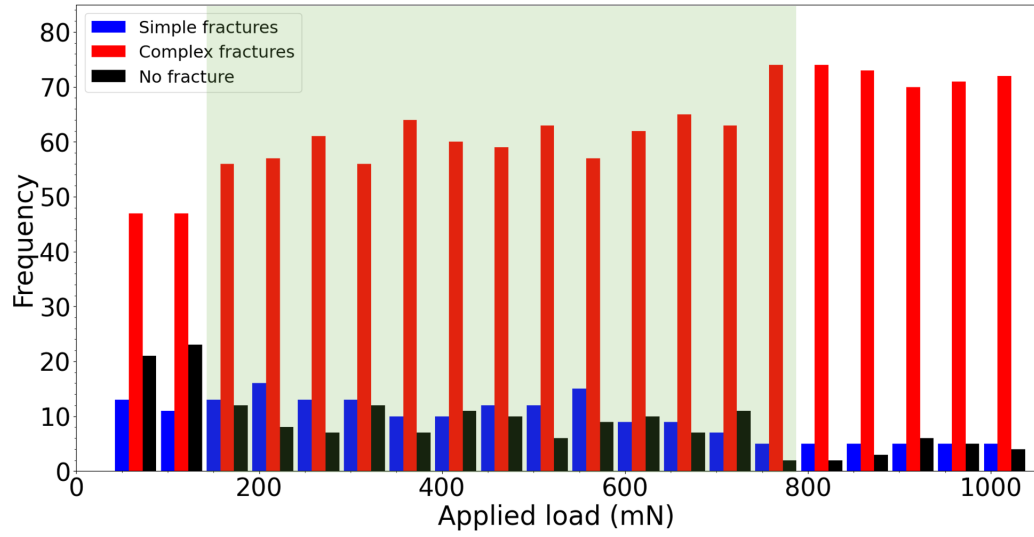
Table 5.6—The relevant parameters for fracture toughness characterization of shale samples using nanoindentation. The high-resolution images are shown in Figure 5.4.

Description, unit	Parameter	Sample			
		A	B	C	D
Distance from the center to the corner, microns	$a$	15.81	18.03	14.14	13.21
Distance from the corner to the tip, microns	$l$	11.18	7.07	11.18	9.19
Fracture length, microns	$c$	26.99	25.10	25.32	22.40
Empirical coefficient, dimensionless	$\alpha$	0.016	0.016	0.016	0.016
Young's modulus, GPa	$E$	51.70	72.10	64.40	34.80
Hardness, GPa	$H$	1.64	2.30	2.10	1.68
Maximum applied load, mN	$P_{max}$	500	500	500	500
Fracture toughness, MPa.m <sup>1/2</sup>	$K_c$	0.677	1.01	0.691	0.682

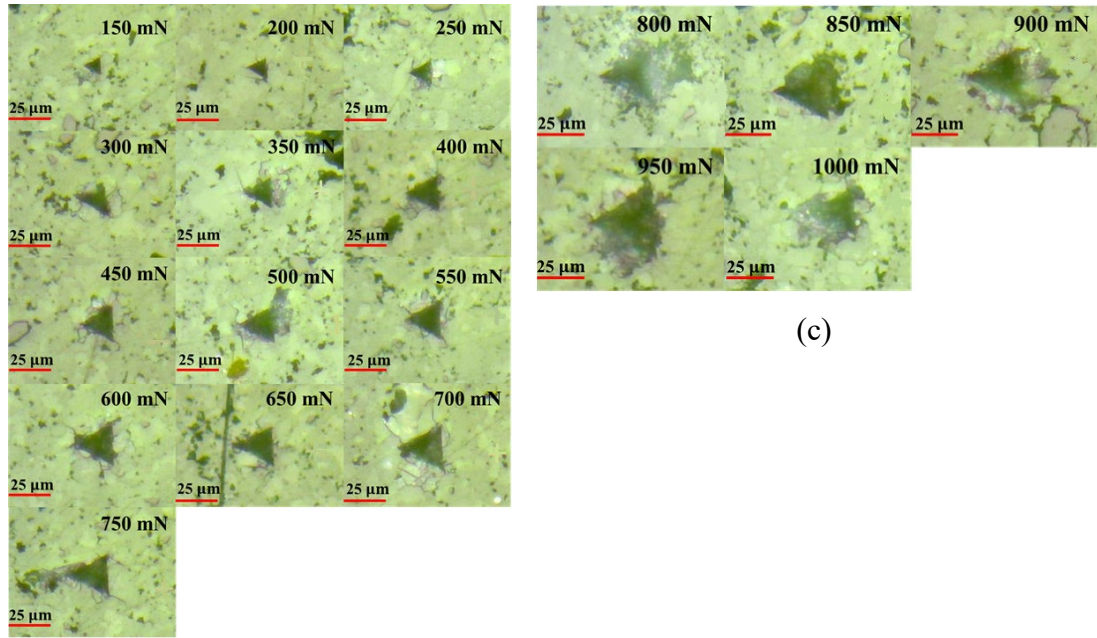
The histogram shows the acceptable load based on the fracture pattern (Figure 5.6a). Results are discarded when the applied load is smaller than or equal to 100 mN because the induced fractures are hardly discernible. Figure 5.6 reveals the total number of different fracture patterns (simple, complex, and no fracture) with the load for Sample A. The histogram of Samples B, C, and D are presented in Appendix A.

Fracture length is a significant parameter in characterizing fracture toughness from the experiment. The green box in Figure 5.6a indicates the acceptable loads to calculate fracture toughness where the number of simple fractures is notable. For instance, the acceptable load range of sample A is 150 to 750 mN. For Samples B, C, and D, the load ranges are 150 to 700 mN, 150 to 650 mN, and 150 to 750 mN, respectively.

When the load is in the range of 50 to 100 mN, it does not capture the sample behavior properly. The histogram of Samples A, B, C, and D illustrates this behavior clearly. The total number of no fractures in those ranges is higher than other loads, meaning that the load does not impact the sample yet. At 150 mN, the total number of no fractures decreases as the number of complex fractures increases. Therefore, the acceptable range begins when the load equals 150 mN.



(a)



(c)

(b)

Figure 5.6— Histogram of Sample A (parallel to the bedding) in three regions with various loads (a). High-resolution images where the applied load is acceptable when (b) smaller than or equal to 750 mN and (c) excessive when larger than 750 mN.



Figure 5.7 illustrates the interpreted fracture toughness values of the semicircular shale samples, where the detailed calculations are provided for four samples in Table 5.5. Samples A and B are parallel to the bedding planes, whereas Samples C and D are perpendiculars. Therefore, each sample has a different load range. The fracture toughness varies between 0.023 to 2.888 MPa.m<sup>1/2</sup> for Sample A; 0.056 to 3.060 MPa.m<sup>1/2</sup> for Sample B; 0.105 to 2.107 MPa.m<sup>1/2</sup> for Sample C; and 0.048 to 2.958 MPa.m<sup>1/2</sup> for Sample D. By averaging the data denoted by the red circles in each sample, the average predicted fracture toughness of Samples A, B, C, and D is 0.677, 0.725, 0.701, and 0.668 MPa.m<sup>1/2</sup>, respectively. Details are listed in Table 5.6.

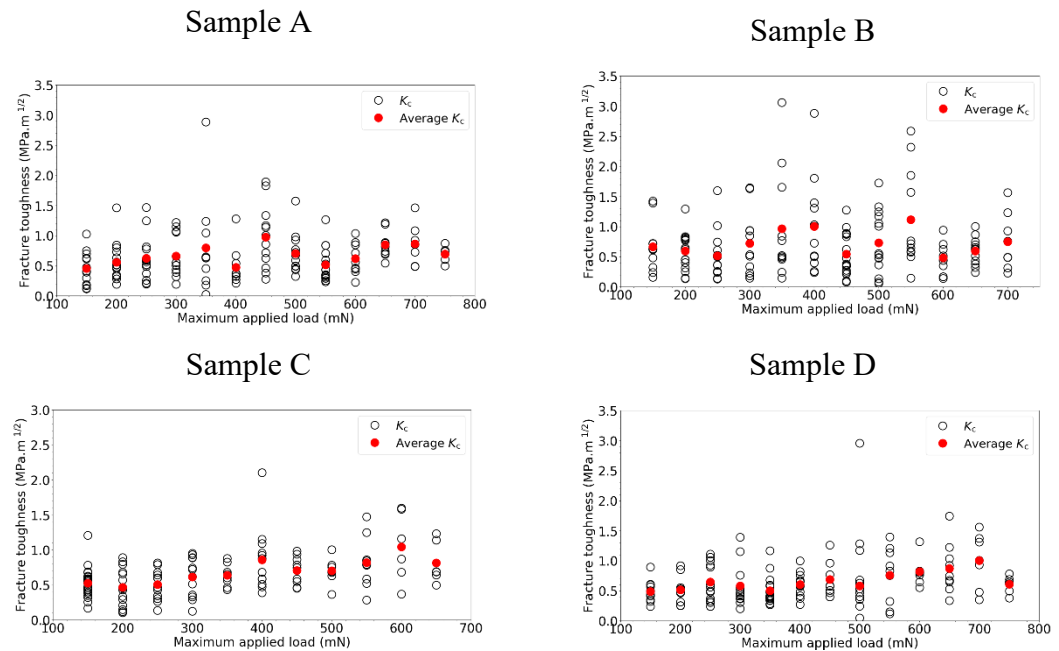
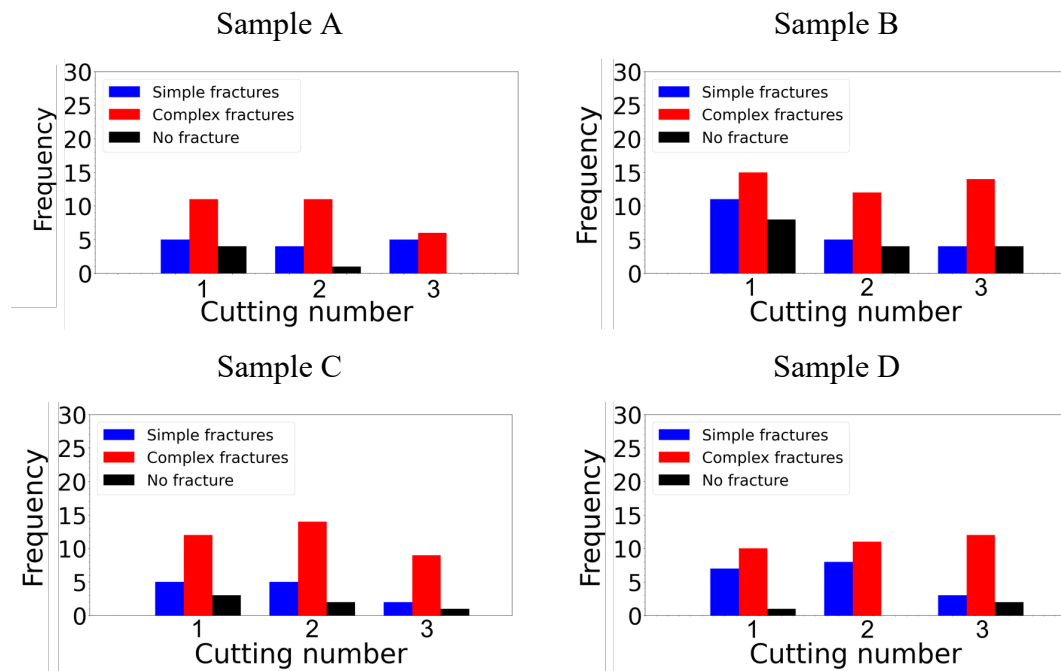


Figure 5.7— Fracture toughness values of four shale samples are listed in Table 5.3. The data shows 144 out of 1,620 tests that led to simple fracture patterns for Sample A; 198 out of 1,620 tests for Sample B; 194 out of 1,620 tests for Sample C; and 184 out of 1,620 tests for Sample D.



### 5.3.2. Nanoindentation on cuttings

Sample preparation for cuttings also consisted of grinding and polishing stages, which was challenging because cuttings broke into pieces easily. On the surface of shale cuttings, the maximum number of indentations reached up to thirty in total, where at least five to ten indents generated simple fracture patterns. The hybrid grid system was not implemented to characterize shale cuttings. Figure 5.8 shows the number of tests obtained on shale cuttings (Table 5.4).



(a)

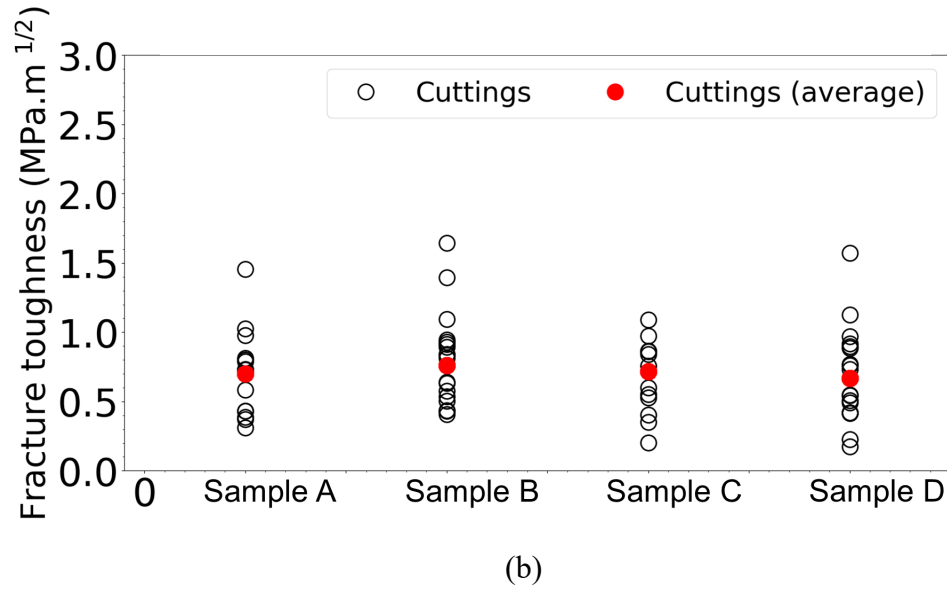


Figure 5.8—Histogram of the number of indents where the maximum applied load is 500 mN (a). The fracture toughness of shale cuttings shows that 14 out of 47 tests led to simple fractures for Sample A; 20 out of 77 tests for Sample B; 12 out of 53 tests for Sample C; and 18 out of 54 tests for Sample D (b).

#### 5.4. Validation

I hypothesize that the shale matrix is represented by two intertwined solid domains. One domain remains intact when loaded, whereas the other domain is weaker and results in fractures. The fracture toughness is estimated if I only account for the failure of the weaker domain. A fracture only occurs when the tip hits the weaker domain to characterize the relevant shale properties using nanoindentation. Based on the high-resolution images, simple fracture patterns determine fracture toughness in shale when their lengths are smaller than 20 microns. It is difficult to measure fracture toughness in a complex pattern where the length is greater than 25 microns. Therefore,

indentations within complex patterns and without fractures are excluded from fracture toughness characterization (**Hypothesis 2**).

The proposed conceptual model represents a shale matrix that comprises various minerals to form the grains. The boundary between the grains formed the weaker domain. Therefore, the model is realistic for shale to better capture its heterogeneity. Heterogeneity is caused by mineral composition and pores (**Hypothesis 2**).

The nanoindentation results from core plugs and cuttings based on the proposed conceptual model are compared with the CCNBD test results for validation purposes at different scales. The average values of the parallel samples (A and B) are larger than those of the perpendicular samples (C and D) using nanoindentation, which is consistent with the measured fracture toughness from the CCNBD test. Local defects or microstructures influence the indentation testing results, where their presence reduces the sample resistance against deformation and the quality of the mechanical properties of shale samples. Furthermore, several factors account for the sensitivity of nanoindentation that may contribute to mechanical properties, such as tip rounding, pile up and sink in, and surface roughness, which would require further study (Fischer-Cripps, 2011). Figure 5.9 represents the calculated shale fracture toughness of the cuttings and core plugs from nanoindentation against the independent laboratory measurement.

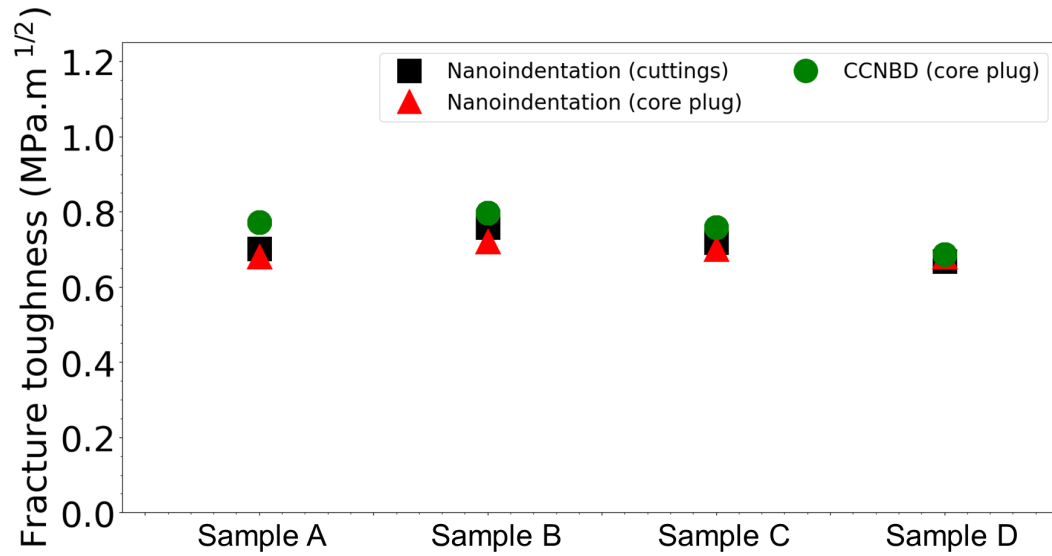


Figure 5.9—The average fracture toughness of the shale samples based on nanoindentation and the CCNBD test.

Table 5.7—The average anisotropic fracture toughness of the shale samples.

Sample	Applied load (N)	CCNBD test (MPa.m <sup>1/2</sup> )	Nanoindentation			
			Applied load (mN)	Core plug (MPa.m <sup>1/2</sup> )	Applied load (mN)	Cuttings (MPa.m <sup>1/2</sup> )
A	4,118	0.772	150-750	0.677	500	0.701
B	4,127	0.797	150-700	0.725	500	0.758
C	4,430	0.759	150-650	0.701	500	0.717
D	3,749	0.687	150-750	0.668	500	0.668

This study compared the predicted fracture toughness values with the CCNBD test, a standard laboratory experiment on a large scale, to validate the nanoindentation results. The error associated with the fracture toughness characterization based on nanoindentation is quantified as follows:

$$\text{Error (core plug)} = \left| \frac{K_{c \text{ core plug}}^{\text{average}} - K_{IC \text{ CCNBD}}}{K_{IC \text{ CCNBD}}} \right| \times 100\% \quad (5.1)$$

$$\text{Error (cuttings)} = \left| \frac{K_{c \text{ cuttings}}^{\text{average}} - K_{IC \text{ CCNBD}}}{K_{IC \text{ CCNBD}}} \right| \times 100\% \quad (5.2)$$

where  $K_{c \text{ core plug}}^{\text{average}}$  is the average fracture toughness on core plug predicted from nanoindentation,  $K_{c \text{ cuttings}}^{\text{average}}$  is the average fracture toughness on cuttings predicted from nanoindentation, and  $K_{IC \text{ CCNBD}}$  is the fracture toughness obtained from the CCNBD test.

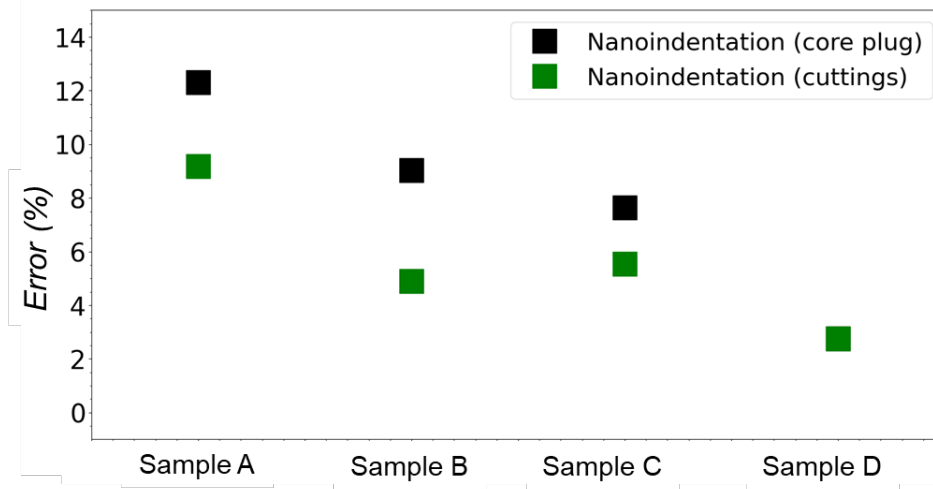


Figure 5.10—The error associated with the predicted shale anisotropic fracture toughness using nanoindentation (core plugs and cuttings) with the CCNBD results for validation purposes.

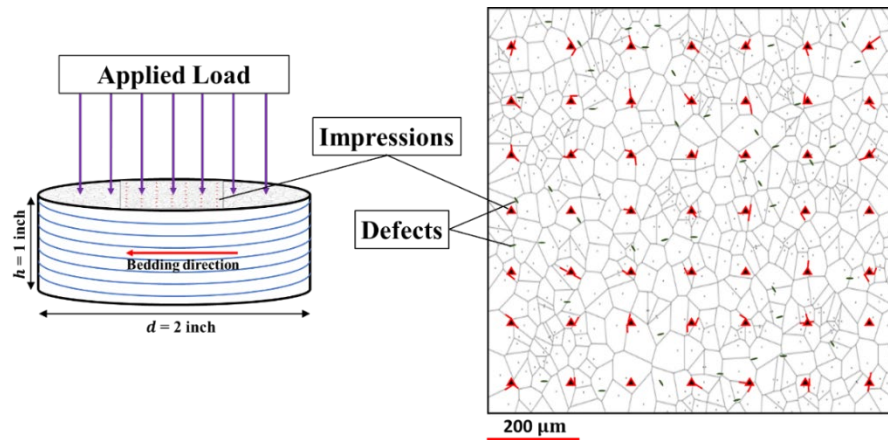
The plot in Figure 5.10 reveals the accuracy of the fracture toughness characterization based on nanoindentation by calculating the error of the predicted value relative to the CCNBD experiment. The error is in the range of 3% to 13% for core plugs and 3% to 10% for cuttings. The small error shows that nanoindentation

characterizes the anisotropic fracture toughness of shale with reasonable accuracy compared to the standard method (**Test 3**).

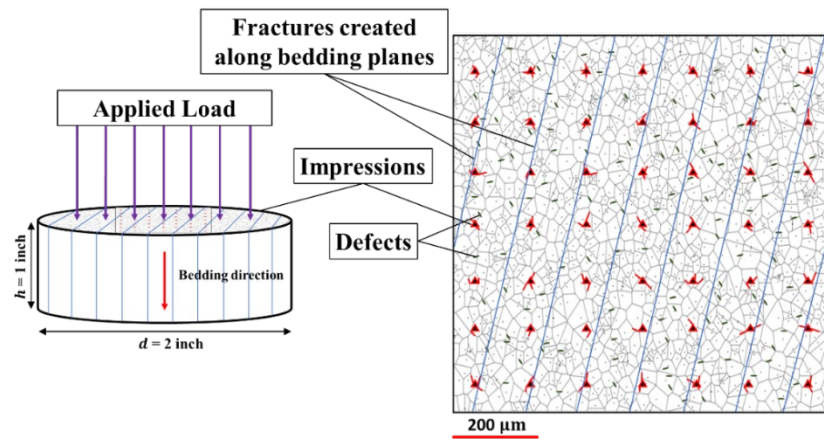
## **5.5. Discussion**

Following the CCNBD test, indentation testing is applied on semicircular core plugs and cuttings. This study aims to characterize shale fracture toughness using the recently proposed model (Esatyana et al., 2021) based on nanoindentation and validate the results with the CCNBD test. The proposed conceptual model accounts for two intertwined solid domains. Fractures generate when the tip hits on a weaker domain, while no fracture is formed when the tip lands on a stronger domain. The high-resolution images of shale core plugs and cuttings obtained from nanoindentation were 6,711 in total.

Nanoindentation accounts for the directional dependence of fracture toughness when the load is applied in various directions relative to the bedding plane. The Berkovich tip forms the impressions (indented area). The red marks represent the simple fractures generated between the grain boundaries and the bedding layers. The green marks show defects. In perpendicular samples, fractures propagate within a layer, while fractures spread through the bedding planes in parallel samples. Figure 5.11 further clarifies the directional dependency of the fracture toughness on a core plug using nanoindentation.



(a)



(b)

Figure 5.11—Conceptual illustrations of shale samples that are perpendicular (Fig. 3a) and parallel (Fig. 3b) to the bedding planes (blue lines) and the induced fractures on the surface of shale using nanoindentation (Esatyana et al., 2021).

In practice, high-resolution images reveal the complexity of the fracture patterns formed on the surface of shale. Esatyana et al. (2021) identified three significant

configurations of fracture patterns: simple fractures, complex fractures, and no fracture, based on their applied loads.

Figure 5.7 depicts a large scatter of the predicted fracture toughness from nanoindentation, ranging from 0.1 to 3.1 MPa.m<sup>1/2</sup>, even from the same type of rock and formation. The scatters have been examined to have strong correlations with the sample preparation, geometry dependency, size effect, and loading condition (Aliha et al., 2012). Regardless of the abundance of the data, information on the geometry dependency and size effect are still limited. Researchers have shown that the scatter could be attributed to preservation and hydration during sample preparation, as the water lowers fracture toughness (Wild et al., 2015).

The results of this study yield in good agreement with a standalone laboratory measurement conducted by the CCNBD test. Moreover, the predicted fracture toughness values also agree with data available in the literature. For example, Chandler et al. (2016) reported fracture toughness of Mancos shale using short-rod was in the range of 0.12 to 0.44 MPa.m<sup>1/2</sup>; Haynesville shale was 0.90 MPa.m<sup>1/2</sup> using straight notch Brazilian disc (Yuan et al., 2017); Woodford shale was in the range of 0.65 to 1.17 MPa.m<sup>1/2</sup> using Brazilian tensile test (Tran et al., 2014); Marcellus shale was in the range of 0.642 to 0.967 MPa.m<sup>1/2</sup> using three-point bending (Jin et al., 2018); Antrim shale was in the range of 0.032 to 0.111 MPa.m<sup>1/2</sup> using nanoindentation. It is recommended to test more samples not only from the same formation but also for other formations.



On a large scale, the induced fracture toughness can be defined as a pure mode I (tensile-dominated), mode II (shear-dominated), mode III (tearing-dominated), or mixed-mode (I/II, I/III, II/III, I/II/III). This study employed the CCNBD test that led to pure mode I in determining shale fracture toughness. In nanoindentation, mixed-mode fractures are commonly generated that can be either tensile- or shear-dominated.

## **5.6. Conclusions**

The key objective of this study was to determine the anisotropic fracture toughness of shale samples on the core scale using cuttings, then validate the results with the CCNBD test. Four shale samples were divided into two groups (parallel and perpendicular to the bedding planes). The complexities of fracture patterns on the surface of shale samples were clarified, in which the applied loads were considered excessive. The anisotropic fracture toughness was calculated based on linear elastic fracture mechanics.

Two independent laboratory tests determined the fracture toughness of the samples. The first test was the CCNBD, which validated the nanoindentation on core plugs and cuttings. As a result of the CCNBD test, the samples were halved. Next, the semicircular samples (core plugs) were prepared with a surface polisher and tested with nanoindentation using the Berkovich tip. The hybrid grid system was implemented in nanoindentation to better capture shale heterogeneity over an extensive surface area by applying various loads at different locations. The average fracture toughness was then

calculated based on the acceptable load ranges generated by relatively simple fracture patterns.

Afterward, the semicircular samples were crushed to obtain shale cuttings for the nanoindentation application. Because of the limited surface area with irregular shapes, it is challenging to accurately determine the bedding direction of the pieces and prepare the samples prior to indentation testing. Therefore, the only acceptable load for the shale cuttings was 500 mN, restricted by their size through a trial-and-error method. The CCNBD test validated the predicted anisotropic fracture toughness of the shale core plugs and cuttings from nanoindentation.

The average fracture toughness values obtained from nanoindentation were between 0.668 MPa.m<sup>1/2</sup> and 0.725 MPa.m<sup>1/2</sup> on core plugs; 0.668 MPa.m<sup>1/2</sup> and 0.758 MPa.m<sup>1/2</sup> on cuttings. The result is promising to concern the CCNBD test. For all analyzed samples, the error was between 2.76% and 12.3% on core plugs; 2.76% and 9.19% on cuttings. Therefore, determining the anisotropic shale fracture toughness using cuttings or core plugs yielded agreeable results to characterize large samples.

## **CHAPTER 6. ASSUMPTIONS AND LIMITATIONS**

This chapter discusses the pertinent assumptions and limitations of the conducted study. They are divided into the applications of nanoindentation for characterizing Young's modulus and fracture toughness. The limitations are also elaborated for thoroughness.

### **6.1. Indentation technique to determine Young's modulus of shale at the core scale using drill cuttings**

The assumption is that Young's modulus of shale on a core scale is equal to the average values obtained from nanoindentation at a regular spacing distance if the average values change less than 20% while decreasing the distance between indentations, as shown in Figure 3.7. The 20% differences in acceptable error are obtained because of a significant variety of Young's moduli in shale captured from nanoindentation and reported in the literature (Gupta et al., 2020; Shukla et al., 2013). The spacing distance defines the cuttings scale that is later implemented for small cuttings, as shown in Figure 3.8. The spacing of indents must be larger than the plastic zone to avoid interference between the stimulated regions.

The assumption is that nanoindentation captures a bulk property (instead of a local property) pertinent to a volume smaller than the core volume, which is compatible with the Sneddon solution. The justification is based on a solid medium that undergoes deformations in different locations, even at small loads. Johnson (1970) proposed a

relation to calculate the corresponding plastic zone size, as depicted in Figure 3.2, which can be approximated as

$$\frac{c_p}{a_r} = \left[ \frac{1}{6(1-\nu_s)} \left( \frac{E_s}{\sigma_{yield}} \tan\left(\frac{\pi}{2} - \theta\right) + 4(1 - 2\nu_s) \right) \right]^{\frac{1}{3}}, \quad (6.1)$$

where  $c_p$  is the plastic zone radius,  $a_r$  is the contact radius,  $\nu_s$  is Poisson's ratio of the sample,  $E_s$  is Young's modulus,  $\sigma_{yield}$  is the yield strength, and  $\theta$  is a geometrical parameter.

Hill (1963) proposed a conceptual illustration of the representative element volume (REV), which is equal to the corresponding distance ( $c_p$ ), whose repetition generates the bulk volume at a large scale, as depicted in Figure 3.3. Therefore, the assumption implies that there is a scale smaller than the core scale controlling the core-scale properties. A smaller scale refers to a cutting scale, which is unequal in different formations.

The first limitation is that the plastic zone size restricts the indentation spacing as a lower limit and the core size as an upper limit. If only small pieces are available, Young's modulus can be predicted from drill cuttings. It may be impossible to accurately determine the cutting scale for each formation because of the various sizes. However, estimating Young's moduli of a sample whose size is close to the cutting size should predict the values at the core scales.

The second limitation is the challenge of determining the bedding orientation in the cuttings—determining the bedding plane becomes more complicated when the sample is smaller. Characterizing anisotropic properties based on nanoindentation

involves various loads in different directions, which often becomes impossible because of the small size of the cutting. Thus, Young's modulus obtained in this study is treated as an effective isotropic response.

When applied to the field scale, the average Young's modulus obtained from the laboratory has certain limitations because of higher pressure and temperature in the field (Rinehart et al., 1961). The Young's modulus is often obtained from the Ultrasonic Pulse Wave Velocities (UPV), which is more reflective of dynamic behavior, and is influenced by overburden pressure through which the pulse waves must propagate (King, 1966). Consequently, some modifications are required to apply the laboratory measurements to the field scale.

There are differences between Young's moduli of laboratory and field values—there are competing effects when mapping the laboratory measurements to the field scale. The confinement in the subsurface increases Young's modulus, and there are also larger defects in the subsurface that weaken the sample. The importance of these effects should be assessed depending on the sample depth.

## **6.2. Proposed conceptual model**

The assumption for the proposed conceptual model is that two intertwined solid domains can represent the shale matrix. One domain is weaker and fails when loaded, resulting in fractures, whereas the other domain remains intact. Only the failure of the weaker domain is accounted for to calculate fracture toughness. A fracture occurs when the tip hits the weaker domain to characterize the relevant properties of shale using

nanoindentation. The high-resolution images show the simple fracture patterns when their lengths are smaller than 20 microns in shale. In comparison, complex patterns or damaged areas occur when the length exceeds 25 microns, which makes measurement difficult. Indentations within complex fracture patterns and without fracture are excluded from fracture toughness characterization.

The proposed conceptual model represents a shale matrix that comprises different minerals to form the grains. The boundary between the grains generated the weaker domain. The model is realistic to mimic shale heterogeneity caused by mineral composition and pores. It is challenging to define the shape and size of the mineral properties that correspond to the stronger domain.

The first limitation of the proposed conceptual model is that it does not account for the effects of the fluid-rock interaction to determine fracture toughness. For example, the injected fluid may alter the properties because of swelling. It may also influence the sample after recovery because of the escape of the saturation fluid. Despite a small amount of water that can increase the density of the sample, the velocities of compressional and shear waves are higher in the water-saturated than in the dry state (Kuster and Toksoz, 1974). Therefore, these fluid-rock interactions are not considered in this proposed model with this complexity.

The second limitation is that the acceptable load ranges vary even at the same formation from the same depth. The proposed model needs to be tested for other shale formations. This applicability needs further study because of shale heterogeneity and anisotropic behavior.

In indentation, the external load alters the stress in the sample, which in turn fractures the sample. The original stress field of the sample studied was unclear. The nanoindentation leads to mixed-mode fractures that are either tensile or shear-dominated. Field observations indicate hydraulic fracturing is also mixed-mode, but they are tensile-dominated (Lockner et al., 1992; Senseny and Pfeifle, 1984). Thus, the induced fracture mode in the laboratory has similarities to the field. Relating the fracture values of the laboratory to the field is not so trivial because of the difference between the scales.

## **CHAPTER 7. CONCLUDING REMARKS AND FUTURE WORKS RECOMMENDATIONS**

### **7.1. Concluding remarks**

#### **7.1.1. Indentation technique to determine Young's modulus of shale at the core scale using drill cuttings**

Shale is mechanically unstable and easily breaks into pieces. The proposed method is required because large samples (~1 in.) are often unavailable. The instability suggests nanoindentation as an alternative to standard core-scale measurements that often require large samples. Therefore, cuttings were the only source used to determine Young's modulus of shale at the core scale. A new method was developed to predict Young's modulus of shale at the core scale using drill cuttings.

1. In contrast to the homogeneous media such as aluminum, sample preparation significantly impacts nanoindentation results for shale. The average moduli captured from nanoindentation increased up to 83% after grinding but significantly less (~10%) after polishing. In general, grinding is more crucial than the polishing.
2. The suggested cutting size is 2.2 mm for characterizing Young's modulus of shale. The value can be lower than the suggested size as long as it is larger than the plastic size, which is 0.1 mm. Determining the plastic size is essential to avoid interference between the stimulated regions.
3. Young's moduli of shale at the core scale were between 51.48 and 89.52 GPa and on cuttings were between 35.98 and 62.85 GPa. The difference between the average



modulus based on nanoindentation and the independent core-scale measurements remained less than 30% for all the samples when the applied load equaled 500 mN.

### **7.1.2. Proposed conceptual model**

The conceptual model is based on two intertwined solid domains. One domain remains intact when loaded, while another domain is weaker, resulting in fractures. A fracture is generated when the tip hits the weaker domain. A conceptual model was proposed to characterize shale fracture toughness using nanoindentation to determine fracture toughness.

1. The ideal fracture patterns are absent in shale based on 20,424 high-resolution images. Simple fracture patterns are present when their lengths are smaller than 20 microns. In contrast, complex patterns are difficult to measure when their lengths are greater than 25 microns. Indentations within complex patterns and without fractures were excluded from fracture toughness characterization.
2. The proposed hybrid grid system was proposed, and it was used to identify the acceptable load ranges through trial and error. The fracture toughness was calculated based on the acceptable load ranges generated by relatively simple patterns.
3. The conceptual model proposed for fracture toughness characterization was tested at different scales. A cube-corner tip partially validated the proposed model on a small scale. Shale fracture toughness based on the cube-corner was 18% smaller than the Berkovich tip. This was an important milestone because acquiring consistent values using two tip geometries is challenging. The cube-corner tip has a sharper angle compared to the Berkovich tip.

4. The conceptual model was fully validated on a larger scale. In this regard, the cracked chevron notched Brazilian disc (CCNBD) test was initially performed. The results were used to validate the anisotropic fracture toughness of core plugs and cuttings using nanoindentation. The differences with the CCNBD test were between 2.76% and 12.3% for core plugs; and 2.76% and 9.19% for cuttings in all analyzed samples.

The experimental results of nanoindentation can be applied to the Finite Element Method (FEM). Young's moduli obtained from nanoindentation are used to calculate fracture toughness, an input for hydraulic fracturing design. It will specifically identify the sweet zone of the formation. A low fracture toughness value typically generates the fractures easily. By identifying this value, the target of the hydraulic fracturing technique is better located.

## **7.2. Future work recommendations**

### **7.2.1. Indentation technique to determine Young's modulus of shale at the core scale using drill cuttings**

Nanoindentation is sensitive to sample preparation. Although this study used an advanced surface polisher, the ion beam milling technique would likely provide a more polished surface. It remains difficult to prepare small samples because their shape is usually irregular, and it is even more challenging when the samples are brittle.

### **7.2.2. Proposed conceptual model**

The conceptual model was used for shale samples from the Wolfcamp Formation and yielded promising results. It worked well to predict the anisotropic fracture toughness of shale cuttings and core plugs using nanoindentation against the independent laboratory

measurements. However, the model needs to be tested on other shale formations. In addition, the applicability to other shale formations needs to be verified because of their heterogeneity. It is also recommended to test in other types of formations.

It is also impossible to assign the load a priori on shale samples. As a result, different loads at different locations are applied to determine the acceptable load ranges. The approach known as the hybrid grid system explores an extensive sample area to better characterize shale heterogeneity. This study used the maximum number of grids ( $9 \times 9$ ). It is suggested to have as many grids as possible to cover more area. The only consideration is that the spacing distance between indents must be larger than the plastic zone size to avoid interference between the stimulated regions.

This study used two tips for partial validation. The most used one was the Berkovich tip. It reflects a fully formed plastic zone where fractures may occur. Tip rounding occurs because it is often used, resulting in an initial elastic contact that does not capture the sample behavior. During indentation, the contact between the indenter tip and sample surface is predictably drawn inwards or downwards, causing pile-up or sink-in conditions. For the cube-corner tip, the topology is sharper than the Berkovich tip, causing tip rounding to occur more often than with the Berkovich tip. Therefore, replacing them in a specific timeframe is recommended to avoid tip rounding.

Subsequently, it is recommended to present a correlation to estimate mechanical properties based on the components of the sample. The correlation is crucial to observing the mechanical behavior of the sample. The measurements can use x-ray diffraction (XRD) and helium porosimeter to define its mineralogy, porosity, and organic content. The

observations are advantageous whether trends and results of the multivariate analysis result in a single shale match with other shales or types of formations.

## REFERENCES

- Abedi, S., Slim, M., Hofmann, R., Bryndzia, T., and Ulm, F.-J. 2016. Nanochemo-Mechanical Signature of Organic-Rich Shale: A Coupled Indentation-EDX Analysis. *Acta Geotechnica*, 11(3), 559–572. <https://doi.org/10.1007/s11440-015-0426-4>.
- Abousleiman, Y.N., Hull, K.L., Han, Y., Al-Muntasheri, G., Hosemann, P., Parker, S., and Howard, C.B. 2016. The Granular and Polymer Composite Nature of Kerogen-Rich Shale. *Acta Geotechnica*, 11, 573–594. <https://doi.org/10.1007/s11440-016-0435-y>.
- Acosta, J.A., Curtis, M.E., Wick, W., Sondergeld, C.H., and Rai, C.S. Study of Creep Behavior in Barnett Shale using Nanoindentation. Paper presented at the 55<sup>th</sup> U.S. Rock Mechanics/Geomechanics Symposium, Houston, Texas, USA, 20-23 June 2021. ARMA-21-2088.
- Al-Maharma, A.Y., and Sendur, P. 2018. Review of the Main Factors Controlling the Fracture Toughness and Impact Strength Properties of Natural Composites. *Materials Research Express*, 6(2), 1–30. <https://doi.org/10.1088/2053-1591/aec28>.
- Alehossein, H., and Hood, M. 1996. State-of-the-art Review of Rock Models for Disc Roller Cutters. In: Proceedings of the 2<sup>nd</sup> North American Rock Mechanics Symposium, Montreal, 1, 693–700.
- Aliha, M.R.M., Ayatollahi, M.R., and Akbardoost, J. 2012. Typical Upper Bound-Lower Bound Mixed-Mode Fracture Resistance Envelopes for Rock Material. *Rock Mechanics and Rock Engineering*, 45(1), 65–74. <https://doi.org/10.1007/s00603-011-0167-0>.
- Aliha, M.R.M., and Ayatollahi, M.R. 2013. Rock Fracture Toughness Study using Cracked Chevron Notched Brazilian Disc Specimen under Pure Modes I and II Loading – A Statistical Approach. *Theoretical Applied Fracture Mechanics*, 6, 17–25. <https://doi.org/10.1016/j.tafmec.2013.11.008>.
- Aliha, M.R.M., Bahmani, A., and Akhondi, S. 2015. Determination of Mode III Fracture Toughness for Different Materials using a New Designed Test Configuration. *Materials & Design*, 86, 863–871. <https://doi.org/10.1016/j.matdes.2015.08.033>.
- Aliha, M.R.M., Mahdavi, E., and Ayatollahi, M.R. 2018. Statistical Analysis of Rock Fracture Toughness Data Obtained from Different Chevron Notched and Straight Cracked Mode I Specimens. *Rock Mechanical and Rock Engineering*, 51(7), 2095–2114. <https://doi.org/10.1007/s00603-018-1454-9>.
- Alsteens, D., Muller, D.J., and Dufrene, Y.F. 2017. Multiparametric Atomic Force Microscopy Imaging of Biomolecular and Cellular Systems. *Accounts of Chemical Research*, 50(4), 924–931. <https://doi.org/10.1021/acs.accounts.6b00638>.
- Anderson, T.L. 1991. *Fracture Mechanics*, second edition. Boca Raton, Florida, USA: CRC Press.

- Andersen, M.A., Duncan, B., and McLin, R. 2013. Core Truth in Formation Evaluation. *Oilfield Review Summer*, 25(2), 16–25.
- Anstis, G.R., Chantikul, P, Lawn, B.R., and Marshall, D.B. 1981. A Critical Evaluation of Indentation Techniques for Measuring Fracture Toughness: I Direct Crack Measurements. *Journal of the American Ceramic Society*, 64, 533–538. <https://doi.org/10.1111/j.1151-2916.1981.tb10320.x>
- Arora V, Cai Y. 2014. U.S. Natural gas exports and their global impacts. *Applied Energy*, 120, 95–103. <https://doi.org/10.1016/j.apenergy.2014.01.054>.
- Asef, M. 2013. *Shale Engineering: Mechanics and Mechanisms*, first edition. CRC Press, Hoboken.
- Ashby, M.F. 1999. *Materials Selection in Mechanical Design*, second edition. Woburn, MA: Butterworth-Heinemann.
- Ast, J., Ghidelli, M., Durst, K., Göken, M., Sebastiani, M., and Korsunsky, A.M. 2019. A Review of Experimental Approaches to Fracture Toughness Evaluation at the Micro-Scale. *Materials and Design*, 173, 1–24. <https://doi.org/10.1016/j.matdes.2019.107762>.
- Atkins, A.G., and Tabor, D. 1965. Plastic Indentation in Metals with Cones. *Journal of the Mechanics and Physics of Solids*, 13, 149–164. [https://doi.org/10.1016/0022-5096\(65\)90018-9](https://doi.org/10.1016/0022-5096(65)90018-9).
- Ayatollahi, M.R., and Akbardoost, J. 2012. Size Effects on Fracture Toughness of Quasi-Brittle Materials-A New Approach. *Engineering Fracture Mechanics*, 92, 89–100. <https://doi.org/10.1016/j.engfracmech.2012.06.05>.
- Backers, T., Stephansson, O., and Rybacki, E. 2002. Rock Fracture Toughness Testing in Mode II – Punch-Through Shear Test. *International Journal of Rock Mechanics and Mining Sciences*, 39(6), 755–769. [https://doi.org/10.1016/S1365-1609\(02\)00066-7](https://doi.org/10.1016/S1365-1609(02)00066-7).
- Bell, T.J., Bendeli, A., Field, J.S., Swain, M.V., and Thwaite, E.G. 1991. The Determination of Surface Plastic and Elastic Properties by Ultra Microindentation. *Metrologia*, 28, 463–469. <https://doi.org/10.1088/0026-1394/28/6/004>.
- Berkovich, E.S. 1951. Three-Faceted Diamond Pyramid for Micro-hardness Testing. Translated into English: *Industrial Diamond Review in June 1951*, 11(127), 129–132.
- Berto, F. and Ayatollahi, M.R. 2011. Fracture Assessment of Brazilian Disc Specimens Weakened by Blunt V-Notches under Mixed Mode Loading by Means of Local Energy. *Materials and Design*, 32(5), 2858–2869. <https://doi.org/10.1016/j.matdes.2010.12.034>.
- Bhushan, B., and Gupta, B.K. 1991. *Handbook of Tribology: Materials, Coatings, and Surface Treatments*. Krieger Publishing Company, United States.

Bolshakov, A., and Pharr, G.M. 1998. Influences of Pileup on the Measurement of Mechanical Properties by Load and Depth Sensing Indentation Techniques. *Journal of Material Research*, 13(4), 1049–1058. <https://doi.org/10.1557/JMR.1998.0146>.

Brinell, J.A. 1925. Determine the Hardness of Different Materials.

Brown, L., Allison, P.G., and Sanchez, F. 2018. Use of Nanoindentation Phase Characterization and Homogenization to Estimate the Elastic Modulus of Heterogeneously Decalcified Cement Pastes. *Materials Design*, 142, 308–318. <https://doi.org/10.1016/j.matdes.2018.01.030>.

Campbell, J.S. 1891. *Flexible Driving Shaft* (US Patent No. 459,152) US Patent Office. [1498391536243342521-00459152 \(storage.googleapis.com\)](https://storage.googleapis.com/1498391536243342521-00459152)

Cappella, B., and Dietler, G. 1999. Force-Distance Curves by Atomic Force Microscopy. *Surface Science Reports*, 34, 1–104. [https://doi.org/10.1016/S0167-5729\(99\)00003-5](https://doi.org/10.1016/S0167-5729(99)00003-5).

Chandler, M.R., Meredith, P.G., Brantut, N., and Crawford, B.R. 2016. Fracture Toughness Anisotropy in Shale. *Journal of Geophysical Research: Solid Earth*, 121(3), 1706–1729. <https://doi.org/10.1002/2015JB012756>.

Cheatham, J.B., and Gnirk, P.F. 1967. The Mechanics of Rock Failure Associated with Drilling at Depth. In proceedings of the 8<sup>th</sup> US Symposium on Rock Mechanics, 410–439. ARMA-66-0410.

Chen, J., and Bull, S.J. 2007. On the Relationship between Plastic Zone Radius and Maximum Depth during Nanoindentation. *Surface and Coatings Technology*, 201(7), 4289–4293. <https://doi.org/10.1016/j.surfcoat.2006.08.099>.

Cheng, Y.T. and Cheng, C.M. 1998. Scaling Approach to Conical Indentation in Elastic-Plastic Solids with Work Hardening. *Journal of Applied Physics*, 84(3), 1284–1291. <https://doi.org/10.1063/1.368196>.

Cheng, Y.T., Li, Z., and Cheng, C.M. 2002. Scaling Relationships for Indentation measurements. *Philosophical Magazine A*, 82(10), 1821–1829. <https://doi.org/10.1080/01418610208235693>.

Crawford, B.R., Smart, B.G.D., Main, I.G., and Liakopoulou-Morris, F. 1995. Strength Characteristics and Shear Acoustic Anisotropy of Rock Core Subjected to True Triaxial Compression. *International Journal of Rock Mechanics and Mining Sciences and Geomechanics Abstracts*, 32(3), 189–200. [https://doi.org/10.1016/0148-9062\(94\)00051-4](https://doi.org/10.1016/0148-9062(94)00051-4).

Cook, R.F. and Pharr, G.M. 1990. Direct Observation and Analysis of Indentation Cracking in Glasses and Ceramics. *Journal of the American Ceramic Society*, 73(4), 787–817. <https://doi.org/10.1111/j.1151-2916.1990.tb05119.x>.

- Daneshy, A.A. 2003. Off-Balance Growth: A New Concept in Hydraulic Fracturing. *Journal of Petroleum Technology*, 55(04), 78–85. <https://doi.org/10.2118/80992-JPT>.
- Deirieh, A., Ortega, J.A., Ulm, F.J., and Abousleiman, Y. 2012. Nanochemomechanical Assessment of Shale: Coupled WDS- Indentation Analysis. *Acta Geotechnica*. 7(4), 271–295. <https://doi.org/10.1007/s11440-012-0185-4>.
- Doerner, M.F., and Nix, W.D. 1986. A Method for Interpreting the Data from Depth-Sensing Indentation Instruments. *Journal of Materials Research*, 1, 601–609. <https://dx.doi.org/10.1557/JMR.1986.0601>.
- Du, J., Hu, L., Meegoda, J.N., and Zhang, G. 2018. Shale Softening: Observations, Phenomenological Behavior, and Mechanisms. *Applied Clay Science*, 161, 290–300. <https://doi.org/10.1016/j.clay.2018.04.033>.
- Dukino, R.D., and Swain, M.V., 1992. Comparative Measurement of Indentation Fracture Toughness with Berkovich and Vickers Indenters. *Journal of the American Ceramic Society*, 75(12), 3299–3304. <https://doi.org/10.1111/j.1151-2916.1992.tb04425.x>.
- Engel, A., and Muller, D.J. 2000. Observing Single Biomolecules at Work with the Atomic Force Microscope. *Nature Structure Biology*, 7(9), 715–718. <https://doi.org/10.1038/78929>.
- Esatyana, E., Sakhaee-Pour, A., Sadooni, F.N., and Al-Kuwari, H.A-S. 2020. Nanoindentation of Shale Cuttings and Its Application to Core Measurements. *Petrophysics*, 61(5), 404–416. <https://doi.org/PJV61N5-2020a1>.
- Esatyana, E., Alipour, M., and Sakhaee-Pour, A. et al. 2021. Characterizing Anisotropic Fracture Toughness of Shale using Nanoindentation. *SPE Reservoir Evaluation and Engineering*, 1–13. SPE-205488-PA. <https://doi.org/10.2118/205488-PA>.
- Fitch, P., Davies, S., Lovell, M., and Pritchard, T. 2013. Reservoir Quality and Reservoir Heterogeneity: Petrophysical Application of the Lorenz Coefficient. *Petrophysics*, 54(5), 465–474. SPWLA-2013-v54n5-A5.
- Fischer-Cripps, A.C. 2011. *Nanoindentation*, third edition. Springer New York Dordrecht Heidelberg London.
- Fjær, E., and Nes, O-M. 2014. The Impact of Heterogeneity on the Anisotropic Strength of an Outcrop Shale. *Rock Mechanics and Rock Engineering*, 47, 1603–1611. <https://doi.org/10.1007/s00603-014-0598-5>.
- Fowell, R.J. 1995. Suggested Method for Determining Mode I Fracture Toughness using Cracked Chevron Notched Brazilian Disc (CCNBD) Specimens. *International Journal of Rock Mechanics and Mining Sciences & Geomechanics Abstracts*, 32(1), 57–64. [https://doi.org/10.1016/0148-9062\(94\)00015-U](https://doi.org/10.1016/0148-9062(94)00015-U).



- Gao, Q., Tao, J., Hu, J., and Yu, X.B. 2015. Laboratory Study on the Mechanical Behaviors of an Anisotropic Shale Rock. *Journal of Rock Mechanics and Geotechnical Engineering*, 7(2), 213– 219. <https://doi.org/10.1016/j.jrmge.2015.03.003>.
- Ghidelli, M., Sebastiani, M., Johanns, K.E., and Pharr, G.M. Effects of Indenter Angle on Micro-Scale Fracture Toughness Measurement by Pillar Splitting. *Journal of the American Ceramic Society*, 100(12), 5731–5738. <https://doi.org/10.1111/jace.15093>.
- Gu, M. 2018. Impact of Anisotropy Induced by Shale Lamination and Natural Fractures on Reservoir Development and Operational Designs. *SPE Reservoir Evaluation & Engineering*, 21(04), 1–13. SPE-191131-PA. <https://doi.org/10.2118/191131-PA>.
- Gupta, I., Sondergeld, C., and Rai, C. 2020. Fracture Toughness in Shale using Nanoindentation. *Journal of Petroleum Science and Engineering*, 191, 1–8. <https://doi.org/10.1016/j.petrol.2020.107222>.
- Gokaraju, D., Govindarajan, S., Mitra, A., Aldin, M., and Patterson R. 2017. Evaluation of Fracture Toughness and Its Impact on Hydraulic Fracturing. Paper presented at the 51<sup>st</sup> U.S. Rock Mechanics/Geomechanics Symposium, San Fransisco, California, USA, June 2017. ARMA-2017-0590.
- Gomes, J.P., Chandra, S.R., and Sondergeld, C.H. 2007. Effect of Microstructure and Pore Fluid on the Elastic Properties of Carbonates. In proceedings of the SEG/San Antonio 2007 Annual Meeting, 1565–1569. SEG-2007-1565.
- Gouldstone, A., Koh, H.J., Zeng, K.Y., Giannakopoulos, A.E., and Suresh, S. 2000. Discrete and Continuous Deformation during Nanoindentation of Thin Films. *Acta Materialia*, 48(9), 2277–2295. [https://doi.org/10.1016/S1359-6454\(00\)00009-4](https://doi.org/10.1016/S1359-6454(00)00009-4).
- Graham-Brady, L. and Huq, F. 2013. Upscaling Crack Propagation and Random Interactions in Brittle Materials Under Dynamic Loading. *Procedia IUTAM*, 6, 108-113. <https://doi.org/10.1016/j.piutam.2013.01.012>.
- Griepentrog, M., Kramer, G., and Cappella, B. 2013. Comparison of Nanoindentation and AFM Methods for the Determination of Mechanical Properties of Polymers. *Polymer Testing*, 32(3), 455–460. <https://doi.org/10.106/j.polymertesting.2013.01.011>.
- Griffith, A.A. 1920. The Phenomena of Rupture and Flow in Solids. *Philosophical Transactions of the Royal Society of London Series A*, 221, 163–198.
- Grim, R.E. 1947. Relation of Clay Mineralogy to Origin and Recovery of Petroleum. *AAPG Bulletin*, 31(8), 1491–1499. <https://doi.org/10.1306/3D933A1F-16B1-11D7-8645000102C1865D>.
- Gupta, I., Sondergeld, C., and Rai, C. 2018. Applications of Nanoindentation for Reservoir Characterization in Shale. In: Proceedings of the 52<sup>nd</sup> U.S. Rock Mechanics/Geomechanics Symposium, Washington.

Gupta, I., Sondergeld, C., and Rai, C. 2020. Fracture Toughness in Shales using Nanoindentation. *Journal of Petroleum Science and Engineering*, 191, 1–8. <https://doi.org/10.1016/j.petrol.2020.107222>.

Hagoort, J. 1981. Waterflood-Induced Hydraulic Fracturing. Ph.D. Thesis.

Hahn, G.T., and Rosenfield, A.R. 1975. Metallurgical Factors Affecting Fracture Toughness of Aluminum Alloys. *Metallurgical Transactions*, 6, 653–668. <https://doi.org/10.1007/BF02672285>.

Hertz, H. 1881. On the Contact of Elastic Solids. *Journal für die reine und angewandte Mathematik*, 92, 156–171. Translated and reprinted in English in *Hertz's Miscellaneous Papers*, Macmillan & Co., London, 1896, Ch. 5.

Hill, R. 1950. *The Mathematical Theory of Plasticity*, Clarendon Press, Oxford.

Hill, R. 1963. Elastic Properties of Reinforced Solids: Some Theoretical Principles. *Journal of the Mechanics and Physics of Solids*, 11(5), 357–372. [https://doi.org/10.1016/0022-5096\(63\)90036-X](https://doi.org/10.1016/0022-5096(63)90036-X).

Hill, D.G., Lombardi, T.E., and Martin, J.P. 2004. *Fractured Shale Gas Potential in New York*.

Höök, M., Davidsson, S., Johansson, S., and Tang, X. 2014. Decline and Depletion Rates of Oil Production: A Comprehensive Investigation. *Philosophical Transactions of The Royal Society Series A*, 372, 20120448. <https://doi.org/10.1098/rsta.2012.0448>.

Hornby, B.E., Schwartz, L.M., and Hudson, J.A. 1994. Anisotropic Effective Medium Modeling of the Elastic Properties of Shale. *Geophysical Journal International*, 59(10), 1570–1583. <https://doi.org/10.1190/1.1443546>.

Hughes, J.D. 2013. Energy: A Reality Check on the Shale Revolution. *Nature*, 494, 307–308. <https://doi.org/10.1038/494307a>.

Inskip, N.D.F, Meredith, P.G., Chandler, M.R., and Gudmundsson, A. 2018. Fracture Properties of Nash Point Shale as a Function of Orientation to Bedding. *Journal of Geophysical: Solid Earth*, 123(10), 8428–8444. <https://doi.org/10.1029/2018JB015943>.

Irwin, G.R. 1957. Analysis of Stresses and Strains Near the End of a Crack Traversing a Plate. *Journal of Applied Mechanics*, 24, 361–364.

Irwin, G.R. 1968. Linear Fracture Mechanics, Fracture Transition, and Fracture Control. *Engineering Fracture Mechanics*, 1(2), 241–257. [https://doi.org/10.1016/0013-7944\(68\)90001-5](https://doi.org/10.1016/0013-7944(68)90001-5).

ISO 4287. 1997. Geometrical Product Specifications (GPS)–Surface Texture: Profile Method–Terms. Definitions and Surface Texture Parameters. Geneva, Switzerland: International Organization of Standardization.

ISO 14577. Metallic Materials – Instrumented Indentation Test for Hardness and Materials Parameters.

Javadpour, F. 2009. Nanopores and Apparent Permeability of Gas Flow in Mudrocks (Shale and Siltstone). *Journal of Canadian Petroleum Technology*, 48(8), 16–21. <https://doi.org/10.2118/09-08-17-DA>.

Jennings, H.M., Thomas, J.J., Gevrenov, J.S., Constantinides, G., and Ulm, F.J. 2005. Nanostructure of CSH Gel in Cement Paste as a Function of Curing Conditions and Relative Humidity. In proceedings: International Conference on Creep, Shrinkage and Durability of Concrete and Concrete Structures, Conreep7, Ecole Centrale de Nantes, France, 19–37 September. URL: <https://www.researchgate.net/publication/283716499>. Accessed July 22, 2020.

Jha, K.K., Suksawang, N., Lahiri, D., and Agarwal, A. 2012. Energy-based Analysis of Nanoindentation Curves for Cementitious Materials. *ACI Materials Journal*, 109(1), 81–90.

Jiang, W-G., Su, J-J., and Feng, X-Q. 2008. Effect of Surface Roughness on Nanoindentation Test of Thin Films. *Engineering Fracture Mechanics*, 75(17), 4965–4972. <https://doi.org/10.1016/j.engfracmech.2008.06.016>.

Jin, Z., Li, W., Jin, C., Hambleton, J., and Cusatic, G. 2018. Anisotropic Elastic, Strength, and Fracture Properties of Marcellus Shale. *International Journal of Rock Mechanics and Mining Sciences*, 109, 124–137. <https://doi.org/10.1016/j.ijrmms.2018.06.009>.

Johnson, K.L. 1970. The Correlation of Indentation Experiments. *Journal of the Mechanics and Physics of Solids*, 18(2), 115–126. [https://doi.org/10.1016/0022-5096\(70\)90029-3](https://doi.org/10.1016/0022-5096(70)90029-3).

Johnson, K.L. 1985. *Contact Mechanics*. Cambridge University Press.

Karimi, M. 2013. Drill-Cuttings Analysis for Real-Time Problem Diagnosis and Drilling Performance Optimization. Paper presented at the SPE Asia Pacific Oil and Gas Conference and Exhibition, Jakarta, Indonesia, October 2013. <https://doi.org/10.2118/165919-MS>.

Khan, S., Ansari, S., Han, H., and Khosravi, N. 2011. Importance of Shale Anisotropy in Estimating In-Situ Stresses and Wellbore Stability Analysis in Horn River Basin. Paper presented at the Canadian Unconventional Resources Conference, Calgary, Alberta Canada, November 2011. <https://doi.org/10.2118/149433-MS>.

Khrushchov, M.M., and Berkovich, E.S. 1950. Method of Determining the Hardness of Very Hard Materials: The Hardness of Diamond. Translated into English: *Industrial Diamond Review in February 1951*, 11, 42–49.

- King, M.S. 1966. Wave Velocities in Rocks as a Function of Changes in Overburden Pressure and Pore Fluid Saturants. *Geophysics*, 31(1), 50–73. <https://doi.org/10.1190/1.1439763>.
- King, M.S. 1983. Static and Dynamic Elastic Properties of Rocks from the Canadian Shield. *Journal of Rock Mechanics and Mining Sciences & Geomechanics Abstracts*, 20(5), 237–241. [https://doi.org/10.1016/0148-9062\(83\)90004-9](https://doi.org/10.1016/0148-9062(83)90004-9).
- Klein, C.A., and Cardinale, G.F. 1993. Young's Modulus and Poisson's ratio of CVD Diamond. *Diamond and Related Materials*, 2(5–7), 918–923. [https://doi.org/10.1016/0925-9635\(93\)90250-6](https://doi.org/10.1016/0925-9635(93)90250-6).
- Kuster, G.T., and Toksoz, M.N. 1974. Velocity and Attenuation of Seismic Waves in Two-Phase Media: Part I. Theoretical Formulations. *Geophysics*, 39(5), 587–606. <https://doi.org/10.1190/1.1440450>.
- Laugier, M.T. 1986. Indentation Cracking in Ceramics and Cermets. Paper presented at the 2<sup>nd</sup> International Conference – Science of Hard Metals, Rhodes, Greece, 23–28 September, edited by Almond, E.A., Brookes, C.A., and Warren, R. Institute of Physics Conference Series 75. Science of Hard Materials. 1986. *Institute of Physics Conference Series*, 449.
- Laugier, M.T. 1987. New Formula for Indentation Toughness in Ceramics. *Journal of Materials Science Letters*, 6(3), 355–356. <https://doi.org/10.1007/BF01729352>.
- Lawn, B.R., Evans, A.G., and Marshall, D.B. 1980. Elastic/Plastic Indentation Damage in Ceramics: The Median/Radial Crack System. *Journal of the American Ceramic Society*, 63(9–10), 574–581. <https://doi.org/10.1111/j.1151-2916.1980.tb10768.x>
- Lawn, B.R., and Howes, V.R. 1981. Elastic Recovery at Hardness Indentations. *Journal of Materials Science*, 16, 2745–2752. <https://doi.org/10.1007/BF02402837>.
- Lee, G., Ong, S.H., Azeemuddin, M., and Goodman, H. 2012. A Wellbore Stability Model for Formations with Anisotropic Rock Strengths. *Journal of Petroleum Science and Engineering*, 96–97, 109–119. <https://doi.org/10.1016/j.petrol.2012.08.010>.
- Lee, J.S., Jacobi, D., and Alnajar, Z. Rock Mechanical Characterization of Unconventional Source Rocks. Paper presented at the SPE Middle East Oil and Gas Show and Conference held in Manama, Bahrain, 18–21 March 2019. <https://doi.org/10.2118/194953-MS>.
- Li, H., Ghosh, A., Han, Y.H., and Bradt, R.C. 1993. The Frictional Component of the Indentation Size Effect in Low Load Microhardness Testing. *Journal of Material Research*, 8(5), 1028–1032. <https://doi.org/10.1557/JMR.1993.1028>.
- Li, X.D., Diao, D.F., Bhushan, B. 1997. Fracture Mechanics of Thin Amorphous Carbon Films in Nanoindentation. *Acta Materialia*, 45(11), 4453–4461. [https://doi.org/10.1016/S1359-6454\(97\)00143-2](https://doi.org/10.1016/S1359-6454(97)00143-2).

- Li, W., and Sakhaee-Pour, A. 2016. Macroscale Young's Moduli of Shale Based on Nanoindentation. *Petrophysics*, 57(6), 597–603.
- Liu, Y. 2015. Fracture Toughness Assessment of Shale by Nanoindentation. Masters Thesis. University of Massachusetts, Amherst, MA. <https://doi.org/10.7275/jzym-1g18>.
- Liu, K., Ostadhassan, M., and Bubach, B. 2016. Application of Nanoindentation Methods to Estimate Nanoscale Mechanical Properties of Shale Reservoir Rocks. *Journal of Natural Gas Science and Engineering*, 35, 1310–1319. <https://doi.org/10.1016/j.jngse.2016.09.068>.
- Liu, G., and Ehlig-Economides, C.A. 2018. Practical Considerations for Diagnostic Fracture Injection Test (DFIT) Analysis. *Journal of Petroleum Science Engineering*, 171, 1133–1140. <https://doi.org/10.1016/j.petrol.2018.08.035>.
- Liu, K., Ostadhassan, M., and Wang, H. 2018. Creep Behavior of Shale-Nanoindentation Experiments. Paper presented at the 52<sup>nd</sup> US Rock Mechanics/Geomechanics Symposium, Seattle, Washington, USA, 17–20 June 2018. ARMA-2018-692.
- Lopez, B., Piedrahita, J., and Aguilera, R. 2015. Estimates of Stress Dependent Properties in Tight Reservoirs: Their Use with Drill Cuttings Data. Paper presented at the SPE Latin American and Caribbean Petroleum Engineering Conference, Quito, Ecuador, November 2015. <https://doi.org/10.2118/177189-MS>.
- Marshall, D., and Lawn, B. 1985. Indentation of Brittle Materials. *Microindentation Techniques in Materials Science and Engineering*, 17, 26–46. <https://doi.org/10.1520/STP32950S>.
- Market Report. 2021, September. *Shale Gas Global Market Report 2020-30: Covid-19 Growth and Change*. Retrieved from [Shale Gas Global Market Report 2020-30: COVID-19 Growth And Change \(reportlinker.com\)](https://www.reportlinker.com/Shale-Gas-Global-Market-Report-2020-30-COVID-19-Growth-And-Change)
- Marshall, D.B., Noma, T., and Evans, A.G. 1980. A Simple Method for Determining Elastic-Modulus-to-Hardness Ratios using Knoop Indentation Measurements. *Journal of the American Ceramic Society*, 65, C175–C176. <https://doi.org/10.1111/j.1151-2916.1982.tb10357.x>
- Maurer, W.O. 1967. The State of Rock Mechanics Knowledge in Drilling. In: Fairhurst (Ed.), *Proceedings of the 8<sup>th</sup> US Symposium on Rock Mechanics*, 355–395. ARMA-66-0355.
- Mavko, G., Mukerji, T., and Dvorkin, J. 2009. *The Rock Physics Handbook: Tools for Seismic Analysis of Porous Media*. Cambridge University Press. <https://doi.org/10.1017/CBO9780511626753>.

- Mayerhofer, M.J., and Economides, M.J. 1993. Permeability Estimation From Fracture Calibration Treatments. Paper presented at the SPE Western Regional Meeting, Anchorage, Alaska, May 1993. <https://doi.org/10.2118/26039-MS>.
- Maxwell, J. C. 1873. *A Treatise on Electricity and Magnetism*, first edition. Oxford, England, UK: Clarendon Press.
- McElhaney, K.W., Vlassak, J.J., and Nix, W.D. 1998. Determination of Indenter Tip Geometry and Indentation Contact Area for Depth-Sensing Indentation Experiments. *Journal of Materials Research*, 13(5), 1300–1306. <https://doi.org/10.1557/JMR.1998.0185>.
- Miller, M., Bobko, C., Vandamme, M., Ulm, F.-J. 2008. Surface Roughness Criteria for Cement Paste Nanoindentation. *Cement and Concrete Research*, 38(4), 467–476. <https://doi.org/10.1016/j.cemconres.2007.11.014>.
- Mishnaevsky Jr, L.L. 1995. Physical Mechanisms of Hard Rock Fragmentation under Mechanical Loading: A Review. *International Journal of Rock Mechanics and Mining Sciences & Geomechanics Abstracts*, 32(8), 763–766. [https://doi.org/10.1016/0148-9062\(95\)00027-E](https://doi.org/10.1016/0148-9062(95)00027-E).
- Morsy, S., Sheng, J.J., Gomaa, A., and Soliman, M.Y. 2013. Potential of Improved Waterflooding in Acid-Hydraulically-Fractured Shale Formations. Paper presented at the SPE Annual Technical Conference and Exhibition, New Orleans, Louisiana, USA, September 2013. <https://doi.org/10.2118/166403-MS>.
- Nair, A.K., Cordill, M.J., Farkas, D., and Gerberich, W.W. 2009. Nanoindentation of Thin Films: Simulations and Experiments. *Journal of Materials Research*, 24, 1135–1141. <https://doi.org/10.1558/jmr.2009.0136>.
- Nelson, P.H. 2009. Pore-Throat Sizes in Sandstones, Tight Sandstones, and Shale. *AAPG Bulletin*, 93(3), 329–340. <https://doi.org/10.1306/1024080859>.
- Nohava, J., Randall, N.X., and Conté, N. 2009. Novel Ultra Nanoindentation Method with Extremely Low Thermal Drift: Principle and Experimental Results. *Journal of Materials Research*, 24(3), 873–882. <https://doi.org/10.1557/jmr.2009.0114>.
- Nolte, K.G. 1979. Determination of Fracture Parameters From Fracturing Pressure Decline. Paper Presented at the SPE Annual Technical Conference and Exhibition, Las Vegas, Canada, Nevada, USA, September 1979. <https://doi.org/10.2118/8341-MS>.
- Nolte, K.G. 1986. A General Analysis of Fracturing Pressure Decline With Application to Three Models. *SPE Formation Evaluation*, 1(6), 571–583. <https://doi.org/10.2118/12941-PA>.



- Oliver, W.C., and Pharr, G.M. 1992. An Improved Technique for Determining Hardness and Elastic Modulus Using Load and Displacement Sensing Indentation Experiments. *Journal of Materials Research*, 7(6), 1564–1583. <https://doi.org/10.1557/JMR.1992.1564>.
- Oliver, W.C., and Pharr, G.M. 2004. Measurement of Hardness and Elastic Modulus by Instrumented Indentation: Advances in Understanding and Refinements to Methodology. *Journal of Material Research*, 19(1), 3–20. <https://doi.org/10.1557/JMR.2004.19.1.3>.
- Ortega, C., and Aguilera, R. 2012. Use of Drill Cuttings for Improved Design of Hydraulic Fracturing Jobs in Horizontal Wells. Paper presented at the Americas Unconventional Resources Conference, Pittsburgh, Pennsylvania, USA, June 5–7. <https://doi.org/10.2118/155746-MS>.
- Ortega, C., and Aguilera, R. 2014. A Complete Petrophysical-Evaluation Method for Tight Formations From Drill Cuttings Only in the Absence of Well Logs. *SPE Journal*, 19(4), 636–647. <https://doi.org/10.2118/161875-PA>.
- Ouchterlony, F. 1988. ISRM Commission on Testing Methods. Suggested Methods for Determining the Fracture Toughness of Rock. *International Journal of Rock Mechanics and Mining Sciences Geomechanical Abstract*, 25(2), 71–96. [https://doi.org/10.1016/0148-9062\(88\)91871-2](https://doi.org/10.1016/0148-9062(88)91871-2).
- Paliwal, B. and Ramesh, K.T. 2008. An Interacting Micro-Crack Damage Model for Failure of Brittle Materials Under Compression. *Journal of the Mechanics and Physics Solids*, 56 (3), 896-923. <https://doi.org/10.1016/j.jmps.2007.06.012>.
- Park, S., Costa, K.D., and Ateshian, G.A. 2004. Microscale Frictional Response of Bovine Articular Cartilage from Atomic Force Microscopy. *Journal of Biomechanics*, 37(11), 1679–1687. <https://doi.org/10.1016/j.jbiomech.2004.02.017>.
- Pharr, G.M., Oliver, W.C., and Brotzen, F. R. 1992. On The Generality of The Relationship among Contact Stiffness, Contact Area, and Young's Modulus during Indentation. *Journal of Material Research Technology*, 7 (3), 613–617. <https://doi.org/10.1557/JMR.1992.0613>.
- Pharr, G.M., and Bolshakov, A. 2002. Understanding Nanoindentation Unloading Curves. *Journal of Material Research*, 17(10), 2660–2671.
- Pharr, G.M., Herbert, E.G., and Gao, Y. 2010. The Indentation Size Effect: A Critical Examination Observations and Mechanistic Interpretations. *Annual Review of Materials Research*, 40, 271–292. <https://doi.org/10.1146/annurev-matsci-070909-104456>.
- Pietras, D., Aliha, M.R.M., and Sadowski, T. 2020. Mode III Fracture Toughness Testing and Numerical Modeling for Aerated Autoclaved Concrete using Notch Cylinder Specimen Subjected to Torsion. *Materialstoday: Proceedings*, 45(5), 4326–4329. <https://doi.org/10.1016/j.matpr.2020.12.899>.

- Ponton, C.B., and Rawlings, R.D. 1989a. Vickers Indentation Fracture Toughness Test Part 1 Review of Literature and Formulation of Standardised Indentation Toughness Equations. *Journal of Materials Science and Technology*, 5(9), 865–872. <https://doi.org/10.1179/mst.1989.5.9.865>.
- Ponton, C.B., and Rawlings, R.D. 1989b. Vickers Indentation Fracture Toughness Test Part 2 Application and Critical Evaluation of Standardised Indentation Toughness Equations. *Journal of Material Science and Technology*, 5(10), 961–976. <https://doi.org/10.1179/mst.1989.5.10.961>.
- Popov, V.L. 2010. *Contact Mechanics and Friction*. Springer-Verlag Berlin Hedielsberg. <https://doi.org/10.1007/978-3-642-10803-7>.
- Poulsen, D.K., and Soliman, M.Y. 1986. A Procedure for Optimal Hydraulic Fracturing Treatment Design. Paper presented at the SPE Eastern Regional Meeting, Columbus, Ohio, USA, November 1986. <https://doi.org/10.2118/15940-MS>.
- Raven, M.D., and Self, P.G. 2017. Outcomes of 12 Years of the Reynolds Cup Quantitative Mineral Analysis Round Robin. *Clays and Clay Minerals*, 65(2), 122–134. <https://doi.org/10.1346/CCMN.2017.064054>.
- Ren, L., Xie, H.P., Sun, X., Zhang, R., Li, C.B., Xie, J., and Zhang, Z.T. 2020. Characterization of Anisotropic Fracture Properties of Silurian Longmaxi Shale. *Rock Mechanics and Rock Engineering*, 54, 665–678. <https://doi.org/10.1007/s00603-020-02288-9>.
- Rinehart, J.S., Fortin, J-P., and Burgin, L. 1961. Propagation Velocity of Longitudinal Waves in Rocks. Effects of State of Stress, Stress Level of the Wave, Water Content, Porosity, Temperature, Stratification and Texture. Paper presented at the 4<sup>th</sup> US Symposium on Rock Mechanics (USRMS), University Park, Pennsylvania, March 1961. ARMA-61-119.
- Roberts, J.M., and Elmore, R.D. 2018. A Diagenetic Study of the Woodford Shale in the Southeastern Anadarko Basin, Oklahoma, USA: Evidence for Hydrothermal Alteration in Mineralized Fractures. *Interpretation*, 6(1), 1–13. <https://doi.org/10.1190/INT-2017-0071.1>.
- Rother, B., Steiner, A., Dietrich, D.A., Jehn, H.A., Haupt, J., and Giessler, W. 1998. Depth-Sensing Indentation Measurements with Vickers and Berkovich indenters. *Journal of Materials Research*, 13(8), 2071–2076. <https://doi.org/10.1557/JMR.1998.0291>.
- Rybacki, E., Reinicke, A., Meier, T., Makasi, M., and Dresen, G. 2015. What Controls the Mechanical Properties of Shale Rocks? Part I: Strength and Young's Modulus. *Journal of Petroleum Science and Engineering*, 135, 702–722. <https://doi.org/10.1016/j.petrol.2015.10.028>.



- Sayers, C.M. 2013. The Effect of Kerogen on the Elastic Anisotropy of Organic-Rich Shale. *Geophysics*, 78(2), 65– 74. <https://doi.org/10.1190/geo2012-0309.1>.
- Schiffmann, K.I. 2011. Determination of Fracture Toughness of Bulk Materials and Thin Films by Nanoindentation: Comparison of Different Models. *Philosophical Magazine*, 91(7–9), 1163–1178. <https://doi.org/10.1080/14786435.2010.487984>.
- Sebastiani, M., Johannis, K.E., Herbert, E.G., and Pharr, G.M. 2015. Measurement of Fracture Toughness by Nanoindentation Methods: Recent Advances and Future Challenges. *Current Opinion in Solid State and Materials Science*, 19(6), 324–333. <https://doi.org/10.1016/j.cossms.2015.04.003>.
- Serajian, V., and Ghassemi, A. 2011. Hydraulic Fracture Initiation from a Wellbore in Transversely Isotropic Rock. Paper presented at the 45<sup>th</sup> US Rock Mechanics/Geomechanics Symposium, San Fransisco, USA, June 26–29. ARMA 11–201.
- Senseny, P.E., and Pfeifle, T.W. 1984. Fracture Toughness of Sandstones and Shales. Paper presented at the 25<sup>th</sup> US Symposium on Rock Mechanics (USRMS), Evanston, Illinois, June 1984. ARMA-84-0390.
- Sharafi, S., Santare, M.H., Gerdes, J., and Advani, S.G. 2021. A Review of Factors that Influence the Fracture Toughness of Extrusion-based Additively Manufactured Polymer and Polymer Composites. *Additive Manufacturing*, 38, 1–24. <https://doi.org/10.1016/j.addma.2020.101830>.
- Sheng, J., Morsy, S., Gomaa, A., and Soliman, M.Y. 2014. Matrix Acidizing Characteristics in Shale Formations. *Journal of Petroleum & Biotechnology*, 5(5), 1–10. <https://doi.org/10.4712/2157-7463.1000194>.
- Sherbeny, W.E., Nuic, I., and Madkour, A. Significance of Advanced Cuttings Evaluation (ACE) Technologies for Chemostratigraphy Purposes While Drilling; Technology Overview and Applications. Paper presented at the SPE North Africa Technical Conference and Exhibition, Cairo, Egypt, September 2015. <https://doi.org/10.2118/175860-MS>.
- Shukla, P., Kumar, V., Curtis, M., Sondergeld, C.H., and Rai, C.S. 2013. Nanoindentation Studies on Shale. Paper presented at the 47<sup>th</sup> U.S. Rock Mechanics/Geomechanics Symposium, San Francisco, California, USA, 23-26 June. ARMA-2013-578.
- Simon, R. 1967. Rock Fragmentation by Concentrated Loading. In: Fairhurst (Ed.), *Proceedings of the 8<sup>th</sup> US Symposium on Rock Mechanics*, 440–454. ARMA-66-0440.
- Sinha, S., Mirshams, R.A., Wang, T., Nene, S.S., Frank, M., Liu, K., Mishra, R.S. 2019. Nanoindentation Behavior of High Entropy Alloys with Transformation Induced Plasticity. *Scientific Reports*, 9(1), 6639. <https://doi.org/10.1038/s41598-019-43174-x>.

Singh, R.N., and Sun, G.X. 1990. An Investigation into Factors Affecting Fracture Toughness of Coal Measures Sandstones. *Journal of Mines, Metals and Fuels*, 38(6), 111–118.

Sneddon, I.N. 1965. The Relation Between Load and Penetration in the Axisymmetric Boussinesq Problem for a Punch of Arbitrary Profile. *International Journal of Engineering Science*, 3(1), 47–57. [https://doi.org/10.1016/0020-7225\(65\)90019-4](https://doi.org/10.1016/0020-7225(65)90019-4).

Soliman, M.Y. 1983. Modifications to Production Increase Calculations for a Hydraulically Fractured Well. *Journal of Petroleum Technology*, 35(1), 170–172. <https://doi.org/10.2118/9021-PA>.

Soliman, M.Y. 1986. Numerical Model Estimates Fracture Production Increase. *Oil & Gas Journal*, 84(41).

Soliman, M.Y., Hunt, J.L., and El Rabaa, A.M. 1990. Fracturing Aspects of Horizontal Wells. *Journal of Petroleum Technology*, 42(08), 966–973. <https://doi.org/10.2118/18542-PA>.

Soliman, M.Y., Kuhiman, R.D., and Poulsen, D.K. 1991. *Method of Determining Fracture Parameters for Heterogeneous Formations* (US Patent No. 5,005,643A) US Patent Office. [US5005643A - Method of determining fracture parameters for heterogenous formations - Google Patents](https://patents.google.com/patent/US5005643A)

Soliman, M.Y., Craig, D.P., Bartko, K.M., Rahim, Z., and Adams, D.M. 2005. Post-Closure Analysis to Determine Formation Permeability, Reservoir Pressure, Residual Properties. Paper presented at the SPE Middle East Oil and Gas Show and Conference, Kingdom of Bahrain, March 2005. <https://doi.org/10.2118/93419-MS>.

Sondergeld, C.H., and Rai, C.S. Controls on the Geomechanical Properties of Unconventional Resource Formations. *Online Journal for E&P Geoscientists*. Adopted from oral presentation given at 2019 AAPG Hedberg Conference, The Evolution of Petroleum Systems Analysis: Changing of the Guard from Late Mature Experts to Peak Generating Staff, Houston, Texas, United States, March 4–6, 2019. <https://doi.org/10.1306/80707Sondergeld2019>.

Sone, H., and Zoback, M. 2013. Mechanical Properties of Shale-Gas Reservoir-Rocks—Part 1: Static and Dynamic Elastic Properties and Anisotropy. *Geophysics*, 78(5), D381–D392. <https://dx.doi.org/10.1190/geo2013-0050.1>.

Tabor, D. 1950. *The Hardness of Metals*. Clarendon Press: Oxford.

Tada, H., Paris, P.C., and Irwin, G.R. 2000. *The Stress Analysis of Cracks*, third edition. New York, USA: ASME Press.

Tai, K., Ulm, F.J., and Ortiz, C., 2006. Nanogranular Origins of the Strength of Bone. *Nano Letters*, 6(11), 2520–2525. <https://doi.org/10.1021/nl061877k>.

- Tang, H., Li, S., and Zhang, D. 2018. The Effect of Heterogeneity on Hydraulic Fracture in Shale. *Journal of Petroleum Science and Engineering*, 162, 292–308. <https://doi.org/10.1016/j.petrol.2017.12.020>.
- Thiercelin, M. 1989. Fracture Toughness and Hydraulic Fracturing. *International Journal of Rock Mechanics and Mining Sciences & Geomechanics Abstracts*, 26(03-04), 177–183. [https://doi.org/10.1016/0148-9062\(89\)91967-0](https://doi.org/10.1016/0148-9062(89)91967-0).
- Tran, M.H., Chen, S., Rafael, S.P., Abousleiman, Y., and Slatt, R.M. 2014. A Geomechanics Approach to Evaluate Gas Shale Frackability: A Case Study with the Woodford Shale. Poster presented at the AAPG Annual Convention and Exhibition, Long Beach, California, USA, 22-25 April. #50913.
- Tutuncu, A.N., Myers, M.T., and Arasteh, M.M. 2004. *Use of Cutting Velocities for Real Time Pore Pressure and Fracture Gradient Prediction* (US Patent No. 20040236513 A1) US Patent Office. [US20040236513A1 - Use of cutting velocities for real time pore pressure and fracture gradient prediction - Google Patents](https://patents.google.com/patent/US20040236513A1)
- Tutuncu, A.N., Myers, M.T., and Arasteh, M.M. 2005. *Use of Cutting Velocities for Real Time Pore Pressure and Fracture Gradient Prediction* (US Patent No. 6,968,274) US Patent Office.
- Ulm, F.J., Vandamme, M., Bobko, C., Alberto Ortega, J., Tai, K., and Ortiz, C. 2007. Statistical Indentation Techniques for Hydrated Nanocomposites: Concrete, Bone, and Shale, *Journal of the American Ceramic Society*, 90(9), 2677–2692. <https://doi.org/10.1111/j.1551-2916.2007.02012.x>.
- U.S. Energy Information Administration (EIA). 2013, January 2. *Shale Oil and Shale Gas Resources are Globally Abundant*. Retrieved from [Shale oil and shale gas resources are globally abundant - Today in Energy - U.S. Energy Information Administration \(EIA\)](https://www.eia.gov/energyexplained/shale/shale_oil_and_gas_resources.php).
- U.S. Energy Information Administration (EIA). 2020, September 2020. *How Much Shale (Tight) Oil is Produced in the United States?*. Retrieved from [Frequently Asked Questions \(FAQs\) - U.S. Energy Information Administration \(EIA\)](https://www.eia.gov/energyexplained/shale/shale_oil_and_gas_resources.php).
- Vizini, V.O.S., and Futai, M.M. 2021. Mode II Fracture Toughness Determination of Rock and Concrete via Modified Direct Shear Test. *Engineering Fracture Mechanics*, 257, 1–16. <https://doi.org/10.1016/j.engfracmech.2021.108007>.
- Voronoi, G. 1908. Nouvelles Applications Des Paramètres Continus à la Théorie Des Formes Quadratiques. Premier Mémoire. Sur Quelques Propriétés Des Formes Quadratiques Positives Parfaites. *Journal für die reine und angewandte Mathematik*, 133, 97–102. <https://doi.org/10.1515/crll.1908.133.97>.
- Wang, Z., Wang, H., and Cates, M.E. 2001. Effective Elastic Properties of Solid Clays. *Geophysics*, 66(2), 428–440. <https://doi.org/10.1190/1.1444934>.

Westergaard, H.M. 1939. *Bearing Pressures and Cracks*. Cambridge Mass.

Wild, K.M., Wymann, L.P., Zimmer, S., Thoeny, R., and Amann, F. 2015. Water Retention Characteristics and State-Dependent Mechanical and Petro-Physical Properties of a Clay Shale. *Rock Mechanics and Rock Engineering*, 48(2), 427–439. <https://doi.org/10.1007/s00603-014-0565-1>.

Xiang, D., Chen, Z., Yang, Z., and Wang, S. 2017. Probing the Mechanical Properties of Shale by Nanoindentation. In: *Proceedings of the Geotechnical Frontiers*, Florida.

Yuan, J., Zhou, J., Liu, S., Feng, Y., Deng, J., Xie, Q., and Lu, Z. 2017. An Improved Fracability-Evaluation Method for Shale Reservoirs based on New Fracture Toughness-Prediction Models. *SPE Journal*, 22(05), 1704–1713. <https://doi.org/10.2118/185963-PA>.

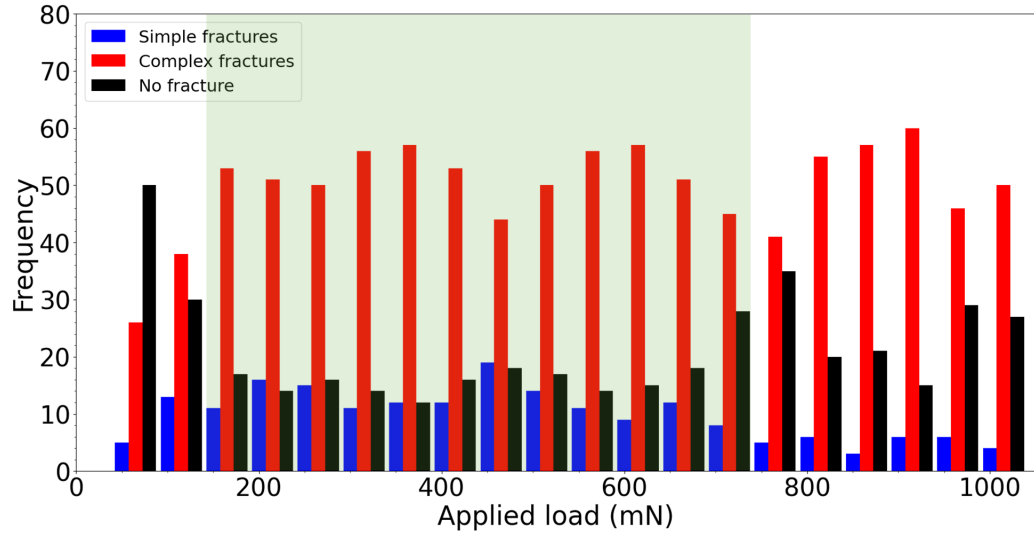
Zhang, J. 2013. Borehole Stability Analysis Accounting for Anisotropies in Drilling to Weak Bedding Planes. *International Journal of Rock Mechanics and Mining Sciences*, 60, 160–170. <https://doi.org/10.1016/j.ijrmms.2012.12.025>.

Zhang, H., Li, Y.E., Zhao, D., Zhao, J., and Liu, H. 2018. Formation of Rifts in Central Tibet: Insight from P wave Radial Anisotropy. *Journal of Geophysical Research: Solid Earth*, 123, 8827–8841. <https://doi.org/10.1029/2018JB015801>.

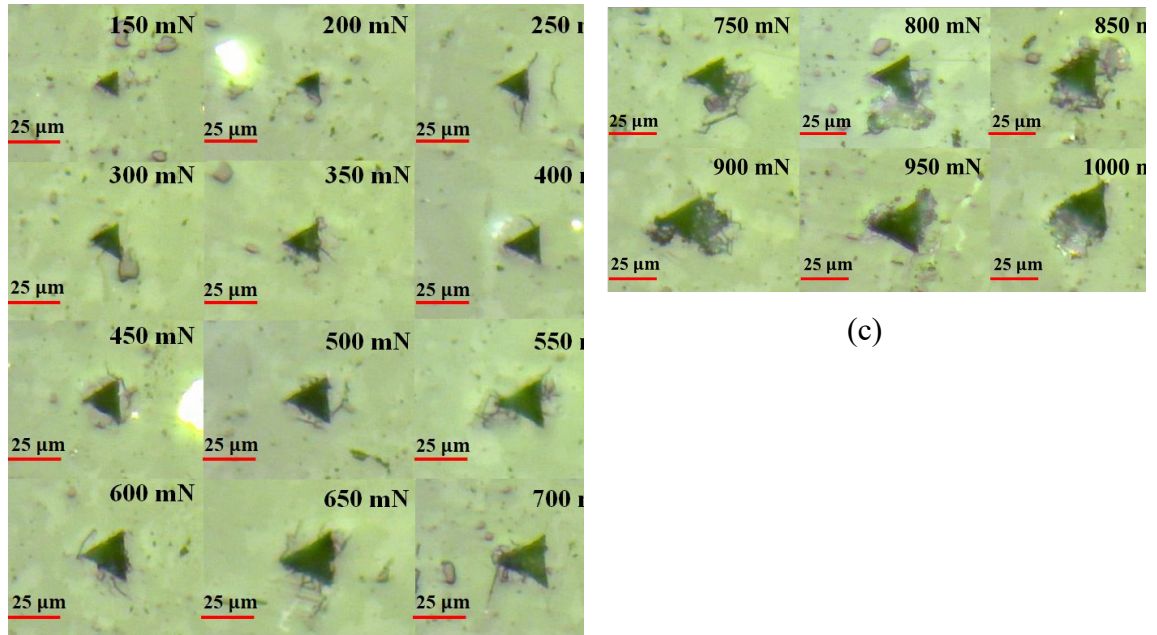
Zhu, W., Fonteyn, M.T.J., Hughes, J., and Pearce, C., 2009, Nanoindentation Study of Resin Impregnated Sandstone and Early-Age Cement Paste Specimens. In: Bittnar Z., Bartos P.J.M., Němeček J., Šmilauer V., Zeman J. (eds) *Nanotechnology in Construction 3*. Springer, Berlin, Heidelberg. [https://doi.org/10.1007/978-3-642-00980-8\\_55](https://doi.org/10.1007/978-3-642-00980-8_55).

## APPENDICES

### 1. Histogram of Samples B, C, and D (in lieu of Chapter 5)



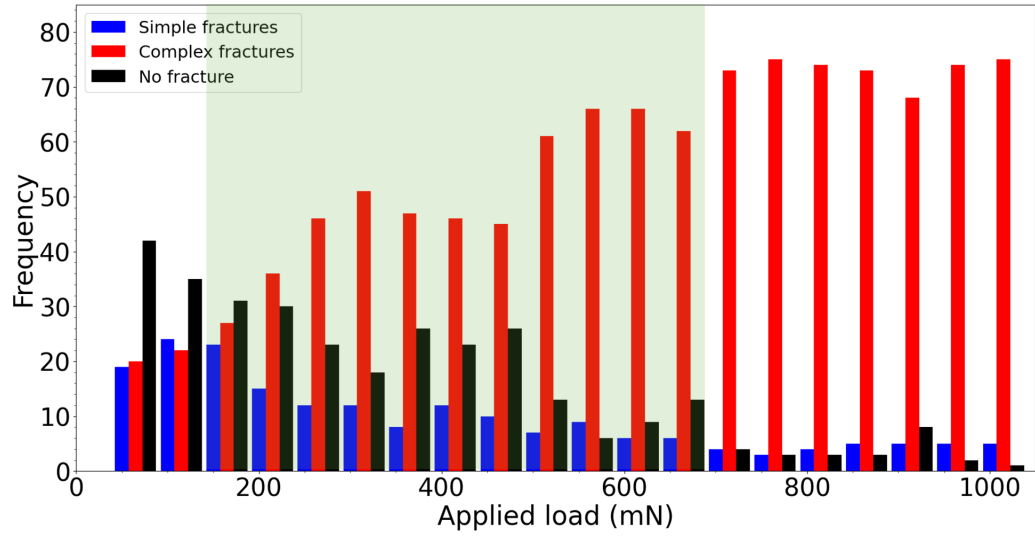
(a)



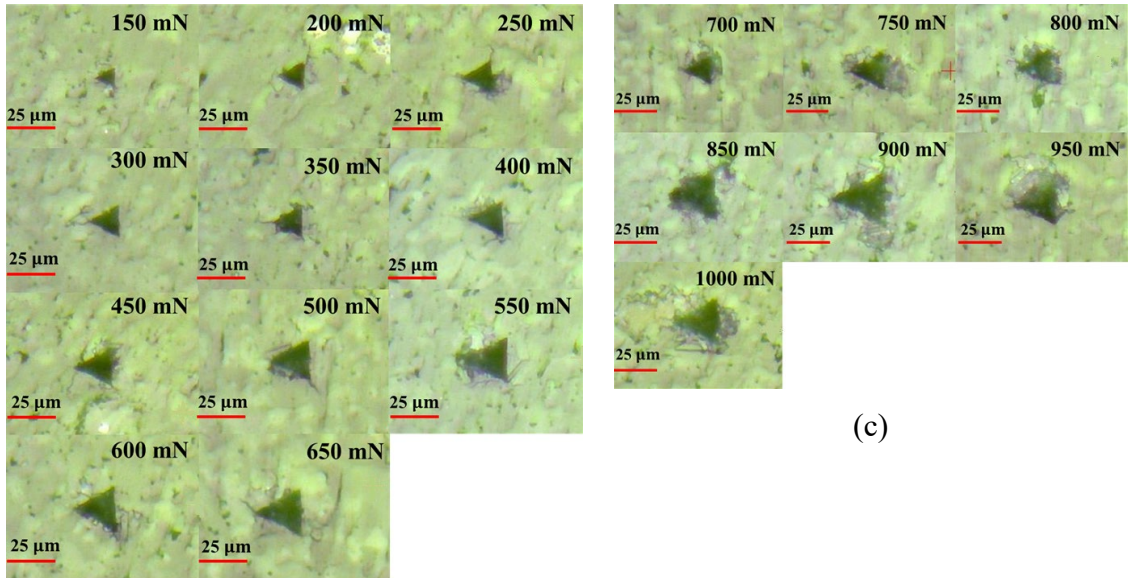
(b)

(c)

Figure A.1—Histogram of sample B (parallel to the bedding) in three regions with various loads. High-resolution images where the applied load is **b** acceptable when it is smaller than or equal to 700 mN and **c** excessive when it is larger than 700 mN to characterize shale fracture toughness.



(a)

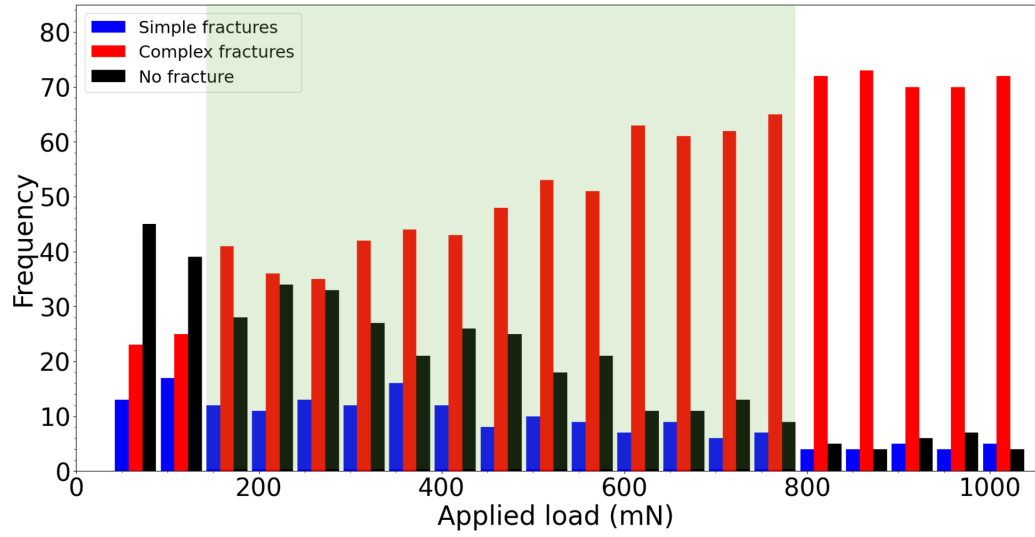


(c)

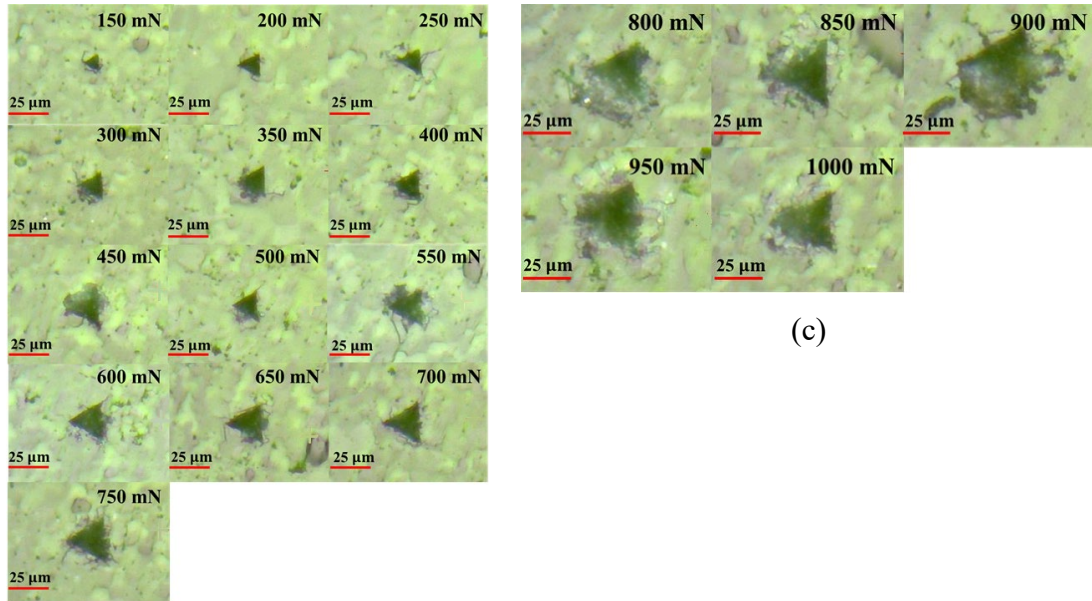
(b)

Figure A.2—Histogram of sample C (perpendicular to the bedding) in three regions with various loads. High-resolution images where the applied load is **b** acceptable when it is smaller than or equal to 650 mN and **c** excessive when it is larger than 650 mN to characterize shale fracture toughness.





(a)



(c)

(b)

Figure A.3—Histogram of sample D (perpendicular to the bedding) in three regions with various loads. High-resolution images where the applied load is **b** acceptable when it is smaller than or equal to 750 mN and **c** excessive when it is larger than 750 mN to characterize shale fracture toughness.

## 2. Title pages of the journal publications relevant to the dissertation

PETROPHYSICS, VOL. 61, NO. 5 (OCTOBER 2020); PAGES 404–416; 12 FIGURES. DOI: 10.1016/j.petphys.2020.100001

### Nanoindentation of Shale Cuttings and Its Application to Core Measurements

Erica Esatyana<sup>1</sup>, A. Sakhaee-Pour<sup>1\*</sup>, Fadhil N. Sadooni<sup>2</sup>, and Hamad Al-Saad Al-Kuwari<sup>2</sup>

#### ABSTRACT

Large samples (~1 in.) required for standard tests are often unavailable in shale formations due to various reasons. They are not usually recovered in horizontal drilling, which is a common practice in hydraulic fracturing. They also delaminate and are difficult to process in core analysis. Hence, common characterization techniques face challenges and lead to uncertainties. A new method is needed that can be applied to small pieces, such as drill cuttings, which are often the only available sources, especially in real-time conditions. The present

study proposes a new method applicable to the cuttings to determine the geomechanical properties of shale formations at the core scale from nanoindentations. In particular, the Young's moduli have been determined from cuttings, and the results are compared with those of the core plugs. Nanoindentation and the required sample preparation are reviewed. The results are promising, and the methodology has applications in characterizing formation heterogeneity in the petroleum industry.

#### INTRODUCTION

Hydraulic fracturing has increased energy recovery from shale formations within the last decade. Although increased production has played a dominant role, the full potential of such resources is yet to be realized. One of the key challenges is evaluating formations that encounter difficulties due to the lack of large samples.

Large samples, such as core plugs (~1 in.) or blocks that are an important part of formation characterization, are not usually available, as recovering them is difficult and expensive. Large-scale tests are also time consuming and expensive. Thus, the data required for detailed analysis are scarce, leading to uncertainties in predicting the performance of a formation. The lack of large samples is relevant, especially to shale formations, as they delaminate and are hard to process in core analysis.

Drill cuttings are often the only sources available and provide useful information for formation evaluation (Tutuncu et al., 2005), and predicting the relevant properties from drill cuttings is a known problem (Tutuncu et al., 2004). One appealing test for analyzing cuttings is nanoindentation because it can be done on small samples. Nanoindentation is based on contact mechanics, which was founded by Hertz

(1896). He recognized that the mathematics of contact between two elastic bodies resembles common problems in electricity and proposed five key assumptions that were adopted later but did not derive from the stress field (Huber, 1904).

Indentation has a wide range of applications because it can be performed easily, and the results provide useful information about Young's modulus (Sneddon, 1965; Velez et al., 2001), hardness (Bobji and Biswas, 1998), cracking (Lawn et al., 1980), creep (Li et al., 2008), and fracture toughness (Laugier, 1987; Volinsky et al., 2003). The main idea is that the features of the load-displacement curve are related to the specimen deformation. Researchers have applied nanoindentation to heterogeneous media, characterizing cement (Constantinides et al., 2003; Constantinides and Ulm, 2004; Jennings et al., 2005), shale (Ulm et al., 2007; Shukla et al., 2013), and even bone (Tai et al., 2006), based on conceptual models that have enabled them to interpret nano- to microscale deformations of forming phases (Ulm and Abousleiman, 2006; Ortega et al., 2007; Abedi et al., 2016a; Abedi et al., 2016b). They have also used nanoindentation to investigate carbonate properties (De Paula et al., 2010; Vialle and Lebedev, 2015; Uribe et al., 2016). Research using nanoindentations has

Manuscript received by the Editor February 23, 2020; revised manuscript received May 25, 2020; manuscript accepted June 26, 2020.

<sup>1</sup>University of Houston, Cullen College of Engineering, Department of Petroleum Engineering, UH Technology Bridge, 5000 Gulf Freeway Bldg 9, Room 219, Houston, TX 77204-0945

<sup>2</sup>Environmental Science Center, Qatar University, P. O. Box 2713, Doha, Qatar

\*Corresponding author: asakhaee@central.uh.edu



# Characterizing Anisotropic Fracture Toughness of Shale Using Nanoindentation

Erica Esatyana, Mehdi Allipour, and A. Sakhaee-Pour, University of Houston

## Summary

Shale, which has pores as small as 10 nm, is economically viable for hydrocarbon recovery when it is fractured. Although the fracture toughness dictates the required energy for the improvement, the existing techniques are not suitable for characterization at scales smaller than 1 cm. Developing practical methods for characterization is crucial because fractures can contribute to an accessible pore volume at different scales. This study proposes a conceptual model to characterize the anisotropic fracture toughness of shale using nanoindentations on a sub-1-cm scale. The conceptual model reveals the complexities of characterizing shales and explains why induced fractures differ from those observed in more-homogeneous media, such as fused silica. Samples from the Wolfcamp Formation were tested using Berkovich and cube-corner tips, and the interpreted fracture toughness values are promising. The conceptual model is the first application of the effective-medium theory for fracture toughness characterization using nanoindentation. In addition, it can quantify fracture toughness variations when using small samples, such as drill cuttings.

## Introduction

Shale is a sedimentary rock containing clay minerals and silt-sized particles (Blatt and Tracy 1996) with a pore size of smaller than 100 nm in its matrix, which results in ultralow permeability. Shale gas was first extracted in 1821 (Hill et al. 2004) and has recently become economically viable because of hydraulic fracturing. This has made the US a significant fossil fuel producer.

Since the Stanolind Oil and Gas Corporation performed the first hydraulic fracturing using water-based muds in 1947 (King 2012), many stimulations have shown favorable results and an increased recovery rate. Fracture toughness is a crucial parameter for the successful design of the formation stimulation, which, in practice, is usually evaluated on a large scale (King 2012). The mechanical properties measured in the laboratory with triaxial compression are usually static measurements (Fjar et al. 1992), whereas dynamic measurements are acquired from logging and wave velocities. Consequently, pertinent information remains scarce on a small scale (<1 cm).

Fracture toughness depends on material properties, and the estimated value based on nanoindentation accounts for the tip geometry, applied load, and induced fracture length. The fracture toughness is usually expressed in  $\text{MPa}\cdot\text{m}^{1/2}$ . It can be as small as  $0.01 \text{ MPa}\cdot\text{m}^{1/2}$  for polymers and foams and as large as  $175 \text{ MPa}\cdot\text{m}^{1/2}$  for steel (Ashby 1999). The fracture toughness estimation is discussed in detail later in this study (Eqs. 1 and 2).

The core scale, which is a standard scale in petroleum engineering, is on the order of a few centimeters (Civan 2016). A core sample is valuable for quantitative characterizations and is often used to calibrate reservoir parameters. However, retrieving core samples is costly and time-consuming, and it is challenging to preserve the retrieved piece during transportation.

Small pieces of rock (drill cuttings) are abundant and often discarded in landfills. These samples are a potential source of information. Their characterization entails unique measurements and interpretations that can be conducted using nanoindentations.

Nanoindentation, which is considered nondestructive, has become popular because it is applicable to small samples. Researchers have used this technique to characterize composite materials (Brown et al. 2018) and thin films (Fischer-Cripps 2011). In addition, researchers have used nanoindentation in petroleum engineering to determine geomechanical properties (Abousleiman et al. 2007). For instance, Gupta et al. (2018) determined the shear modulus and hardness of shale, Liu et al. (2018) obtained the geomechanical properties of Bakken shale, and Kumar et al. (2012) quantified the effects of organic content and thermal maturity on shale response. Although these investigations shed light on the shale response, it is challenging to determine fracture toughness using nanoindentation. Table 1 lists the properties obtained by nanoindentation.

Geomechanical Properties	Reference
Young's modulus, $E$	Abousleiman et al. (2007); Kumar et al. (2012); Liu et al. (2018)
Hardness, $H$	Abousleiman et al. (2007); Liu et al. (2018)
Shear modulus, $G$	Liu et al. (2018)
Fracture toughness, $K_{IC}$	Gupta et al. (2018)

Table 1—Summary of the geomechanical properties obtained by nanoindentation.

This study proposes a conceptual model based on the effective-medium theory to characterize the fracture toughness of the shale. In addition, it clarifies the complexities of fracture patterns created by different compression (overburden) loads applied to the surface of a dry sample and indicates when it is more feasible to use existing analytical relations, such as Eq. 2, for fracture toughness based on linear elastic fracture mechanics.

## Materials

**Sample Descriptions.** Four shale samples from the Wolfcamp Formation have been studied. The Wolfcamp Formation has been an unconventional resource in the Permian Basin, Texas. Two samples (Samples 1 and 2) are parallel to, and two (Samples 3 and 4) are perpendicular to, the bedding plane. Each sample is tested by the Berkovich and cube-corner tips.

Copyright ©2021 Society of Petroleum Engineers

Original SPE manuscript received for review 28 November 2020. Revised manuscript received for review 12 March 2021. Paper (SPE 205486) peer approved 15 March 2021.

590

August 2021 SPE Reservoir Evaluation & Engineering

Downloaded from https://onepetro.org/REE/article-pdf/2021/05/590/4148707/205486.pdf by University of Houston user on 18 September 2021

